NANOPARTICLE-COATED OPTICAL MICRORESONATORS FOR WHISPERING-GALLERY LASING AND OTHER APPLICATIONS

By

SIYKA IVANOVA SHOPOVA

Master of Science in Engineering Physics
University of Sofia Kliment Ohridski
Sofia, Bulgaria
1989

Submitted to the Faculty of the
Graduate College of the
Oklahoma State University
in partial fulfillment of
the requirements for
the Degree of
DOCTOR OF PHILOSOPHY
May, 2007

UMI Number: 3259570

ProQuest Information and Learning Company
300 North Zeeb Road
P.O. Box 1346
Ann Arbor, MI 48106-1346

NANOPARTICLE-COATED OPTICAL

MICRORESONATORS FOR WHISPERING-GALLERY

LASING AND OTHER APPLICATIONS

Dissertation Approved:

Albert T. Rosenberger

Dissertation Adviser
James P. Wicksted

Paul A. Westhaus

Daniel Grischkowsky

A. Gordon Emslie

Dean of the Graduate College

ACKNOWLEDGMENTS

There are many people I wish to thank for supporting me in various ways throughout the years of graduate study. First on the list is my son, who has shared moments of excitement and frustration with me. Being compassionate and well behaved, he has given me the opportunity to accomplish this ordeal.

I would like to thank my academic adviser, professor Dr. Al Rosenberger, for the support, teaching, and freedom to explore my own ideas. His elaborate writing style has been a great example for me. My dissertation would not have been possible without his guidance.

I am grateful to all professors, whose classes I've taken throughout the years, for forming and broadening my understanding of the research area of Photonics. My special thanks to Dr. Grischkowsky, who has shared with us the ideas and accomplishments in his research area and has also taught us the way to approach the unknown and what it takes to discover. His words of support have given me confidence in myself to carry out my research experiments. I am thankful to Dr Westhaus, whose letter of recruitment made all the difference in my life. I thank Dr. Wicksted for being part of my dissertation committee and for his advice in my job search.

People who have worked and collaborated with me have enriched me with their knowledge and skills. My special thanks go to Dr. George Farca for the great team atmosphere all these years. I cannot list everything I need to thank him for, so I will just

say he's been the best colleague one could wish for. I thank Dr. Charles Blackledge for his expertise and the excitement we shared during the work on gold nanorods. I have learned much from Dr. Jeromy Rezac, who introduced me to the work in the lab, and Dr. David Smith from NASA Marshall Space Flight Center, with whom I had the pleasure to work on several occasions. I would also like to acknowledge other graduate students that have worked with me or have simply been friends: Dr. Michael Humphrey, Birol Ozturk, Lee Elizondo, Elijah Dale, Razvan Stoian, Ghazal Behin-Aein, Dr. Peyman Ahmadi, and many others.

I also have to recognize the help of Mike Lucas and the great work of the instrument shop that helped me so much in setting up and carrying out my experiments. I am thankful to Warren Grider, Charles Hunt, and everybody who has worked in the physics department office, especially Susan, for the constant support and warm feelings going beyond their duties.

Finally, I want to thank the small Bulgarian community in Stillwater and especially to our very special friend Dr. Joan Barrick, for her constant care and support, and my family for their understanding love and support.

TABLE OF CONTENTS

Chapter Page

Chapter Page

LIST OF TABLES

LIST OF FIGURES

Figure Page

Figure Page

Figure Page

Figure Page

CHAPTER I

INTRODUCTION

I.1 Light scattering and whispering-gallery modes (WGMs)

The study of light scattering and the closely related phenomenon of WGMs is always associated with the work of three great scholars: Lord Rayleigh [1, 2], who was also the first to study the phenomena of sound propagation in the whispering gallery of St. Paul's cathedral almost a century ago; Debye, who derived equations for the resonant eigenfrequencies of dielectric and metallic spheres (including WGMs) [3]; and Mie, whose theoretical studies on the scattering of plane electromagnetic waves by spheres can also lead to deriving the equations of WGMs [4].

The first observations of WGMs in optics were related to the operation of solid state lasers [5, 6]. Ironically these works did not initiate immediate scientific interest in WGMs, but did have some technological impact as the side surface of the laser rod was purposely made rough to eliminate WGMs. WGMs in droplets were studied because of their strong effect on fluorescence [7, 8], Raman scattering [9, 10], and laser action [11, 12]. Braginsky, Gorodetsky and Ilchenko [13] first showed the potential of WG resonators made of dielectric silica to exhibit extremely long photon storage times. This initiated a great deal of subsequent research on low threshold optical effects in such structures.

I.2 Nanoparticles

Materials with sizes greater than the size of one unit cell, but small enough to have properties different from the bulk material are usually considered to be nanoparticles or nanocrystals. Material properties can vary significantly depending on the size. Generally two different kinds of cluster-size effects can be distinguished: intrinsic effects, when the electronic and structural properties vary as a function of particle size and geometry, and extrinsic effects, which are size dependent responses to external fields or forces irrespective of the intrinsic effects.

As an example of an intrinsic effect, this work will further discuss optical material properties of semiconductor particles as a function of size. The quantum size effect, i.e. the dependence of electron energy levels on size, was discussed as early as 1937 by Frohlich [14]. When researchers study this effect they usually refer to nanocrystals as quantum dots (QDs).

Extrinsic cluster size effects were observed much earlier. These are the collective electronic or lattice excitations – also known as Mie resonances. In this work I am discussing in more detail the collective electronic excitations in gold nanoparticles.

Comprehensive reviews of the optical properties of semiconductor nanocrystals can be found in [15] and [16], and a review on metallic nanoparticles in [17].

I.3 Quantum-dot lasers and WGM lasers

The great benefits of lasers with QD active layers were predicted by Arakawa and Sakaki in the early 1980s [18]. Quantum dot lasers should exhibit performance that is less temperature-dependent than bulk and quantum well semiconductor lasers, and that

will not degrade at elevated temperatures. Other benefits of quantum dot active layers include ultralow and temperature-independent thresholds and an increase in differential gain at room temperature – that is, more efficient laser operation [19]. Different growing techniques were employed in the fabrication of QD laser structures. Metal-organic chemical vapor deposition (MOCVD) or molecular beam epitaxy produced QDs with suitable sizes, although nonradiative defects were produced during etching. In 1994 researchers at the Tokyo Institute of Technology reported lasing operation from an etched QD laser [20]. Selective growth and self-assembled growth techniques were later developed to avoid nonradiative defects. In 1994 researchers at the Technical University of Berlin and Ioffe Research Institute (St. Petersburg, Russia) reported the first self-assembled InAs/InGaAs QD laser, showing reduced temperature dependence of the threshold current [21]. Since then, InGaAs/GaAs QD lasers have successfully demonstrated low threshold current density, high operating temperature, and high differential gain at room temperature. Furthermore, QD devices have lased at 1.3 μm, which is an important wavelength for the telecommunications industry. The technology has also been used to produce vertical-cavity surface-emitting lasers (VCSELs) [22]. Concerns about the potential of QD lasers for high power emission, because of their small active volume, was ruled out by researchers in Germany. They fabricated a MOCVD-grown quantum dot laser that emits almost 11.7 W in "quasi" continuous-wave (cw) mode [23]. In normal cw mode, the maximum power is 4.7 W. The device consisted of six layers of quantum dots stacked on top of each other to form the gain medium. The laser was based on a gallium arsenide waveguide and indium gallium arsenide dots, and it emitted light at 1135 nm. With the output power set to 1.5 W, it had a lifetime of over

3000 hours at room temperature. The success of laser technology based on epitaxial QDs has motivated the development of laser devices based on ultrasmall, sub-10 nm nanoparticles fabricated via colloidal chemistry (nanocrystal quantum dots – NQD) [24-28]. Such NQDs have been synthesized with narrow size dispersions and high photoluminescence quantum yield. An additional advantage is that the emission wavelength of NQDs can be significantly modified by simply changing the NQD size or composition [25, 27, 29]. Optical gain and lasing [30, 31] in the visible part of the spectrum, from colloidal quantum dots, have been demonstrated. Infrared gain has also been shown in quantum dot nanocrystals; in PbSe [32], in HgTe [33], and in InAs [34]. Successful demonstrations of photoluminescence [35, 36] and lasing [37] of colloidal QDs in silica or polymer microspheres [38, 39] have recently been achieved.

I.4 Purpose and outline of this study

The purpose of this study is to explore the properties of high quality optical microsphere resonators in combination with various types of nanoparticles deposited on their surfaces. Optical whispering-gallery modes of the silica microspheres were pumped efficiently by tapered optical fibers. An adiabatic, extremely low loss, taper transition for various optical fibers was achieved. For whispering-gallery lasing, the microspheres were coated with HgTe quantum dots. Lasing in HgTe was demonstrated for the first time and record low thresholds were measured in these devices [40]. An interesting effect, the enhancement of evanescent coupling, was observed with microsphere resonators with gold nanorods grown on their surfaces (presented at CLEO/QELS 2006). We developed

a new procedure [41] that uses semiconductor nanoparticles as seeds for the growth of gold nanorods.

Outline:

Chapter II begins with an outline of the derivations of the electromagnetic theory of light scattering from a spherical particle (Mie scattering) and presents the properties of WGMs as a special case of Mie resonances. These derivations, with an extension for the scattering by elliptical particles, are then used for describing surface plasmon resonances. An original contribution is the model describing the extinction spectrum of an ensemble of spherical and rod-shaped gold nanoparticles. The program was written with the help of Elijah Dale, an undergraduate student in the Physics department (at that time).

Chapter III discusses the coupling mechanism using tapered optical fibers. Different coupling regimes are described by the ring cavity model. A taper puller was designed by the author and constructed with the help of Mike Lucas and the instrument shop. A LabView program for controlling the tapering process was done by my colleague George Farca. A procedure for monitoring the process of tapering, in order to verify the adiabaticity of the tapered fibers, was implemented. Also a dual-coupling configuration was realized. Finally an experimental example of coupling dependence on the fiber-resonator distance is given.

Chapter IV talks about energy band structure modifications in 3D confined semiconductor structures (quantum dots). Existing models are used for calculating the separation between the energy levels for HgTe nanocrystals as a function of the quantum dot radius. A model describing the gain spectrum of spherical semiconductor nanoparticles is also discussed.

Chapter V presents the experimental realization of a WGM laser based on a spherical microresonator coated with semiconductor nanoparticles. HgTe and HgCdTe nanoparticles used in this work were synthesized in Dr. N. Kotov's labs. Capillary electrophoresis was used to improve the size uniformity of the gain material. These experiments were carried out in the lab of Dr. El Rassi. Lasing at ultralow absorbed pump power was demonstrated. Results were published in Applied Physics Letters [40]. The large fraction of spontaneous emission coupled to the lasing mode is discussed on the basis of existing quantum and classical theories, which help to explain the low threshold operation of these lasers. In order to get precise measurement of the threshold in the excitation power we correlated the emission peak with the dip in the pump power, measuring the integrated scattered pump at the same time. These results were presented at the CLEO/QELS 2006 conference. Work on the selection of a single lasing mode using a coupled resonator system was initiated and will continue in the future. Several new ideas were contributed to this work: sparse coating of the resonator surface with semiconductor NPs – the relatively small number of NPs in the WGM volume allows for high quality factors and low transparency density thus reducing the threshold power of the microlaser; in the process of coating a resonator, D_2O was substituted for water; in order to get more efficient outcoupling, a second tapered fiber, optimized for coupling of light at the emission wavelength, was implemented in the system; correlated measurement of the pump, emission and scattering in a single pump WGM was introduced; and coupled microresonators for mode selection were used.

In **Chapter VI** I investigate the properties of microsphere resonators with gold nanoparticles grown on their surface. The process of growing of gold nanorods on different surfaces is original and was published in Applied Physics Letters [41]. It uses

semiconductor HgTe nanoparticles as seeds for initiating Au growth and allows for firm attachment of gold particles to various surfaces. The work on synthesis was done in collaboration with Dr. C. Blackledge. Furthermore, it was found that a sparse coverage of the surface of microresonators with Au nanorods results in a significant enhancement of the evanescent coupling. These results were reported at the CLEO/QELS 2006 conference.

CHAPTER II

MIE SCATTERING AND WHISPERING-GALLERY MODES

II.1 General scattering analysis

Mie scattering analysis gives expressions for the fields, caused by an incident plane wave, inside and outside of a small sphere of radius *a*. The analysis can be done for a metal as well as a dielectric sphere. In both cases it is necessary to find a solution to the vector wave equation in spherical coordinates:

$$\nabla^2 \vec{C} + k^2 \vec{C} = 0\,, \tag{II.1}$$

where the wave number *k* comes from:

$$k^2 = \varepsilon\mu\omega^2 + ig\mu\omega\,. \tag{II.2}$$

Here ε is the dielectric permittivity, μ is the permeability, and *g* is the conductivity of the medium. When it is necessary to distinguish between the regions interior and exterior to the sphere, these and other parameters will be labeled with a superscript *in* or *ex*.

For an isotropic medium, the wave equation can be solved in its scalar form,

$$\left(\nabla^2 + k^2\right)\psi = 0\,. \tag{II.3}$$

For any solution ψ of the scalar equation (II.3) there are three independent vector solutions $\vec{L}$, $\vec{M}$, and $\vec{N}$ of (II.1) defined as [42]:

Longitudinal part $$\vec{L} = \vec{\nabla}\psi \tag{II.4}$$

Transverse part $$\vec{M} = \vec{\nabla}\times\left(\vec{r}\psi\right)$$
$$\vec{N} = \frac{1}{k}\vec{\nabla}\times\vec{M}\ . \tag{II.5}$$

The three vector solutions form a basis in which any arbitrary wave function can be represented as a linear combination of these functions. The coefficients of expansion can be determined because of the orthogonal properties of $\vec{L}$, $\vec{M}$, and $\vec{N}$.

The solution of the scalar equation (II.3) in spherical coordinates has the form:

$$\psi_{\substack{e\\o}ml}(r,\theta,\varphi) = P_l^m(\cos\theta)Z_l(kr)\begin{matrix}\cos\\ \sin\end{matrix} m\varphi\,, \tag{II.6}$$

where *o* and *e* stand for odd and even; the time dependence factor $e^{-i\omega t}$ is omitted and will not be carried on to simplify further derivations. The spherical Bessel function $Z_l(kr)$ determines the radial transverse structure of the wave (Fig. II.1). The angular transverse structure is described by the Legendre polynomial $P_l^m(\cos\theta)$. For large values of l and $m \simeq l$, this function (and the corresponding field component) is concentrated in a narrow interval of angles θ near $\pi/2$ (Fig. II.2). If $m \neq l$ the mode acquires an oscillating transverse structure. The number of field extrema in the polar direction is *l*-*m*+1.

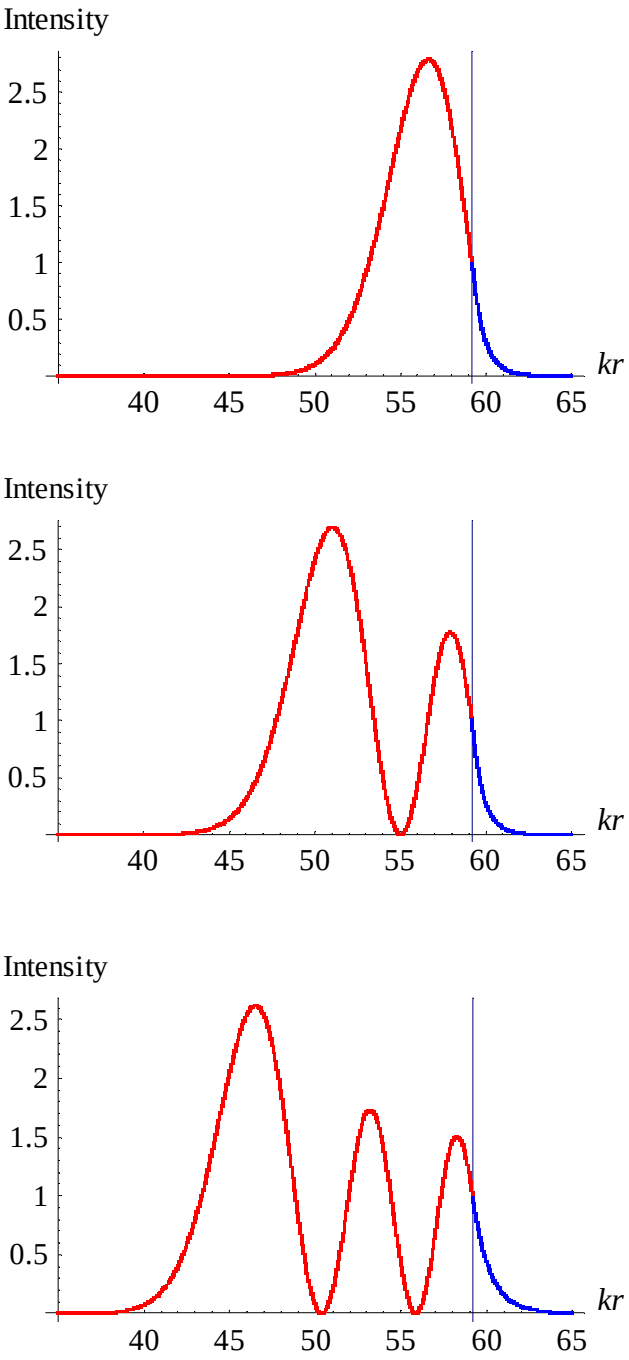

Figure II.1. Bessel function $[Z_l(kr)]^2$ representing the radial variation of the intensity of TE modes of wavelength λ = 800 nm for a silica sphere with a = 10.5 μm, n^{in} =1.45, n^{ex} =1 and radial order 1, 2, or 3 respectively. The red part is a spherical Bessel function of the 1st kind and the blue part is a spherical Hankel function of the 1st kind. The grid line represents the silica/air boundary.

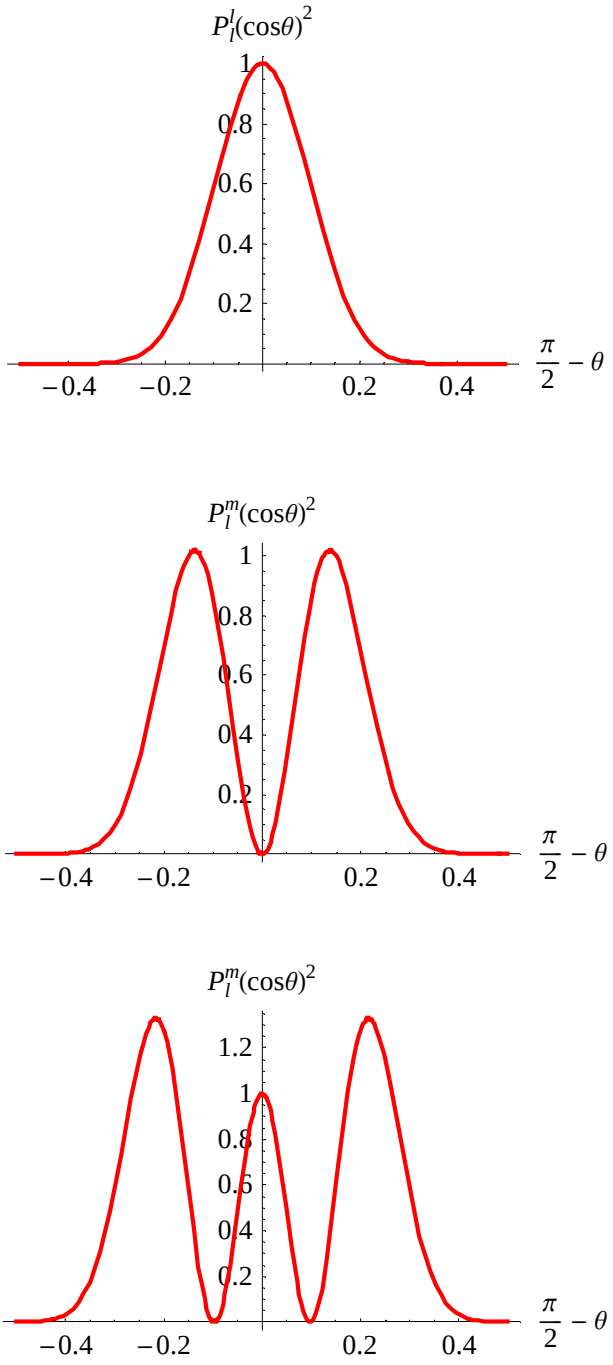

Figure II. 2. Squared Legendre polynomial representing the angular transverse structure of a mode's intensity. The three examples have $l = 53$ and $m = 53,\ 52,$ and 51 respectively. Calculations are done for the same sphere as in Fig. II.1.

The forms of $\vec{L}$, $\vec{M}$ and $\vec{N}$ in spherical coordinates are:

$$\vec{L}_{\substack{e\\o}ml} = \frac{\partial}{\partial r} Z_l(kr) P_l^m(\cos\theta) \begin{matrix}\cos\\ \sin\end{matrix} m\varphi \hat{r} + \frac{1}{r} Z_l(kr) \frac{\partial P_l^m(\cos\theta)}{\partial\theta} \begin{matrix}\cos\\ \sin\end{matrix} m\varphi \hat{\theta}$$

$$\mp \frac{m}{r\sin\theta} Z_l(kr) P_l^m(\cos\theta) \begin{matrix}\sin\\ \cos\end{matrix} m\varphi \hat{\varphi}$$

$$\vec{M}_{\substack{e\\o}ml} = \mp \frac{m}{\sin\theta} Z_l(kr) P_l^m(\cos\theta) \begin{matrix}\sin\\ \cos\end{matrix} m\varphi \hat{\theta} - Z_l(kr) \frac{\partial P_l^m(\cos\theta)}{\partial\theta} \begin{matrix}\cos\\ \sin\end{matrix} m\varphi \hat{\varphi} \qquad \text{(II.7)}$$

$$\vec{N}_{\substack{e\\o}ml} = \mp \frac{l(l+1)}{kr} Z_l(kr) P_l^m(\cos\theta) \begin{matrix}\cos\\ \sin\end{matrix} m\varphi \hat{r} + \frac{1}{kr} (krZ_l)' \frac{\partial P_l^m(\cos\theta)}{\partial\theta} \begin{matrix}\cos\\ \sin\end{matrix} m\varphi \hat{\theta}$$

$$\mp \frac{m}{kr\sin\theta} (krZ_l)' P_l^m(\cos\theta) \begin{matrix}\sin\\ \cos\end{matrix} m\varphi \hat{\varphi},$$

where $Z_l\,(kr)$ stands for a spherical Bessel function of different kinds: spherical Bessel of the 1st kind inside and spherical Hankel of the 1st kind outside of the sphere. For isotropic media, the fields can be expanded in the basis of $\vec{M}$ and $\vec{N}$ only.

The incident plane wave field (polarized in the *x*-direction) can be written as:

$$\vec{E}_{inc} = E_0 \hat{x} e^{ikz}$$
$$\vec{H}_{inc} = \frac{k^{ex} E_0}{i\mu^{ex}\omega} \hat{y} e^{ikz}, \qquad \text{(II.8)}$$

or in spherical coordinates:

$$\vec{E}_{inc} = E_0(\sin\theta\cos\varphi\hat{r} + \cos\theta\cos\varphi\hat{\theta} - \sin\varphi\hat{\varphi}) e^{ikr\cos\theta}$$
$$\vec{H}_{inc} = \frac{k^{ex} E_0}{i\mu^{ex}\omega} (\sin\theta\sin\varphi\hat{r} + \cos\theta\sin\varphi\hat{\theta} + \cos\varphi\hat{\varphi}) e^{ikr\cos\theta}. \qquad \text{(II.9)}$$

Consequently the incident field can be presented as a superposition of $\vec{M}$ and $\vec{N}$ vectors with $m = 1$ in the form:

$$\vec{E}_{inc} = E_0 \sum_l (\alpha_l \vec{M}^{(1)}_{o1l} + \beta_l \vec{N}^{(1)}_{e1l})$$
$$\vec{H}_{inc} = \frac{k^{ex} E_0}{i\mu^{ex}\omega} \sum_l (\alpha_l \vec{N}^{(1)}_{o1l} + \beta_l \vec{M}^{(1)}_{e1l}) \qquad \text{(II.10)}$$

where the superscript (1) indicates spherical Bessel functions of the first kind (because the field is finite at r = 0). The orthogonality relations give expressions for the coefficients α and β:

$$\alpha_l = i^l \frac{2l+1}{l(l+1)}$$
$$\beta_l = -i^{l+1} \frac{2l+1}{l(l+1)} \tag{II.11}$$

The interior and exterior fields fields in general can be written as:

$$\vec{E} = E_0 \sum (A_{\substack{o \\ e}}{}_{ml} \vec{M}_{\substack{o \\ e}}{}_{ml} + B_{\substack{o \\ e}}{}_{ml} \vec{N}_{\substack{o \\ e}}{}_{ml}),$$
$$\vec{H} = \frac{kE_0}{i\omega\mu} \sum (A_{\substack{o \\ e}}{}_{ml} \vec{N}_{\substack{o \\ e}}{}_{ml} + B_{\substack{o \\ e}}{}_{ml} \vec{M}_{\substack{o \\ e}}{}_{ml}). \tag{II.12}$$

The summation is over all three indices. If the field has a radial component and all A_{ml} are zero and all the amplitudes are represented by coefficients B_{ml} the oscillations are of an electric type, also known as transverse magnetic (TM). If B_{ml} are zero and all the amplitudes are represented by coefficients A_{ml} the oscillations are of a magnetic type, or transverse electric (TE).

In the case of Mie scattering, only those components of $\vec{M}$ and $\vec{N}$ that are in the incident field can be present in the resulting interior and exterior fields. Thus these fields can be written as:

$r < a$

$$\vec{E}^{in} = E_0 \sum_l \frac{(2l+1)i^l}{l(l+1)} \left[a_l^{in} \vec{M}_{o1l}^{(1)} - i b_l^{in} \vec{N}_{e1l}^{(1)} \right]$$
$$\vec{H}^{in} = \frac{k^{in} E_0}{i\omega\mu^{in}} \sum_l \frac{(2l+1)i^l}{l(l+1)} \left[a_l^{in} \vec{N}_{o1l}^{(1)} - i b_l^{in} \vec{M}_{e1l}^{(1)} \right] , \tag{II.13}$$

$$r>a \qquad \begin{aligned} \vec{E}^{ex} &= \vec{E}_{inc} + E_0 \sum_l \frac{(2l+1)i^l}{l(l+1)} \left[a_l^{ex} \vec{M}_{o1l}^{(3)} - i b_l^{ex} \vec{N}_{e1l}^{(3)} \right] \\ \vec{H}^{ex} &= \vec{H}_{inc} + \frac{k^{ex} E_0}{i\omega\mu^{ex}} \sum_l \frac{(2l+1)i^l}{l(l+1)} \left[a_l^{ex} \vec{N}_{o1l}^{(3)} - i b_l^{ex} \vec{M}_{e1l}^{(3)} \right] \end{aligned} . \qquad \text{(II.14)}$$

Continuity conditions for the tangential components of the fields give the expressions for the expansion coefficients a_l and b_l. Matching the θ components of the electric and magnetic fields at $r = a$ gives:

$$\begin{aligned} & a_l^{in} j_l(k^{in}a) = a_l^{ex} h_l(k^{ex}a) + j_l(k^{ex}a), \\ & \frac{1}{\mu^{in}} a_l^{in} [k^{in} a j_l(k^{in}a)]' = \frac{1}{\mu^{ex}} a_l^{ex} [k^{ex} a h_l(k^{ex}a)]' + \frac{1}{\mu^{ex}} [k^{ex} a j_l(k^{ex}a)]'. \end{aligned} \qquad \text{(II.15)}$$

An identical equation relates b_l^{in} and b_l^{ex}. Coefficients for the resulting scattered field found from the equations above are:

$$\begin{aligned} a_l^{ex} &= -\frac{\mu^{in} j_l(k^{in}a)[k^{ex} a j_l(k^{ex}a)]' - \mu^{ex} j_l(k^{ex}a)[k^{in} a j_l(k^{in}a)]'}{\mu^{in} j_l(k^{in}a)[k^{ex} a h_l(k^{ex}a)]' - \mu^{ex} h_l(k^{ex}a)[k^{in} a j_l(k^{in}a)]'} \\ b_l^{ex} &= -\frac{\mu^{in} j_l(k^{ex}a)[k^{in} a j_l(k^{in}a)]' - \mu^{ex} (k^{in}/k^{ex})^2 j_l(k^{in}a)[k^{ex} a j_l(k^{ex}a)]'}{\mu^{in} h_l(k^{ex}a)[k^{in} a j_l(k^{in}a)]' - \mu^{ex} (k^{in}/k^{ex})^2 j_l(k^{in}a)[k^{ex} a h_l(k^{ex}a)]'}. \end{aligned} \qquad \text{(II.16)}$$

The prime means a total derivative over the argument of the spherical Bessel function i.e. over $k^{ex}r$ or $k^{in}r$, evaluated at $r = a$.

We have a resonant condition for TE modes when the denominator of a_l^{ex} is zero and the resonant condition for TM modes when the denominator of b_l^{ex} is zero. These conditions lead to the characteristic equations. The values of k^{ex} for which the field is enhanced (or equivalently, the resonant frequencies) can be determined from them. The characteristic equations are:

for TE modes: $$\mu^{in} \frac{j_l(k^{in}a)}{[k^{in} a j_l(k^{in}a)]'} = \mu^{ex} \frac{h_l(k^{ex}a)}{[k^{ex} a h_l(k^{ex}a)]'}, \qquad \text{(II.17)}$$

for TM modes: $$\mu^{ex}(k^{in}/k^{ex})^2 \frac{j_l(k^{in}a)}{[k^{in}aj_l(k^{in}a)]'} = \mu^{in} \frac{h_l(k^{ex}a)}{[k^{ex}ah_l(k^{ex}a)]'}. \qquad \text{(II.18)}$$

These equations have many roots, so they determine a large set of complex wavevectors (eigenfrequences) for a sphere of given radius. The real part determines the eigenfrequency of the mode and the imaginary part determines the radiative decay of the mode. A third index q is introduced, which indicates to which root one or another value of the wavevector corresponds; $q-1$ gives the number of the radial nodes of a given mode inside the sphere. The characteristic equations are independent of index m, which means that the modes of an ideal sphere are degenerate over this index. When the body has some ellipticity this degeneracy is removed.

In general the structure of the electric field (TE or TM modes, not restricted to those that can be excited by an incident plane wave) of a dielectric sphere placed in vacuum is:

$$\begin{aligned} &E_r(r,\theta,\varphi,t) = 0 \\ \text{TE:}\quad &E_\theta(r,\theta,\varphi,t) = -E_0 \frac{im}{\sin\theta} P_l^m(\cos\theta) Z_l(k_{ql}^{TE} r) e^{im\varphi} e^{-i\omega_{ql}^{TE} t} \\ &E_\varphi(r,\theta,\varphi,t) = E_0 \frac{\partial P_l^m(\cos\theta)}{\partial\theta} Z_l(k_{ql}^{TE} r) e^{im\varphi} e^{-i\omega_{ql}^{TE} t}, \end{aligned} \qquad \text{(II.19)}$$

$$\begin{aligned} &E_r(r,\theta,\varphi,t) = -E_0 l(l+1) P_l^m(\cos\theta) \frac{Z_l(k_{ql}^{TM} r)}{k_{ql}^{TM} r} e^{im\varphi} e^{-i\omega_{ql}^{TM} t} \\ \text{TM:}\quad &E_\theta(r,\theta,\varphi,t) = -E_0 \frac{\partial P_l^m(\cos\theta)}{\partial\theta} \frac{1}{k_{ql}^{TM} r} [k_{ql}^{TM} r Z_l(k_{ql}^{TM} r)]' e^{im\varphi} e^{-i\omega_{ql}^{TM} t} \\ &E_\varphi(r,\theta,\varphi,t) = -E_0 \frac{imP_l^m(\cos\theta)}{\sin\theta} \frac{1}{k_{ql}^{TM} r} [k_{ql}^{TM} r Z_l(k_{ql}^{TM} r)]' e^{im\varphi} e^{-i\omega_{ql}^{TM} t}. \end{aligned} \qquad \text{(II.20)}$$

Inside the sphere: $Z_l = j_l$ (spherical Bessel functions); and outside: $Z_l = h_l^{(1)}$ (spherical

Hankel functions), and $k_{ql}^{TE(TM)} = k^{in}$ is replaced by $\frac{k_{ql}^{TE(TM)}}{n^{in}} = k^{ex}$, where n^{in} is the refractive index of the dielectric sphere.

II.2 Whispering gallery resonances

Whispering-gallery modes are those that are closely confined to the surface of the sphere. They are characterized by a large index *l*, an index *m* that is close to *l*, and a radial index *q* that is close to 1. Modes with $q = 1$ and $m = l$ are classified as fundamental WGMs. The eigenfrequencies of these modes can be determined to good approximation by solving the characteristic equation with the Bessel functions approximated by Airy functions. The imaginary part of the wavevector for these modes is extremely small. This makes the quality factor, defined for the radiative losses, an astronomically huge number. It rapidly decreases with increasing radial index *q*.

II.2.1 Resonance frequencies

The numerical solutions of (II.17) and (II.18) give the resonant frequency of a particular TE or TM mode respectively. A useful analytical formula is derived in [43] by asymptotic expansion of the characteristic equations in powers of $(l+1/2)^{1/3}$. It is accurate for small radial numbers (q) and large azimuthal numbers (l) and takes into account perfect spherical resonators (first four terms in (II.21)). The eccentricity dependence of the resonant frequency is obtained by using perturbation theory (for small eccentricity e) as discussed in [44].

The resonance frequencies of WGMs can be written as:

$$\nu_{qlm}^{TE(M)} = \frac{\omega_{qlm}^{TE(M)}}{2\pi} =$$
$$= \delta\left[\left(l+1/2\right)+\zeta_q\left(\frac{l+1/2}{2}\right)^{1/3}-\Delta^{TE(M)}+\frac{3\zeta_q^2}{20}\left(\frac{l+1/2}{2}\right)^{-1/3}\pm e^2\left(\frac{l-|m|}{2}\right)\right], \tag{II.21}$$

where
$$\delta = \frac{c}{2\pi n^{in} a} \tag{II.22}$$

is the free spectral range for an azimuthally symmetric resonator of radius a – by direct analogy with Fabry-Perot cavities. Also, ζ_q is the negative of the q^{th} zero of the Airy function, $\Delta^{TE} = \tilde{n}/\sqrt{\tilde{n}^2-1}$ or $\Delta^{TM} = (\tilde{n}\sqrt{\tilde{n}^2-1})^{-1}$ is a polarization dependent frequency shift, $\tilde{n} = n^{in}/n^{ex}$ is the relative index, and $e = \sqrt{(a_+^2 - a_-^2)/a_+^2}$ is the eccentricity in terms of the major (a_+) and minor (a_-) radii, taken with the plus sign for oblate spheres and the minus sign for prolate spheres.

II.2.2 Mode volume

The spatial confinement of light is described by a mode volume, an important performance parameter that depends on the particular cavity geometry. There are several definitions of mode volume depending on the physical problem that is studied.

In the scope of quantum optics, where a strong electric field per photon is considered, mode volume is related to the electromagnetic field distribution normalized to its maximum value [45]:

$$V_{qlm} = \frac{\int_{V_Q} \varepsilon(r)\left|\psi_{qlm}(r,\theta,\varphi)\right|^2 dV}{\max\left|\psi_{qlm}(r,\theta,\varphi)\right|^2}, \tag{II.23}$$

where V_Q is a quantization volume. Integration is over the space inside the sphere plus

the regions where the field is evanescent.

Another definition of mode volume is used when nonlinear effects are described [13]:

$$V_{qlm} = \frac{\left(\int\limits_{V_Q} \left| \psi_{qlm}(r,\theta,\varphi) \right|^2 dV \right)^2}{\int\limits_{V_Q} \left| \psi_{qlm}(r,\theta,\varphi) \right|^4 dV}, \tag{II.24}$$

which leads to an approximate relation for volume of modes with $q = 1$:

$$V_{1lm} \approx 3.4\pi^{3/2} \left(\frac{\lambda}{2\pi n} \right)^3 l^{11/6} \sqrt{l - m + 1}. \tag{II.25}$$

As described in [45], the mode volume predicted by (II.25) is a factor of 1.8 smaller than the mode volume calculated by (II.23) for any *l*. Here and further in this work the refractive index inside the resonator is designated with *n* instead of n^{in}.

II.2.3 Quality factor

The complex eigenfrequencies, determined by solving (II.17) and (II.18), can be written in the form:

$$\tilde{\omega}_{ql} = \omega_{ql} - i\Gamma_{ql}. \tag{II.26}$$

The imaginary part determines the decay of a given mode. This decay is caused by the radiation of the wave from the sphere. For a dielectric sphere with a large *l* index this is a very small number. Cavity loss in general is expressed in terms of quality factor. The radiative quality factor of the modes is defined by the ratio of the real and imaginary parts of the eigenfrequencies,

$$Q_{rad} = \frac{\omega_{ql}}{\Gamma_{ql}}. \tag{II.27}$$

Approximate analytical formulas for Q_{rad} are given in [46].

For large l numbers (at optical wavelengths, for spheres of radius > 10 μm), losses related to absorption (on the surface and inside of the sphere) and scattering (due to surface roughness and inhomogeneities of the material density) are much more significant than the radiative losses and determine the quality factor. The overall Q-factor can be decomposed into the following terms:

$$\frac{1}{Q_{total}} = \frac{1}{Q_{rad}} + \frac{1}{Q_{abs}} + \frac{1}{Q_{ssc}} + \frac{1}{Q_{Vsc}} + \frac{1}{Q_{coupling}} = \frac{1}{Q_{in}} + \frac{1}{Q_{coupling}}, \tag{II.28}$$

where the various terms are defined below. This separation of losses is valid for weak loss – when only a small fraction of optical energy is lost in a round trip [47].

The losses related to absorption by the resonator medium are given by the expression [13],

$$Q_{abs}^{-1} = \frac{\alpha\lambda}{2\pi n_{eff}}, \tag{II.29}$$

where α is the absorption coefficient of the resonator medium and n_{eff} is the effective refractive index. In many cases the strongest absorption losses are caused by an absorbing layer (usually water) on the surface of the resonator. In these cases equation (II.29) is modified by multiplying the Q_{abs} by the ratio of the absorbing layer thickness to the effective thickness of the particular WGM, which is discussed in [46]. An approximation of this ratio [48] is:

$$\frac{\delta}{\sqrt{\lambda 2a}}, \tag{II.30}$$

δ being the thickness of the layer, $\delta << \lambda/2\pi$.

Losses caused by surface scattering are calculated [46] by treating the surface as an ensemble of independently scattering particles, much smaller than the wavelength. An approximate formula for the inverse of the surface scattering related losses, Q_{ssc}, is given in [48],

$$Q_{ssc} = \frac{3n^2\left(n^2+2\right)^2}{\left(4\pi\right)^3\left(n^2-1\right)^{5/2}}\frac{\lambda^{7/2}\left(2a\right)^{1/2}}{h^2B^2} \tag{II.31}$$

where h is the mean height and B is the mean size of surface inhomogeneities. As shown in the same paper, experimentally measured Q-factors follow a $(2a)^{1/2}$ dependence on the radius. Q_{Vsc}^{-1} is from the loss due to scattering within the mode volume. $Q_{coupling}^{-1}$ represents the energy loss due to input/output coupling. Q_{in} represents the effect of all intrinsic losses combined, and can be written as:

$$Q_{in} = \frac{2\pi n_{eff}}{\lambda\alpha_{in}}, \tag{II.32}$$

where α_{in} is an effective intrinsic loss coefficient. Q_{total} thus relates to the time photons are circulating inside the cavity, before decaying through the processes mentioned above, as:

$$Q_{total} = 2\pi\frac{c}{\lambda}\tau_{ph}. \tag{II.33}$$

II.3 Surface plasmon resonances

For small metal particles (high surface to volume ratio), the resonance caused by the collective oscillation of conduction electrons is known as the surface plasmon of the

particles. The position, the intensity, and the width of the peaks in the spectra of small metal particle assemblies depend on: the size and shape of the particles, the dielectric constant of the surrounding medium [49], and their proximity and orientation in the assembly. The Mie scattering analysis developed in section II.1 can be applied to a collection of identical spheres if: (1) the distance between spheres is much larger than the wavelength so that the spheres scatter independently, (2) the spheres are randomly placed to avoid interference effects, and (3) the optical density of the medium is small enough (i.e. a nonabsorbing medium) to assume the same incident intensity on each sphere. The last assumption is used to apply the far field approximation to the scattered fields E^{ex} and H^{ex}, although the exact derivations are also obtainable as described in [50]. The energy dissipation in such a system caused by scattering and absorption is described in terms of extinction σ_{ext} and scattering σ_{sc} cross sections. The extinction cross section is defined as the rate of energy dissipation divided by the incident intensity, and relates to an easily measurable quantity, the extinction coefficient γ, defined by:

$$\frac{I}{I_0} = e^{-\gamma x}, \tag{II.34}$$

with

$$\gamma = N\sigma_{ext}, \tag{II.35}$$

where I_0 is the intensity of the incident light beam, I is the intensity after the beam has traveled through a distance x of an absorbing and scattering medium, and N is the number of spheres per unit volume. Using the Optical Theorem, the extinction σ_{ext} and scattering σ_{sc} cross sections are calculated from Mie theory [50]:

$$\sigma_{ext} = \frac{2\pi}{k^2}\sum_{l=1}^{\infty}(2l+1)\,\mathrm{Re}(a_l + b_l), \tag{II.36}$$

$$\sigma_{sc} = \frac{2\pi}{k^2}\sum_{l=1}^{\infty}(2l+1)(|a_l|^2 + |b_l|^2). \tag{II.37}$$

The absorption cross section is:

$$\sigma_{abs} = \sigma_{ext} - \sigma_{sc}. \tag{II.38}$$

In order to compare attenuation of light by a material in bulk with that in different particulate states it is useful to define a volume attenuation coefficient [51] which is the extinction cross section per unit particle volume:

$$\gamma_v = \frac{\sigma_{ext}}{V} = \frac{\gamma}{NV}. \tag{II.39}$$

This formulation gives a way to compare samples with different volume fractions (*NV*) of particles in the ensemble. To calculate the attenuation of samples containing spheres and rods it is useful to express the volume extinction coefficient (for spheres) in the form [49]:

$$\frac{\gamma}{NV} = \frac{3\pi\varepsilon_m^{3/2}}{\lambda A^3}\sum_{l=1}^{\infty}(2l+1)\,\mathrm{Re}(a_l + b_l), \tag{II.40}$$

where λ is the wavelength of the incident light, ε_m the dielectric constant of the surrounding medium, and $A = \frac{2\pi a\varepsilon_m^{1/2}}{\lambda}$, a being the radius of the spheres. When the particle size is much smaller than the wavelength ($a << \lambda$) the absorption is caused mainly by the electric dipole oscillations, which simplifies the sum in (II.40) to the following equation independent of *a*:

$$\frac{\gamma}{NV} = \frac{18\pi\varepsilon_m^{3/2}}{\lambda}\frac{\varepsilon_2}{(\varepsilon_1 + 2\varepsilon_m)^2 + \varepsilon_2^2}, \tag{II.41}$$

where $\varepsilon_1 = n^2 + \kappa^2$ and $\varepsilon_2 = 2n\kappa$ are the components of the dielectric function of the particle $\varepsilon_p = \varepsilon_1 + i\varepsilon_2$ defined by $\varepsilon_p = (n + i\kappa)^2$, κ being the absorption index.

II.4 Gold nanorod surface plasmon calculations

Gans [52] extended Mie's theory within the dipole approximation. The particles are usually characterized by their aspect ratio (AR – ratio between the length and the width of the particle). The plasmon resonance for nanorods consists of two bands – the higher energy one corresponds to oscillation of the electrons perpendicular to the longer rod axis and is referred to as the transverse plasmon resonance; the lower energy band is due to oscillations of electrons along the rod and known as longitudinal plasmon. As the aspect ratio increases, the energy separation between the resonance frequencies of the two plasmon bands increases.

According to Gans' theory the extinction coefficient of small, randomly oriented, non-interacting particles is [49]:

$$\frac{\gamma}{NV} = \frac{18\pi\varepsilon_m^{3/2}}{3\lambda}\sum_j \frac{(1/P_j^2)\varepsilon_2}{\left(\varepsilon_1 + \frac{1-P_j}{P_j}\varepsilon_m\right)^2 + \varepsilon_2^2}, \qquad \text{(II.42)}$$

where P_j is the depolarization factor corresponding to each of the axes A, B and C. For elongated ellipsoids (A> B=C):

$$P_B = \frac{1-e^2}{e^2}\left(\frac{1}{2e}\ln\frac{1+e}{1-e} - 1\right), \qquad P_B = P_C = \frac{1-P_A}{2} \qquad \text{(II.43)}$$

where $$e = \sqrt{1 - \frac{1}{(AR)^2}}, \qquad \text{(II.44)}$$

and *AR* (aspect ratio) is the ratio of the longer to the shorter axes of the rod.

Calculations for the extinction coefficient of small spheres (II.41) and ellipsoids (II.42) are made using experimentally measured data for the refractive index *n* and the absorption index κ for gold [53]. The optical properties are described in terms of the complex dielectric function of the particles $\varepsilon_p = \varepsilon_1 + i\varepsilon_2$. An interpolation method was used to draw smooth curves, because only 30 data points were available in the wavelength region of interest. This may add some error, in addition to the experimental one, to the calculated values of $\varepsilon_1(\omega)$ and $\varepsilon_2(\omega)$. Figure II.3 shows the calculated plots of the extinction coefficient as a function of wavelength. Figure II.3(a) shows that for the particles with a small aspect ratio in air, there is only one peak that is observable. In a medium with small ε_m (air), the two plasmon modes, transverse and longitudinal, are less separated. Separation is also a function of the aspect ratio. For particles with AR < 3 in air, the transverse plasmon mode overlaps with the longitudinal, which has a significantly higher intensity. Figure II.3(b) shows how sensitive the longitudinal plasmon mode is to changes in the dielectric constant of the surrounding medium. Using the longitudinal surface plasmon mode as a sensor for changes in the surrounding medium has been proposed [54].

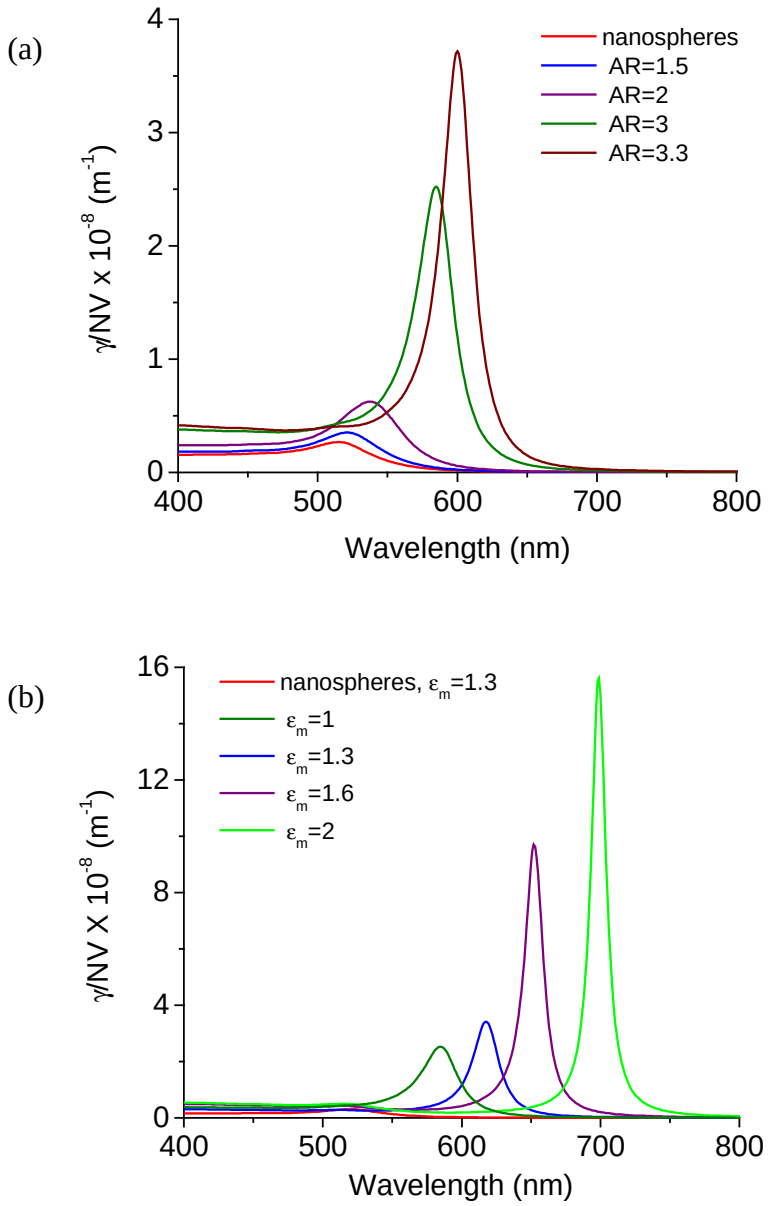

Figure II.3. Dependence of the extinction coefficient on (a) aspect ratio (AR) for ε_m = 1 and (b) dielectric constant of the medium (ε_m) for AR = 3.

In a real sample an ensemble of different size spheres and rods with different aspect ratios will be present. To model this, a Gaussian distribution of aspect ratios of rods was assumed, with a mean of 3.5 and a standard deviation of 0.5. The different plots

in Fig. II.4 take into account the contributions of different volume fractions of nanospheres.

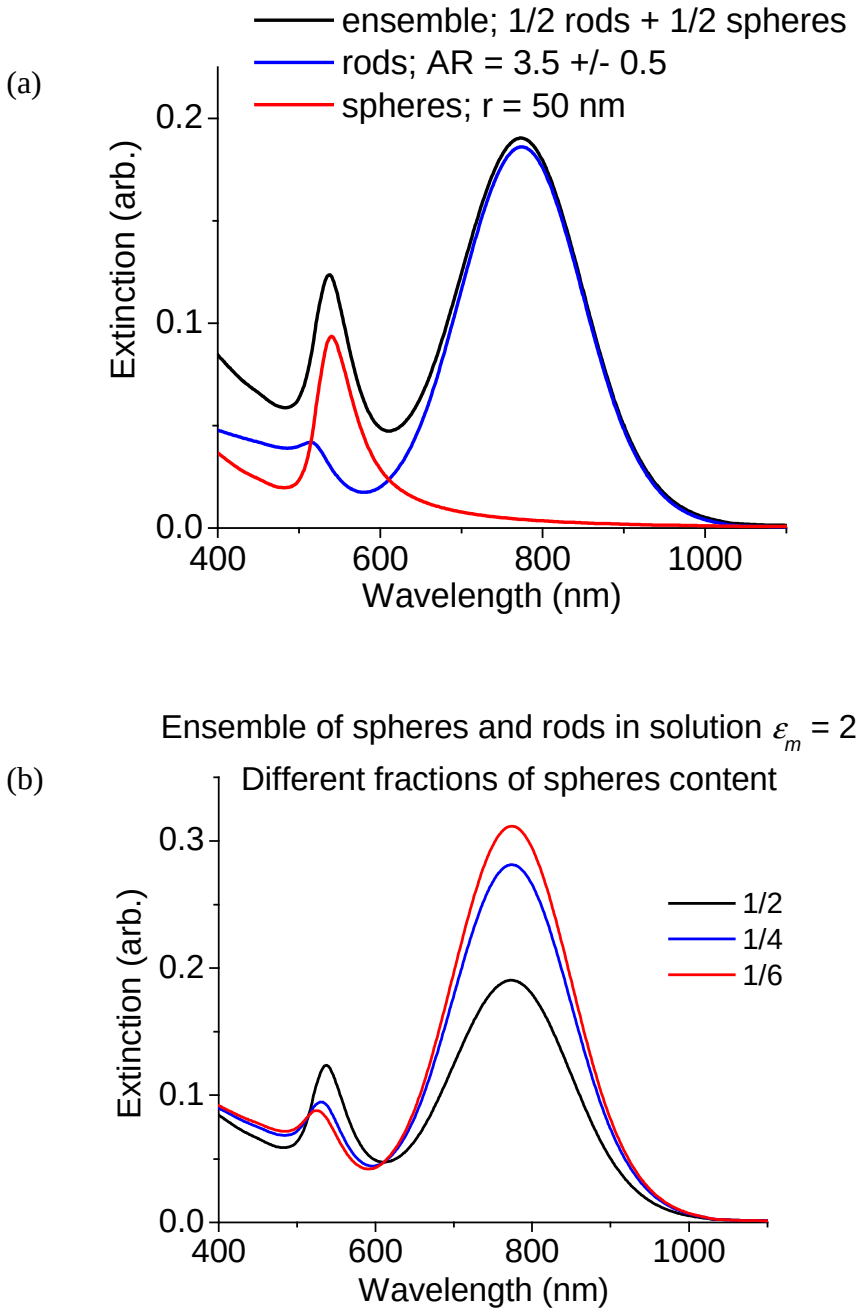

Figure II.4. Ensembles of rods and spheres in solution ($\varepsilon_m = 2$). (a) equal fractions of rods and spheres, (b) various fractions of spheres.

This model adequately describes the extinction spectra of low concentration solutions of Au nanoparticles and is comparable to many experimental results given in the literature [55]. A common mistake is to attribute the shorter wavelength peak to the transverse mode of the rods only, while it is mostly the effect of the presence of nanospheres.

II.5 Conclusions

This chapter describes light scattering by spherical particles. WGM resonances are derived as a generalization of Mie scattering resonances in dielectric spheres. Surface plasmon resonances are described on the basis of the same theory in the case of metallic particles. The extinction coefficient is defined for spherical and elliptical particles. An original contribution in this chapter is the calculation of the extinction coefficient for an ensemble of spheres and rods with a Gaussian distribution of aspect ratios. The model compares well with experimental results for particles in a dilute solution. As a continuation of this work, calculations of the extinction coefficient for a dense ensemble of particles on a surface can be developed and compared with the experimental data.

CHAPTER III

COUPLING INTO MICRORESONATORS USING TAPERED OPTICAL FIBERS

III.1 Evanescent coupling

Evanescent coupling uses tunneling of the photons between the waveguide and the resonator. Approximate phase-matching of the wavevectors is required for efficient coupling. It means the velocity of the excitation wave is equal to the velocity of the confined wave. Phase velocities are determined by the effective refractive index of the optical mode. Evanescent coupling can be realized using total internal reflection in a prism or the evanescent field of an eroded, side-polished, or tapered optical fiber. Prism coupling has also been used for efficient excitation of surface plasmons [56] as well as to excite WGMs of microspheres [57]. Tapered optical fibers have proven to have several advantages over other evanescent couplers – low loss, small transverse dimensions, and more precise control over the coupling between the optical fiber and the resonator.

III.2 Ring cavity model describing coupling between the waveguide and the resonator

A four-mirror ring cavity model, shown in Fig. III.1, was developed to describe the coupling to and from the microsphere cavity.

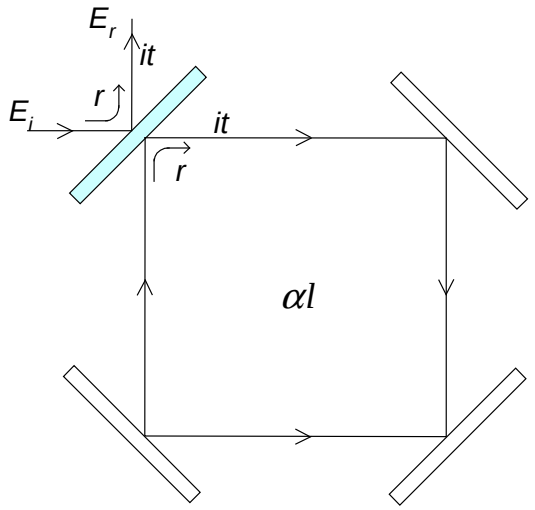

Figure III.1. Ring cavity model. Three of the mirrors are 100% reflecting and one is partially transmitting with an amplitude reflection coefficient r and amplitude transmission coefficient it. Power conservation leads to $t^2 = 1 - r^2$. l is the round trip path length and α is the effective loss coefficient inside the cavity. The internal power losses in one round trip are αl.

The ring cavity model is a valid analog to a fiber-coupled microresonator. Its results are comparable to the results of coupled mode theory with the assumption that only a single fiber mode is excited. However, light coupled from the microresonator to the tapered fiber may excite many fiber modes, all of which, except the fundamental HE_{11}, will be lost after propagating a short distance along the fiber. Fortunately, by placing the resonator at the proper tapered-fiber diameter it is possible to make the losses into higher order modes negligible thus validating the ring-cavity model. The ring cavity may have one or two partially transmitting mirrors with *r* and *it* coefficients of reflection and transmission. The internal round trip loss of the cavity is αl ($l = 2\pi a$, the microresonator circumference) and $r^2 + t^2 = 1$ (lossless mirrors).

The reflected field E_r can be written as:

$$E_r(t) = rE_i(t) - t^2 e^{i\delta} e^{-\frac{\alpha l}{2}} \sum_{n=0}^{\infty} E_i(t-(n+1)\tau_{rt})(re^{i\delta}e^{-\frac{\alpha l}{2}})^n, \tag{III.1}$$

$$\text{or} \quad \frac{E_r}{E_i} \simeq \frac{r - e^{-\frac{\alpha l}{2}} e^{i\delta}}{1 - re^{-\frac{\alpha l}{2}} e^{i\delta}} \tag{III.2}$$

in the case of a cw incident field, $E_i(t) = E_i$; τ_{rt} is the round trip time and $\delta = \frac{2\pi nl}{c}(\nu - \nu_0)$ is the phase detuning from the resonance ν_0. The total loss can be separated into internal (αl) and coupling ($t^2 = T$) losses. The ratio of the coupling to internal loss is defined by

$$x = \frac{T}{\alpha l}. \tag{III.3}$$

In the ring-cavity model, the fiber throughput signal is the power of the reflected field from the partially transmitting mirror. It is described by the reflectivity *R*:

$$R = \left|\frac{E_r}{E_i}\right|^2 = \frac{\left(\frac{1-x}{1+x}\right)^2 + \theta^2}{1+\theta^2} \qquad \text{(III.4)}$$

where $\theta \equiv -\frac{2\delta}{T+\alpha l}$. θ is the detuning of the resonance mode from the injected light in units of the half-linewidth. At resonance the fiber throughput power can be found from:

$$R = \frac{P_{thro}}{P_{in}} = \left(\frac{1-x}{1+x}\right)^2 . \qquad \text{(III.5)}$$

There are three regimes that characterize the coupling:

Undercoupling: Coupling between the waveguide and the cavity is weak. Losses related to coupling are smaller than intracavity losses $(x<1)$. In the four-mirror-cavity model the amplitude of the directly reflected field (first term on right hand side of (III.1)) is greater than the amplitude of the field transmitted out through the mirror (second term on right hand side of (III.1)).

Overcoupling: In the overcoupled regime $(x>1)$ the losses related to coupling are greater than the intracavity losses. The amplitude of the field transmitted out through the mirror in this case is greater than the amplitude of the directly reflected field. In the case of strong overcoupling, it can reach twice the amplitude of the directly reflected field.

Critical coupling: When the internal losses are equal to the coupling losses $(x=1)$, the two terms have the same amplitude. However, since the field transmitted out through the mirror is phase shifted by π, the two fields interfere destructively and the fiber throughput vanishes. The power carried by the waveguide transfers completely to the cavity mode.

The shape of the resonance dip in the tapered fiber throughput power, when the frequency of the exciting wave is varied, is characterized by the dip depth *M* as a function

of detuning θ:

$$M(\theta) = 1 - R = \frac{\frac{4x}{(1+x)^2}}{1+\theta^2} = \frac{M_0}{1+\theta^2}, \tag{III.6}$$

where

$$M_0 = \frac{4x}{(1+x)^2} \tag{III.7}$$

is the dip depth on resonance.

Cavity buildup factor

The cavity buildup factor can be defined as the ratio of internal cavity power to incident power. In the case of one coupler (or, equivalently, one partially transmitting mirror) it is:

$$A_0 = \left(\frac{P_{cav}}{P_{in}} \right) = \frac{4x}{(1+x)^2} \frac{1}{\alpha_i l}. \tag{III.8}$$

In terms of quality factors, the cavity buildup factor is:

$$A_0 = \frac{\lambda}{\pi^2 n_{eff} a} \frac{Q_{total}^2}{Q_c} = \frac{\lambda}{\pi^2 n_{eff} a} Q_{total} \frac{1+x}{4} M_0. \tag{III.9}$$

In the case of critical coupling, the cavity buildup factor is:

$$\frac{P_{cav}}{P_{in}} = \frac{\lambda Q_{total}}{2\pi^2 n_{eff} a}. \tag{III.10}$$

This equation shows that the circulating power can be significantly enhanced inside the high quality factor cavity and therefore the threshold for lasing or other nonlinear effects can be significantly reduced.

III.3 Coupling from tapered optical fibers – in space and in time

Modes of a tapered optical fiber can be modeled as modes of a cylindrical dielectric waveguide. As a single mode optical fiber is adiabatically tapered to diameters below the core diameter, a fraction of the propagating mode extends outside of the fiber. This is the part of the field that can tunnel into a WGM of the cavity. It can be approximated as an exponentially decaying field. The decay constant of the taper field is given by the expression [58]:

$$\begin{aligned} \gamma_f &= \alpha_0 \frac{K_1(\alpha_0 r_f)}{K_0(\alpha_0 r_f)}, \\ \alpha_0 &= \sqrt{\beta_f^2 - k_0^2 n_0^2} \end{aligned} \tag{III.11}$$

where K_1 and K_0 are modified Hankel functions of the first and zero order, β_f is the propagation constant of the fiber mode, and r_f is the taper radius.

The propagation constant is a function of the taper diameter. It varies with position along the taper transition region of the fiber. This can be used for phase matching of the whispering-gallery modes of the cavity. Figure III.2 shows the effective index, which is proportional to the propagation constant, of two modes in the fiber as a function of taper radius.

In the taper transition region, power can transfer from the fundamental HE_{11} mode to other modes that overlap with it. Due to symmetry considerations these are modes of the same family, HE_{1m}. Mode-matching requirements and the assumption of a slow (near adiabatic) transition leave the HE_{12} mode as the dominant possibility for power transfer.

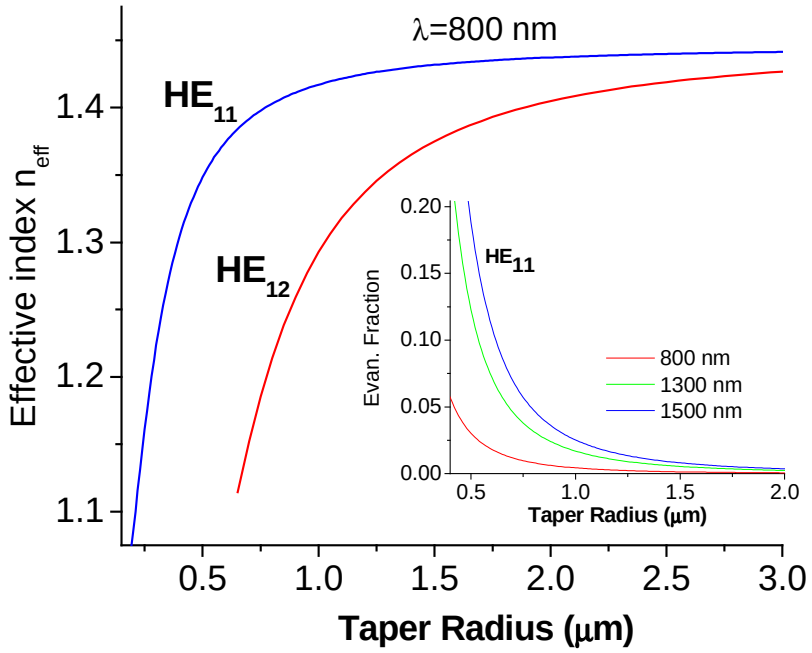

Figure III.2. Calculated effective index n_{eff} of the HE_{11} fundamental and HE_{12} modes of a tapered fiber as a function of the taper radius. The inset shows the evanescent fraction of the HE_{11} mode for three different wavelengths.

If the fiber is tapered adiabatically [59], only the fundamental HE_{11} mode propagates through the fiber. Conditions for adiabatic tapering of an optical fiber are thoroughly discussed by Love [59, 60]. If a microcavity is placed in the vicinity of the tapered region of a single mode fiber, where the field is evanescent, the fundamental fiber mode overlaps with the WGMs of the cavity. In general, the power transfer from the fiber to the cavity modes is caused by a polarization current produced in the cavity by the field of the fiber within the cavity. Analogously the field of the cavity produces a polarization current inside the fiber. Coupling of modes is considered in time and in space. A matrix model of the coupling amplitudes [61] correctly describes the coupling behavior, even in the case of strong coupling. If the coupling is assumed weak, the time rate and the spatial rate of change of the amplitudes of coupled modes are expressed by first order derivatives: higher order derivatives are ignored. Weak coupling is a good approximation when the rate of change per cycle or per wavelength is small, as it is in our applications.

An approach to the coupling problem, which treats the coupling in space, is presented in [62]. It is based on the model of distributed coupling between a WGM in the resonator (with field amplitude A) and modes in the waveguide (B_k). If we consider coupling between one WGM and only one waveguide mode the system of coupled differential equations to be solved is:

$$\begin{aligned} \frac{dA}{dz} &= i\beta_s A + \kappa_{sf} B \\ \frac{dB}{dz} &= i\beta_f B + \kappa_{fs} A \end{aligned} \tag{III.12}$$

where β_s and β_f are the propagation constants of the mode in the sphere and in the fiber, and κ_{sf} and κ_{fs} are the coupling coefficients. Restrictions on κ_{sf} and κ_{fs} are imposed by

power conservation. If coupling is weak the power in the two modes is evaluated disregarding the coupling. Coupling from the cavity to several modes of the waveguide is usually allowed (because of simultaneously satisfying near-phase-matched conditions for these modes). This behavior is studied in [63]. The findings show that when the HE_{11} mode is matched to a fundamental WGM, coupling from the cavity to several higher-order fiber modes can be significant.

Coupling in time is also found under the assumption of weak coupling. When the perturbation of the cavity and the waveguide mode is small (weak coupling), then the slowly varying amplitude approximation can be made. It is valid when the cavity field $A(t)$ satisfies the relation $A(t+\tau_{rt}) \approx A(t) - \tau_{rt}\frac{dA}{dt}$, where τ_{rt} is the cavity round trip time. This coupling-of-modes formalism is given by H. Haus in [47] and is also used in [58]. Coupling in time between the mode of the waveguide and the mode of the cavity is described by two coupled first order differential equations. Energy conservation relates the two coupling coefficients. The results are equivalent to the results obtained with the four-mirror ring cavity model.

III.4 Fabrication of tapered optical fibers

III. 4.1 Details of the tapered-fiber equipment

In this work tapered optical fibers were prepared from SMF-28 (for propagation of 1550 nm light; 8.2 μm core diameter and 125 μm cladding diameter), SBA (for propagation of 800 nm light; 5 μm core diameter and 125 μm cladding diameter), and SE (for λ = 780 nm) commercially available optical fibers. The fibers were stripped ½ inch

(jacket removed). They were stretched while being heated, along the stripped portion, with a hydrogen torch. The flame was controlled by a flowmeter. To control the stretching a computer interfaced machine was designed. A view of the fiber taper pulling machine is given in Fig. III.3.

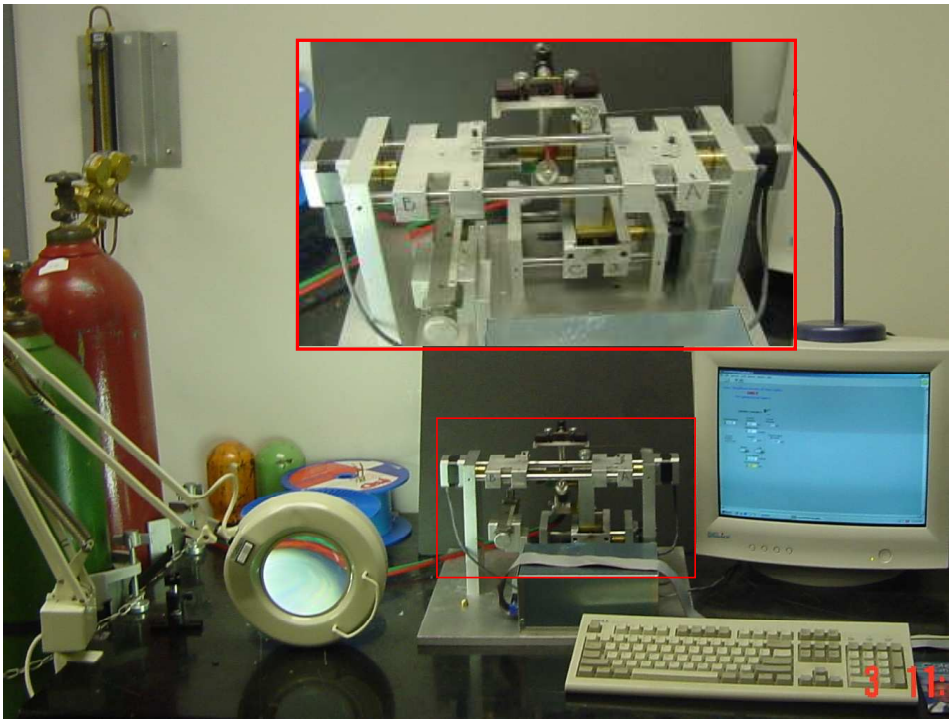

Figure III.3. Equipment for making tapered optical fibers; the inset shows a close look at the taper puller.

A LabView program controls the motion of the machine. As a result of that, it allows for control of the tapered fiber parameters (fiber waist and stretched length). Two motors pull the fiber in opposite directions, which results in two gradual taper transitions with a region of constant diameter between them. The motors can be actuated and controlled simultaneously for achieving adiabatic taper transitions for single mode propagation. They can also be controlled individually for a more sudden transition, which can be optimized for two-mode propagation. For the experiments discussed in this dissertation the aim was to achieve adiabatic tapers. The third motor, controlling the torch motion, was operated in constant speed mode, periodically reversing the direction of motion ("flame brush") in an interval controlled by the program. The gas flow was optimized depending on the composition of the different optical fibers to be tapered.

III. 4.2 Method for monitoring of single mode propagation in the process of tapering

Fibers are pulled at a constant speed of 4.4 mm/min. The two motors are pulling at 2.2 mm/min in opposite directions. The usual setting of flame brush speed is 120 mm /min and the brush length is L_b = 6.5 mm. The final diameter of the tapered fiber can be set and it determines how much the fiber is stretched. In the current setting of the taper-puller program the final diameter $D(= 2\ r_f)$ is calculated as:

$$D = D_0 e^{-\frac{x}{2L_b}}, \qquad \text{(III.13)}$$

where D_0 is the initial diameter and x is the increase in the fiber length resulting from the displacement of the motors. The optimal taper profile, such that the resultant taper transition is adiabatic at minimal stretching, can be achieved by making the brush length a function of x, and is discussed in George Farca's dissertation [64].

To monitor the process of tapering we injected laser light into the optical fiber and recorded the output power at the other end while the fiber was heated and stretched. If the stretching is done too fast to be considered adiabatic, the initial single HE_{11} mode in the fiber core is coupled to higher order modes of the same symmetry (HE_{12}) as the light propagates through the taper transition. Light coupled into the higher order modes will be lost in the cladding after the second taper transition, reducing transmission through the tapered fiber during the process of tapering. If the power transmitted through the tapered fiber remains close to the power transmitted before tapering, the tapered fiber transition can be considered adiabatic. Figure III.4 represents the transmitted power through four fibers during the process of tapering. Fibers 1 and 2 are SBA fibers and the laser light that propagates through them has a wavelength of 830 nm. Fibers 3 and 4 are SMA-28 fibers, propagating 1570 nm light. Fiber 1 was stretched from its original diameter of 125 μm and fiber 2 was first etched to about 80 μm diameter and then stretched. It was found that the initial reduction of the cladding diameter (e.g., by etching in a solution of HF) results in a more gradual transition as light goes from core guided to cladding guided. While a single mode is being guided by the core, the cladding diameter can be reduced abruptly down to diameters such that the evanescent fraction of the core-guided mode is still completely confined in the cladding. The smaller core diameters of SBA and SE fibers require longer taper transition lengths in order to achieve the same angle of transition at the point when light becomes cladding guided in comparison with SMA fibers.

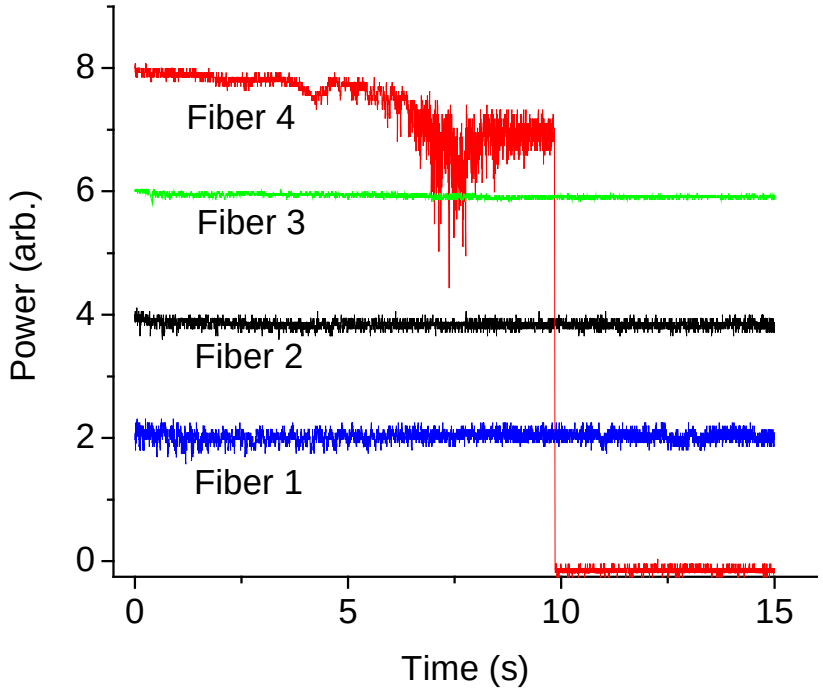

Figure III.4. Transmitted power through a fiber during the process of tapering as a function of time.

To have the same evanescent fraction of the mode in the air, the final diameter has to be smaller when the wavelength is shorter. This also adds to the longer transition length of these tapers. One solution for this is an initial reduction of the fiber diameter using hydrofluoric (HF) acid etching. Fiber 3 is a SMA-28 fiber. Fibers 1-3 were stretched to a 2 μm final diameter using a brush length of 6.5 mm. Fiber 4 was also an SMA fiber, but the transition was made more sudden, by using a brush length of 4 mm. The fiber broke before reaching the final diameter. The initial power in each fiber was normalized to 8 (arbitrary units) and the graphs were offset for clarity. The loss in each of these tapered fibers is: Fiber 1 – 2.4%; Fiber 2 – 2%; Fiber 3 – 4.2%; and Fiber 4 (before break) – 13.4%. The unetched SBA fiber 1 shows small amplitude sinusoidal variations of the power, which is characteristic for two mode propagation with a small fraction of the power coupled into the higher order mode.

III.5 Experimental realization of coupling from a tapered fiber to a microsphere resonator

A portable taper holder was designed to allow for the tapered fiber fabrication to be separate from the coupling setup. Figure III.5 shows an image of the fiber holder and the precise way of attaching the tapered fiber to it. This setting allows for perfect horizontal alignment of the fiber and it also allows for two tapered fibers to be placed parallel to each other (up to 300 μm apart). This design significantly facilitated the experiments. A sketch of two fiber holders positioned close together is given in Fig. III.6.

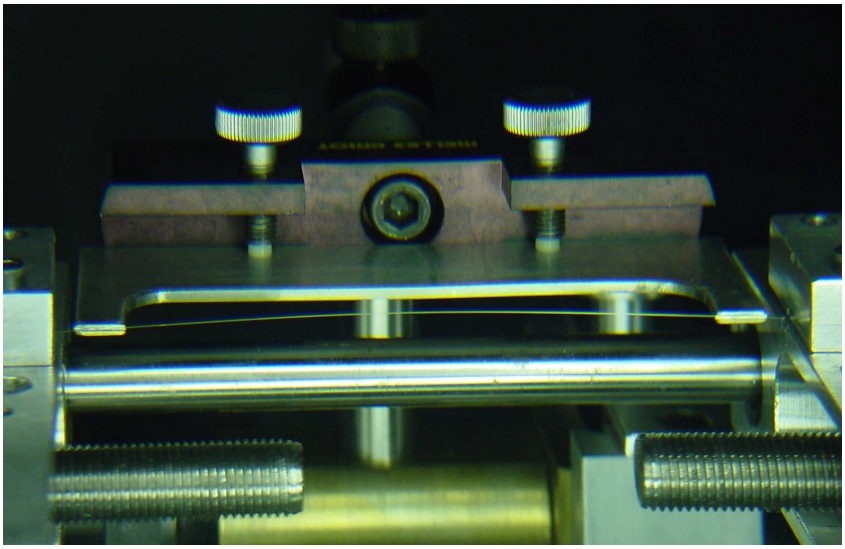

Figure III.5. Fiber attachment to the fiber holder after pulling.

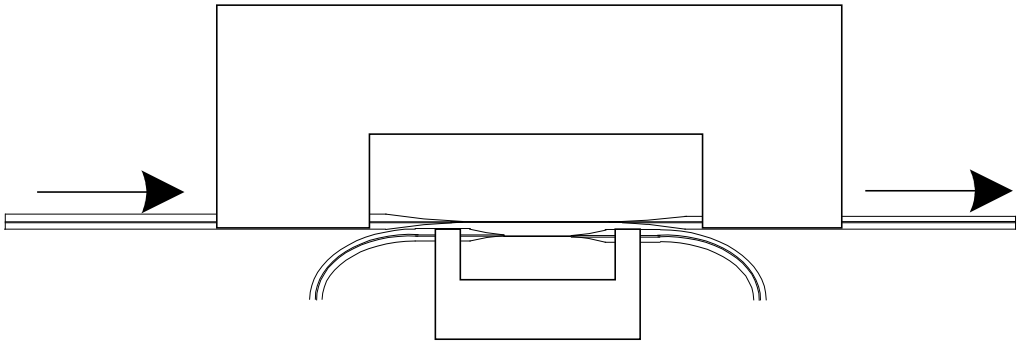

Figure III.6. Two tapered fibers placed parallel at a distance comparable with the microsphere diameter.

An example of evanescent coupling from a tapered fiber to the microsphere resonator is given in Fig. III.7. The fiber was tapered to 2 μm diameter, the radius of the sphere was 225 μm, and the laser wavelength was 1550 nm. The graph shows the throughput power as a function of scanning frequency. Different plots are taken as the distance between the sphere and the fiber changes. At large distances, only several undercoupled modes are observed. These modes are of the same radial order, but different polar orders, because they are equally spaced in frequency. As the distance decreases the overlap of sphere and fiber modes increases, so the coupling becomes stronger. The dip-depth of the modes increases and the dip-width also slightly increases. New classes of modes with different radial orders appear in the spectra. Modes with the highest *Q*-factor appear when the distance between the sphere and the fiber is significantly reduced, showing the fact that the extension of the lowest order radial modes outside the dielectric sphere is smallest. When the fiber touches the sphere (last plot) the relative distance among modes changes, reflecting the slight change in the effective refractive index n_{eff} of the microsphere modes due to the fiber presence.

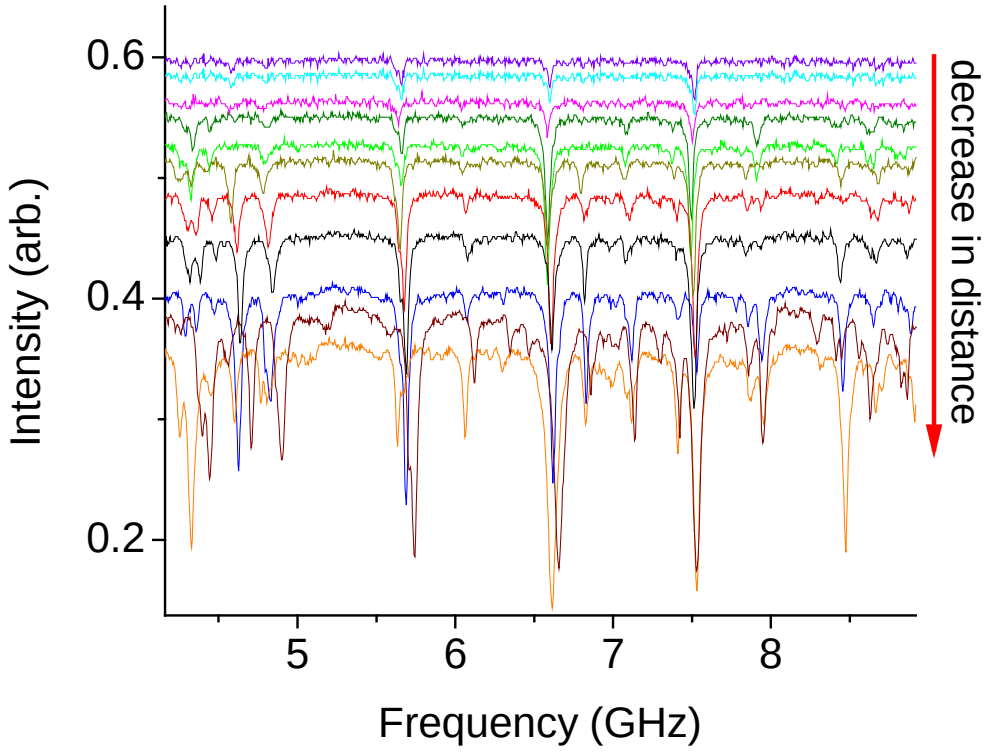

Figure III.7. Evolution of WGMs with decrease of the distance between the microsphere and the fiber.

III. 6 Conclusions

In this chapter I discuss the evanescent coupling between a microsphere resonator and an optical fiber. A ring cavity model was used to describe the shape of the cavity mode in terms of cavity losses. It was shown that the resonance dip depth is a function of the ratio of the coupling loss to the intrinsic loss. This ratio was used to define the three coupling regimes; undercoupled, overcoupled, and critically coupled. An expression for the cavity buildup factor was also found. In the experimental part of this chapter I describe a fiber puller device that was designed in the course of this work for making tapered fibers. We achieved low-loss adiabatically tapered fibers. A method for monitoring and possibly controlling the tapering process was described, which also has significance for making fiber tapers that are deliberately non-adiabatic. Finally an experimental demonstration of the evolution of the WGM spectrum with decreasing fiber-resonator distance was also given.

CHAPTER IV

SEMICONDUCTOR QUANTUM DOTS

IV.1 Introduction

Semiconductor quantum dots (QDs) are studied in this work as a gain medium for a WGM laser based on a high quality microsphere resonator. This chapter discusses the main ideas about carrier confinement in zero dimensional structures such as quantum dots, provides calculations for the parameters of colloidal HgTe QDs, the semiconductor gain material chosen for our WGM laser, and gives some comparison to other QD materials used in laser design.

When charge carriers are confined in all three dimensions in 10-nm-scale semiconductor structures, essentially trapped within potential wells, their motion is quantized. This creates atomic-like states in semiconductors. Quantum confinement gives rise to significant modification of the energy band structure and the density of states in these materials. When the semiconductor dimensionality is reduced the state density distribution acquires sharper features (Fig. IV.1), which in the case of a quantum dot (0-D – zero dimensionality) become δ-functions. The energy spacing between the atomic-like states increases as the dot size decreases.

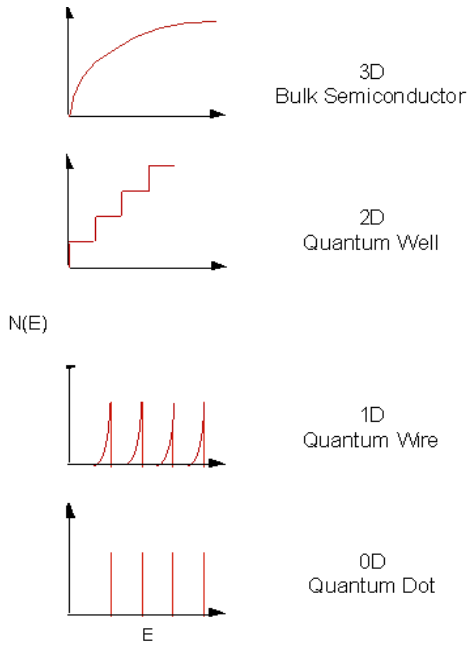

Figure IV.1 Density of states for decreasing dimensionality of the gain medium. (Reproduced from [65].)

In our whispering-gallery microlaser stimulated recombination of electron-hole pairs takes place in the quantum dot region, where the confinement of the carriers and of the optical mode enhance the interaction between carriers and radiation. The population inversion (i.e. creation of electrons and holes) necessary for lasing occurs more efficiently as the active material is scaled down from bulk (3-dimensional) to quantum dots (0-dimensional). However, the laser operation depends not only on the absolute size of the nanostructures in the active region, but also on the uniformity of size. A large distribution of sizes broadens the density of states, producing gain spectra similar to that of bulk material. As an active medium for the proposed laser we choose colloidally prepared HgTe nanoparticles (Fig. IV.2) because of their strong room temperature infrared luminescence [27] and the strong quantum confinement that can be achieved in

these nanoparticles. Depending on the size distribution and the method of preparation these nanoparticles can show a broad luminescence spectrum (1000 – 2000 nm) over the range of strategic telecommunication windows.

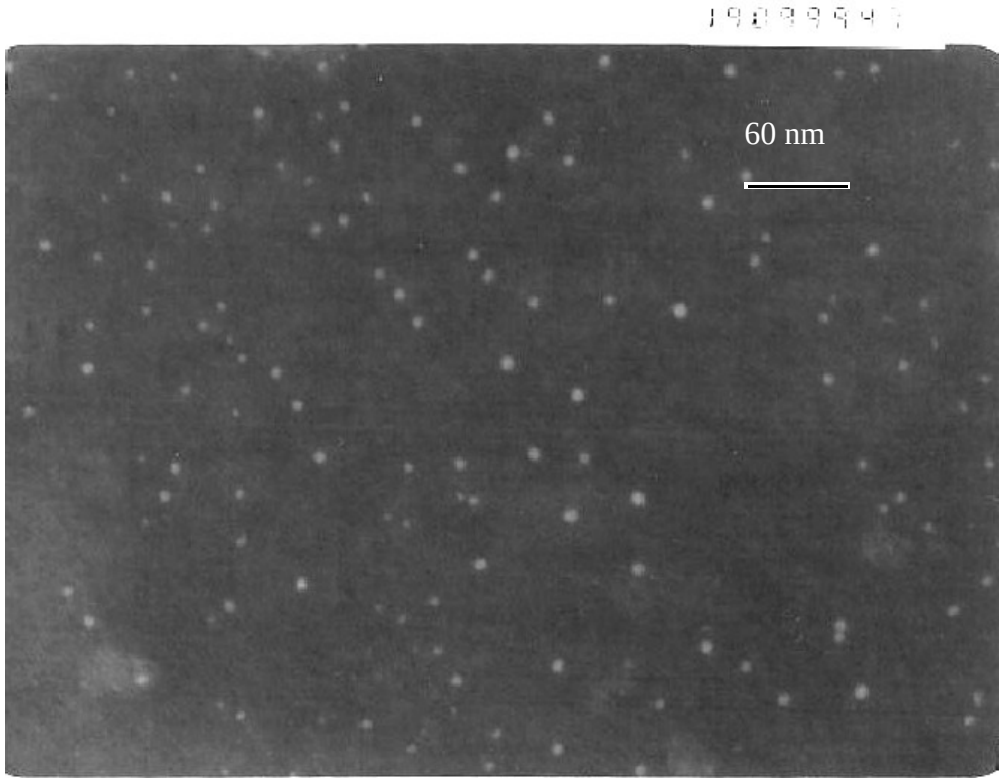

Figure IV.2. TEM image of colloidal HgTe nanoparticles deposited on a formvar grid.

Table IV.1 shows a comparison of emission range, typical diameters, and exciton Bohr radius for several of the most investigated colloidal semiconductor quantum dots. The ratio of Bohr radius to the radius of the QD is a measure of the strength of carrier confinement in a dot.

Material	Emission range (nm)	Diameters (nm)	Exciton Bohr radius (nm)
CuCl	~ 400	3	0.7
CdS	550 – 800	3 – 7	2.8
CdSe	465 – 640	1.9 – 6.7	6
PbS	850 – 2100	2.2 – 9.8	20
InAs	800 – 1300	2 –7	34
HgTe	900 – 2000	2 – 10	39.8
PbSe	1200 – 2340	3.5 – 9	46
InSb	650 – 1330	8 – 12	54

Table IV.1. Comparison of emission range and exciton Bohr radius for different colloidal nanocrystals.

Narrow bandgap materials, such as HgTe, PbSe, and InSb are desirable to investigate the strong confinement limit of QDs. Among these materials, strong confinement for both electrons and holes is easily achievable for PbSe because the electron and hole effective masses are nearly equal. For example, compare the electron and hole Bohr radii of these materials with the typical sizes of QDs in Table IV.1: InSb, a_h = 2 nm; HgTe, a_h= 2.6 nm; PbSe, $a_e = a_h$ = 23 nm.

IV.2 Model describing luminescence in QDs

This model is based on the effective mass approximation. It assumes that the carriers in the dot behave as particles in a spherical well. The energy eigenvalues differ

from the case of a free particle in a spherical potential well but can be formally expressed in terms of effective masses. The equations in this section (IV.2) are written in the CGS system of units. Equation (IV.1) corresponds to a parabolic band approximation used to describe an electron in a periodic crystal lattice:

$$E(k) = \frac{\hbar^2 k^2}{2m^*}, \tag{IV.1}$$

where m^* is an effective mass,

$$m^{*-1} = \frac{1}{\hbar^2}\frac{d^2E}{dk^2}\bigg|_{k=0} = \text{const}. \tag{IV.2}$$

To describe the electronic levels of HgTe nanoparticles attached to the dielectric glass surface we have used two models: a particle in an infinite spherical well and a particle in a finite spherical well. We assumed a potential well depth of 5 eV for the finite spherical well. The well depth is determined by the nature of the capping layer molecules. In all our experiments we have used thioglycolic acid capped nanoparticles.

The nanoparticles are attached to a dielectric medium (thin PDDA layer covering fused silica) with a dielectric constant ε_2 less than that of the semiconductor nanocrystal ε_{QD}. The dielectric confinement (caused by the difference in dielectric constants) gives rise to surface polarization effects [66] because of an interaction of the electron and hole inside a crystallite with induced image charges outside. The finite well depth results in a lowering of energy, compared to the energy of the same state with the assumption of an infinite well.

IV.2.1 Infinite potential well

Quantum confinement: In a quantum dot the electronic states are quantized and the energy levels become discretized. The simplest model of a quantum dot is the particle in a spherical box of radius *R* with an infinite potential step [67]. In this model the Schrödinger equation is solved separately for electrons and holes:

$$\left(-\frac{\hbar^2}{2m_i^*}\nabla^2 + V(\vec{r})\right)\psi_i(\vec{r}) = E_i\psi_i(\vec{r}), \tag{IV.3}$$

where *i* denotes either electron or hole, m_i^* is electron (hole) effective mass, $\psi_i(\vec{r})$ is the electron (hole) wave function, $V(\vec{r}) = 0$ for $r < R$ and $V(\vec{r}) = \infty$ for $r > R$. This boundary condition implies that the wave function vanishes outside the boundary. Another assumption of this model is that it ignores the Coulomb interaction between the electron and the hole. Solving Schrödinger's equation (IV.3) in spherical coordinates we can find the eigenenergies E_i:

$$E_i = \frac{\hbar^2}{2m_i^*}\left(\frac{\alpha_{ql}}{R}\right)^2, \tag{IV.4}$$

where α_{ql} is the *q*th zero of a spherical Bessel function of order *l*. Therefore the energy separation between the two lowest energy levels ($l = 0$ and $l = 1$) is given by:

$$\Delta E_{1,0} = 10.3\frac{\hbar^2}{2m_i^* R^2}. \tag{IV.5}$$

In addition, carriers in the dot (electrons and holes) as charged particles interact via the Coulomb potential and form a quasiparticle, an exciton [68], that corresponds to a hydrogen-like bound state of an electron-hole pair. Coulomb interaction between the localized carriers modifies the particle-in-a-box model depending on the strength of the

confinement in comparison to the electrostatic energy. The Hamiltonian describing an exciton in an infinite well can be written as:

$$H = -\frac{\hbar^2}{2m_e^*}\nabla_e^2 - \frac{\hbar^2}{2m_h^*}\nabla_h^2 - \frac{e^2}{\varepsilon_{QD}\left|\vec{r}_e - \vec{r}_h\right|} + V\left(\vec{r}_e\right) + V\left(\vec{r}_h\right) \tag{IV.6}$$

where $\vec{r}_e$ and $\vec{r}_h$ are the coordinates of an electron and a hole, and ε_{QD} is the dielectric constant of the nanocrystal.

An exciton, similarly to the hydrogen atom, is characterized by the exciton Bohr radius

$$a_B = \frac{\varepsilon_{QD}\hbar^2}{\mu e^2}, \tag{IV.7}$$

where μ is the electron-hole reduced effective mass

$$\mu^{-1} = m_e^{*-1} + m_h^{*-1}, \tag{IV.8}$$

and by the exciton Rydberg energy

$$E_R = \frac{e^2}{2\varepsilon_{QD}a_B}. \tag{IV.9}$$

For optical (interband) transitions we need to consider the energy separation between electron and hole states. If the Coulomb interaction can be ignored then the energy separation between the electron and hole states is:

$$E_{ql} = E_g + \frac{\hbar^2}{2\mu}\left(\frac{\alpha_{ql}}{R}\right)^2. \tag{IV.10}$$

On the other hand, from (IV.7) and (IV.9) the exciton binding energy in the bulk is given by

$$E_R = \frac{\hbar^2}{2\mu a_B^2}. \tag{IV.11}$$

In making the determination of how many electron and hole energy levels to be included in a calculation, an important parameter is the ratio of the dot radius to the exciton Bohr radius in bulk material. In the strong confinement regime, the energy separations (IV.10) are much larger than the exciton binding energy (IV.11), which is a measure of electron-hole Coulomb interaction, so the exciton ground state is composed of the lowest-energy electron and hole states. The criterion for strong confinement is [66]:

$$\left(\frac{R}{a_B}\right) \ll 1 \qquad \text{(IV.12)}$$

As the size of the QD increases and the energy separations of the quantized electron and hole states become equal to or smaller than the exciton binding energy, mixing of the states has to be considered. The valence band in HgTe (zincblende structure) has *p*-like character ($\hbar$ angular momentum). The spin of the electron interacts with the magnetic field produced by the orbital motion. Due to spin-orbit interaction the valence band splits into a 4-fold degenerate band (with total angular momentum $F = 3/2$) and a 2-fold band ($F = 1/2$). The degenerate states at the zone center are represented by different curvatures in the multiband effective mass approximation model and are called heavy hole (HH), light hole (LH), and spin-orbit split-off bands. Mixing of the HH and LH bands described by a multi-band envelope-function model [69] gives more accurate predictions of the lowest-energy hole eigenstates.

For HgTe ($m_e^* = 0.03\, m_0$, $m_h^* = 0.44\, m_0$, where m_0 is the free electron mass), the Bohr radius and Rydberg energy are:

$$a_B = 39.75 \text{ nm}, \quad \text{and} \quad E_R = 0.86 \text{ meV}.$$

The static dielectric constant of bulk HgTe is $\varepsilon_{QD} = 21$ [70]. The electron and hole energy separations for a 2 nm radius HgTe spherical QD are:

$$\Delta E_{e1,0} = 5.1\times10^{-19}\ \text{J} = 3.2\ \text{eV} = 123\ k_B T_{room} \text{ and}$$

$$\Delta E_{h1,0} = 3.5\times10^{-20}\ \text{J} = 0.22\ \text{eV} = 8.4\ k_B T_{room}.$$

Thus for R = 2 nm average size (HgTe nanoparticles), the strong confinement regime is a valid assumption. Thermal population of the higher energy levels can be neglected if the separation between energy levels is large compared to the thermal energy $k_B T_{room} = 26\ \text{meV} = 4\times10^{-21}\ \text{J}$ at $T = 300\ \text{K}$.

Dielectric confinement: The dielectric confinement effect arises when the semiconductor QDs are surrounded by a medium with a relatively small dielectric constant. The electric field lines between the charged particles inside the nanocrystal pass through a medium with a smaller dielectric constant resulting in enhanced Coulomb interaction between the electron and the hole. This effect is more pronounced in QDs with a radius equal to or smaller than the Bohr radius because of the stronger penetration of the electric field lines into the surrounding medium. The electron and the hole motion in these structures is strongly affected by the dielectric boundary.

To take into account the surface polarization energy, which arises from the differences between the dielectric constants of the nanocrystal and the surrounding medium, the electron–hole Hamiltonian is supplemented with the potential energy of electron and hole interaction with the induced polarization field [71]:

$$H = -\frac{\hbar^2}{2m_e}\nabla_e^2 - \frac{\hbar^2}{2m_h}\nabla_h^2 - \frac{e^2}{\varepsilon_{QD}\left|\vec{r}_e - \vec{r}_h\right|} + \frac{e^2}{2R}\sum_{l=1}^{\infty}\alpha_l\left[\left(\frac{\left|\vec{r}_e\right|}{R}\right)^{2l} + \left(\frac{\left|\vec{r}_h\right|}{R}\right)^{2l}\right] - \\ -\frac{e^2}{R}\sum_{l=1}^{\infty}\alpha_l\left(\frac{\left|\vec{r}_e\right|\left|\vec{r}_h\right|}{R^2}\right)^l P_l\left(\cos\Theta_{eh}\right) \qquad \text{(IV.13)}$$

where $\vec{r}_e$ and $\vec{r}_h$ are the respective coordinates of electron and hole, P_l is the Legendre polynomial of the l-th order, and Θ_{eh} is the angle between $\vec{r}_e$ and $\vec{r}_h$. α_l is defined by

$$\alpha_l = \frac{(l+1)(\varepsilon-1)}{\varepsilon_{QD}(l\varepsilon + l + 1)}, \qquad \text{(IV.14)}$$

where $\varepsilon = \frac{\varepsilon_{QD}}{\varepsilon_2}$.

The first two terms represent the kinetic energy, and the third term is the direct Coulomb interaction between an electron and a hole. The last two terms account for the surface polarization energy. The first of these terms is the self-energy of electron and hole due to their own image charges and the second is the mutual interaction energy between electron and hole via image charges. The expression of the dielectric confinement energy for an exciton is dependent on the shape of the quantum dot. This problem has been treated with the variational approach [72-74], and it has been found that in the strong confinement limit ($R << a_B$) the Coulomb term contribution to the ground state energy is even greater than in the bulk monocrystal. Thus the excitonic energy spectra in the strong confinement regime are expected to be strongly modified by this dielectric confinement effect.

The exciton energy measured as a deviation from the bulk band gap energy E_g in the strong confinement limit can be written as an expansion [75]

$$E_{exc} - E_g = \left(\frac{a_B}{R}\right)^2 R_y \left[A_1 + \frac{R}{a_B} A_2 + \left(\frac{R}{a_B}\right)^2 A_3 + ... \right], \qquad \text{(IV.15)}$$

with the small parameter $R/a_B << 1$.

The first coefficient A_1 corresponds to the roots of the Bessel function. The second coefficient A_2 describes the Coulomb term and takes different values for 1*s*1*s*, 1*p*1*p*, and other states [74]. It also contains terms that arise from the surface polarization energy. The third coefficient A_3 is also a function of the dielectric constant ratio $\frac{\varepsilon_{QD}}{\varepsilon_2}$ [76].

Taking the coefficients A_2 and A_3 from the literature [77] we calculated the energy (in eV) of the lowest exciton state as a function of the QD radius (in nm):

$$E_{1s1s} = -0.146 + \frac{\pi^2 1.308}{R^2} - \frac{0.081}{R} - 0.001. \qquad \text{(IV.16)}$$

A plot of this dependence is presented in Fig. IV.2. The 1*s*1*s* exciton state is the lowest energy state for a transition in a QD. The quantum dots are assumed spherical.

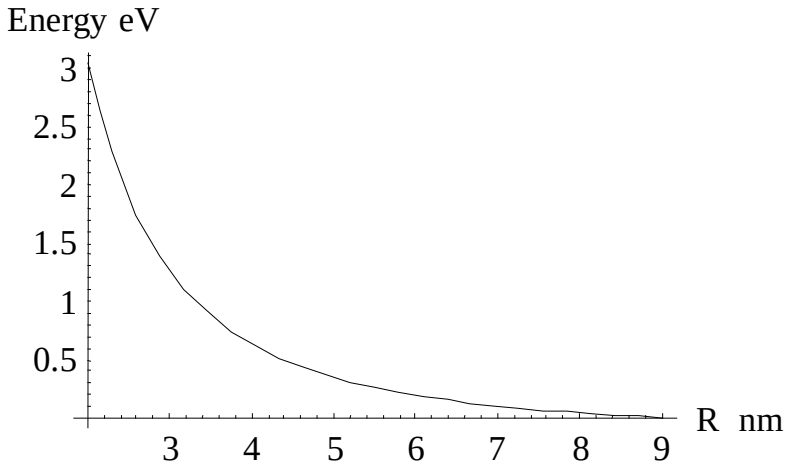

Figure IV.3. The energy of the lowest exciton energy level vs quantum dot radius.

The experimentally measured first excitonic peak of HgTe nanoparticles of average size around 2 nm radius, suspended in water, is at about 1.3 eV (see Ch. V) while according to the graph it should appear at 3 eV. The deviation of the theoretical prediction from the experimentally measured values shows that the boundary constraint of the infinite well model is not valid for small size QDs.

IV.2.2 Finite potential well

Formula (IV.16) diverges in the limit $R \to 0$, while in the real systems E should be bounded by the work function of the semiconductor embedded in the surrounding matrix material. A spherical region in which the potential is less than that of the surroundings ($V(r) = -V_0$ for $r < R$, and $V(r) = 0$ for $r > R$) serves as a finite quantum well. The radial quantum number comes from the solution of the Schrödinger equation in spherical coordinates. The requirement that the radial part of the wave function $\Re(r)$ has to be finite at $r = 0$ leaves the odd parity solution to an equivalent one-dimensional problem.

The interior solution is $\Re(r) = Aj_l(\alpha r)$ for $r < R$, (IV.17)

and the exterior solution is $\Re(r) = Bh_l^{(1)}(i\beta r)$ for $r > R$, (IV.18)

where $j_l(\alpha r)$ is a spherical Bessel function and $h_l^{(1)}(i\beta r)$ is a spherical Hankel function, and α and β are:

$$\alpha = \left[\frac{2\mu\left(V_0 - |E|\right)}{\hbar^2}\right]^{1/2} \quad \text{for } r < R,$$
$$\beta = \left(\frac{2\mu|E|}{\hbar^2}\right)^{1/2} \quad \text{for } r > R. \tag{IV.19}$$

$E < 0$ for bound state energy levels.

The radial quantum number and consequently the bound energy levels are obtained by requiring that $(1/\Re)(d\Re/dr)$ be continuous at $r = R$. This condition, applied to interior and exterior solutions, for *l* = 0, 1, and 2 respectively leads to:

For *l* = 0

$$(\alpha R)\cot(\alpha R) = -(\beta R)$$
$$(\alpha R)^2 + (\beta R)^2 = \frac{2\mu V_0 R^2}{\hbar^2}. \qquad \text{(IV.20)}$$

For *l* = 1

$$\frac{\cot(\alpha R)}{(\alpha R)} - \frac{1}{(\alpha R)^2} = \frac{1}{(\beta R)} + \frac{1}{(\beta R)^2}$$
$$(\alpha R)^2 + (\beta R)^2 = \frac{2\mu V_0 R^2}{\hbar^2}. \qquad \text{(IV.21)}$$

For *l* = 2

$$\frac{\left(4 - \frac{9}{(\alpha R)^2}\right) + \left(\frac{9}{(\alpha R)} - (\alpha R)\right)\cot(\alpha R)}{\left(\frac{3}{(\alpha R)^2} - 1\right) - \frac{3}{(\alpha R)}\cot(\alpha R)} = -\left[(\beta R) + \frac{1 + \frac{6}{(\beta R)} + \frac{9}{(\beta R)^2}}{1 + \frac{3}{(\beta R)} + \frac{3}{(\beta R)^2}}\right] \qquad \text{(IV.22)}$$
$$(\alpha R)^2 + (\beta R)^2 = \frac{2\mu V_0 R^2}{\hbar^2}.$$

The lowest energy levels for the *s*, *p*, and *d* bands of HgTe nanoparticles are found upon graphical solution of these equations. The results are plotted versus dot radius and presented in Figure IV.4.

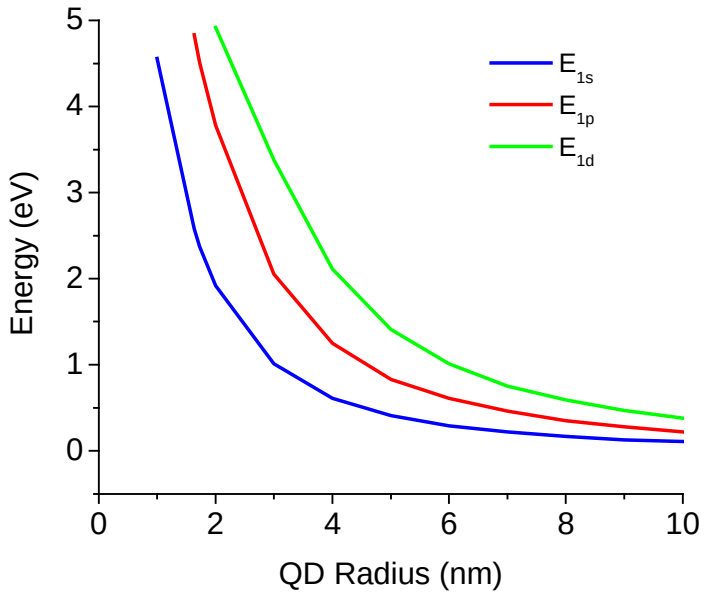

Figure IV.4. Exciton energy levels vs QD radius. Energy levels for different *l* (angular momentum quantum number) are plotted assuming a finite (5 eV) depth quantum well.

Although these results still differ from experimental photoluminescence (PL) spectra, they give some qualitative understanding of the nanoparticles' behavior:

1. The exciton binding energy depends on the size of the QD, depth of the potential well, and strength of the Coulomb interaction.
2. There is a critical size of the nanocrystal (radius less than 0.63 nm) under which there is no confined state. The emission wavelength can be changed either by changing nanocrystal composition (for example $Hg_xCd_{1-x}Te$) or by controlling the average size and size distribution.

IV.3 Optical gain in quantum dots

The overall gain spectrum produced from an active layer of nanoparticles is broadened both homogeneously and inhomogeneously. The natural linewidth of a single transition in a given quantum dot determines the homogeneous broadening. The variations in size and shape among different quantum dots give rise to inhomogeneous broadening. (The equations in this and the following sections are written in the SI system of units.) The gain coefficient per unit time at frequency ω is related to the lineshape functions through the following expression [78]:

$$G(N,\omega) = 2\int D(E-E_0)\, g(\hbar\omega - E)\left|M\right|^2 (f_c(N,E) - f_v(N,E))dE, \qquad \text{(IV.23)}$$

where $g(E)$ is the homogeneous lineshape; the variations in transition energy resulting from the varying sizes of QDs are described by the function $D(E\text{-}E_0)$, where E_0 is the average transition energy; M is the matrix element for a transition, N is the carrier density, and f_c (f_v) is the Fermi factor for the conduction (valence) band.

For the undoped and quasi-neutral QD: $f_v = 1\text{-}f_c$ and also $N = 2f_cN_t$, where N_t is the number of QDs per unit volume.

Because of the large number of QDs in the active layer, $D(E)$ is assumed to be a Gaussian distribution function [78]:

$$D(E) = \frac{2N_t}{\gamma\sqrt{2\pi}} \exp\left(-\frac{1}{2}\left(\frac{E}{\gamma}\right)^2\right), \qquad \text{(IV.24)}$$

where γ gives a measure of inhomogeneous broadening resulting from the variations in QD sizes and is related to statistical variations of QD size.

For simplicity the homogeneous broadening is also assumed to be a Gaussian:

$$g(E) = \frac{\hbar}{\delta}\sqrt{\frac{\pi}{2}}\exp\left(-\frac{1}{2}\left(\frac{E}{\delta}\right)^2\right), \tag{IV.25}$$

where δ is a measure of the homogeneous broadening related to the finite width of the spectrum of a single QD.

The gain spectrum can be written as

$$G(N,\omega) = \frac{4|M|^2\hbar}{\sqrt{2\pi}\sqrt{\gamma^2+\delta^2}}(N-N_t)\exp\left(-\frac{(\hbar\omega-E_0)^2}{2(\gamma^2+\delta^2)}\right). \tag{IV.26}$$

This expression shows that transparency of the active layer occurs at the excitation level $N = N_t$. In the case of optical pumping the transparency should occur when the number of absorbed photons is equal to half the number of quantum dots in the active region. Saturation will occur when all QDs in the active layer are excited. For further calculations of the gain, an expression for $|M|^2$ from [79] can be used.

$$|M|^2 = \frac{E_0}{2\varepsilon_0\varepsilon_{QD}\hbar^2}|d|^2 \tag{IV.27}$$

where d is the component of the dipole matrix element in the direction of the electric field vector.

IV.4 Conclusions

This chapter discusses 3-D confinement in QDs and shows a comparison of the parameters of commonly used colloidal nanocrystals. Energy spectra for HgTe QDs were calculated and it was determined that the carriers in these QDs with radius below 2 nm are under the strong confinement regime. Two models for calculating energy spectra (infinite and finite spherical potential wells) were compared and it was found that

accounting for the finite well gives values for the energy separations of the levels that are closer to those experimentally measured from absorption spectra. The calculations showed a critical size for spherical HgTe QDs (radius less than 0.63 nm) under which there are no confined states. Considering the nanocrystals' deviation from the spherical shape should also give results that are better comparable with the experimental. This is a subject of research of another member of our group, Deepak Ganta.

Finally an expression for the gain in small spherical QDs was discussed.

CHAPTER V

WGM MICROLASER

V.1 Introduction

In the previous chapter we discussed the properties of semiconductor quantum dots and calculated some parameters of colloidal HgTe quantum dots. Because of the strong room-temperature infrared photoluminescence, due to the high confinement of carriers in this material, we found it suitable for a gain medium in the WGM microsphere resonator. The quantum dots are prepared in colloidal solution and coated with a layer of thioglycolic acid, which prevents further growth and clustering and also gives the particles a net negative surface charge.

Fused-silica microspheres have been studied extensively over the past several years as high-quality-factor (Q), low-mode-volume optical microresonators of wide-ranging applicability. Properties of the high-Q eigenmodes of a microsphere, called whispering-gallery modes, are discussed in Chapter II. Part of the field distribution of a WGM extends outside of the microsphere. This evanescent component enables interaction with material on the surface or in the surrounding medium. Recently, microspherical lasers employing several different techniques of introducing gain have been demonstrated [80-85]. We discuss a procedure for attaching the charged

semiconductor nanoparticles to the surface of a high quality optical microresonator. Having the gain medium right on the surface of a resonator allows for capturing a significant fraction of spontaneous emission, thus lowering the laser threshold and making this device promising for achieving thresholdless laser action [86]. Further improvement over previous WGM quantum-dot lasers that used free space coupling [37, 80, 87] is achieved by using tapered optical fibers for efficient coupling of the optical pump and the microlaser emission. The ultralow laser threshold was measured by following the increase of emission as the pump laser is scanned in frequency through a single WGM. We have measured the scattered pump losses simultaneously with the pump and the laser output for a better estimate of the actual absorbed power. Frequency selection of the laser emission by using coupled resonators is also discussed.

V.2 Spontaneous emission and coupling between emitters and cavity modes

Spontaneous emission is often viewed as an inherent property of matter, because it seems that an excited atom inevitably radiates. Nevertheless spontaneous emission is a consequence of atom-vacuum field coupling. When an electron makes a transition from an excited state to the ground state and a photon of energy $\hbar\omega = E_e - E_g$ is emitted, the electron is coupled to the vacuum state of the electromagnetic field. In free space there are an infinite number of vacuum states available. However if the density of these states is modified it is possible to enhance or inhibit the spontaneous emission. The coupling g between an atom and a single mode of the field is described by the Rabi frequency of the vacuum Ω [88] – the frequency at which the atom and a single mode of the field exchange energy:

$$g = \Omega/2 = d_{eg} E_{vac} / \hbar , \tag{V.1}$$

where d_{eg} is the matrix element of the electric dipole moment of the atom between the two levels (*e*-excited and *g*-ground) and E_{vac} is the rms vacuum electric-field amplitude in a mode of frequency ω,

$$E_{vac} = \sqrt{\frac{\hbar\omega}{2\varepsilon_0 V}} . \tag{V.2}$$

Here V is the size of an arbitrary quantization volume. However, in free space, the atom can radiate in any mode that satisfies energy and momentum conservation.

Using Fermi's golden rule the radiative transition rate of an atom can be written as [89]:

$$\Gamma = \frac{2\pi}{\hbar^2} |dE_{vac}|^2 \int \rho(\omega, \vec{r}) dV , \tag{V.3}$$

where d is the optical transition dipole matrix element, $\rho(\omega, \vec{r})$ is a position dependent density of photon states per unit volume and unit frequency interval, and $\vec{r}$ is the position of the emitting atom. The average density of states over the cavity volume (V_c) is defined as:

$$\rho_c(\omega) = \frac{1}{V_c} \int \rho(\omega, \vec{r}) dV . \tag{V.4}$$

In vacuum the density of states is a smooth function given by:

$$\rho_0 = \frac{\omega^2}{\pi^2 c^3} . \tag{V.5}$$

Equation (V.3) expresses the well-known and experimentally proven fact that the spontaneous emission rate of an atom can be reversibly changed by changing its optical environment. One way to achieve a control of spontaneous emission rate is to place an

emitter in a cavity of a size comparable with its emission wavelength. The cavity walls significantly modify the density of states available for the emitted photon. Modes are redistributed and concentrated at cavity resonance frequencies.

In the case of weak coupling, the coupling constant between the emitter and a cavity mode, g (half the vacuum Rabi frequency) satisfies $g << \Gamma_h$ (the homogeneous decay rate, $\Gamma_h = \Gamma_{nr} + \Gamma_{cav}$, is a sum of the nonradiative decay rate and the radiative decay rate in the cavity) and g << k (decay rate of the cavity photon). In the weak coupling case the spontaneous radiative decay is still irreversible but enhanced by a factor F called the Purcell factor:

$$\frac{\Gamma_{cav}}{\Gamma_0} = F \sim Q\frac{\lambda^3}{V}, \tag{V.6}$$

where Γ_0 is the free space radiative decay rate, V is mode volume in the cavity, and Q (here and throughout this chapter) is the cavity mode's Q_{total}. The Purcell factor is derived in detail in [89], where the position of the emitter inside the cavity is also taken into account.

The case $g >> \Gamma_h, k$ is referred to as the strong coupling regime, in which the emitter and the cavity can exchange energy coherently, so the spontaneous decay rate is reversible. A signature for this regime is splitting of the cavity modes by the vacuum Rabi splitting energy $\hbar\Omega$. The splitting has to be bigger than the broadening mechanisms (homogeneous broadening plus spectral diffusion or inhomogeneous broadening in the system) in order for this effect to be observed.

In relation to the emission of QDs in the microsphere resonator, the coupling constant g is proportional to the dipole moment of the quantum dot. QDs with large dipole moments are required for achieving strong coupling. Knowing the coupling

constant of our system is useful in determining the limits of the special quantum regimes that can be reached. These special regimes are usually referred to collectively as cavity quantum electrodynamics (CQED).

V.2.1 Calculation of the coupling constant for a silica microresonator and a HgTe QD

From the measured radiative lifetime of HgTe QDs $\tau_{rad} = 15$ ns [36] we can determine the dipole moment *d*. In the experiment described in [36] QDs were embedded in latex microspheres. Because the dipole radiates inside the quantum dot placed in a dielectric environment the decay rate relates to that of a dipole in vacuum as [90]:

$$\Gamma = \frac{1}{\tau_{rad}} = \frac{9\varepsilon_m^{5/2}}{\left(2\varepsilon_m + \varepsilon_{QD}\right)^2}\Gamma_0, \tag{V.7}$$

where ε_m is the dielectric constant of the embedding material, ε_{QD} is the dielectric constant of the QD semiconductor material, and Γ_0 is the radiative decay in vacuum (the same as Einstein's *A* coefficient):

$$\Gamma_0 = \frac{|d|^2 \omega^3}{3\pi\varepsilon_0 \hbar c^3}, \tag{V.8}$$

where ω is the emission frequency and *d* is the dipole moment. From (V.7) and (V.8) the dipole moment of HgTe QDs (in Debyes and in atomic units) is:

$$d = \frac{2\varepsilon_{m1} + \varepsilon_{QD}}{3\varepsilon_{m1}} \sqrt{\frac{1}{\tau_{rad}} \frac{3\varepsilon_0 \hbar \lambda^3}{8\pi^2 \varepsilon_{m1}^{1/2}}} = 73.6 \text{ D} = 28.47 \text{ a.u.}, \tag{V.9}$$

where the dielectric constant of the latex is $\varepsilon_{m1} = 2.52$, $\varepsilon_{QD} = 21$, and the emission wavelength is 1500 nm. With this large dipole moment HgTe QDs are very good candidates for experiments on special quantum regimes, such as thresholdless laser,

single emitter laser, and strong coupling. Table V.1 gives a comparison with other materials investigated for CQED experiments.

Emitter material	Nd^{3+} ions	Rb atoms	QDs: InAs	QDs: HgTe
Surrounding material	Embedded in silica	Near silica surface	Epitaxially grown in GaAs	Embedded in latex sphere
Dipole moment	~ 10^{-3} a.u. 0.002 D	~1 a.u. 2.5 D	15 a.u. 38.3 D	28 a.u. 73.6 D
Emission	1060 nm	780 nm	~1000 nm	~1500 nm

Table V.1. Comparison of dipole moments of materials investigated for CQED.

To go further in the calculations of the coupling constant we need to know the rms vacuum electric field in the case of a single QD emitting into a single WGM of a microresonator. The expression is similar to (V.2) with the difference that it takes into account that the emitter is inside a QD, includes the dielectric constant of the resonator material, and uses the mode volume V of a particular WGM:

$$E = \frac{3\varepsilon_m}{\left(2\varepsilon_m + \varepsilon_{QD}\right)}\sqrt{\frac{\hbar\omega}{2\varepsilon_0\varepsilon_m V}}\,. \tag{V.10}$$

The coupling constant can be found from (V.1) substituting the expressions (V.9) for the dipole moment and (V.10) for the rms vacuum electric field. Taking into account that the dipole moment was measured for HgTe QDs in latex, which is designated as $m1$, and the field is applied to QDs on the surface of a silica microsphere, which is designated as $m2$, we can write an expression for the coupling constant:

$$g = \frac{\lambda}{2\pi}\frac{\left(\varepsilon_{QD} + 2\varepsilon_{m1}\right)}{\left(\varepsilon_{QD} + 2\varepsilon_{m2}\right)}\frac{\varepsilon_{m2}}{\varepsilon_{m1}}\frac{1}{\sqrt{n_1}}\sqrt{\frac{3\pi c}{2n_2^2 V\tau_{rad}}}\,. \tag{V.11}$$

This expression assumes that a QD on a silica surface radiates as if it was embedded in silica. This assumption is justified in the next subsection. If $m1$ and $m2$ are identical the expression for the splitting energy (and consequently for the coupling constant) becomes the same as in [91]. The volume is calculated from (II.25) for the fundamental WGM of a spherical resonator of radius 300 μm.

Parameters for which the coupling constant is calculated:

$\lambda = 1.5\times10^{-6}$ m

$n_1 = \varepsilon_{m1}^{1/2} = 1.59$ - latex index of refraction

$n_2 = \varepsilon_{m2}^{1/2} = 1.45$ - silica index of refraction

$\tau_{rad} = 15$ ns radiative decay time

$\tau_2 = 7.5$ ns total decay time based on 50% quantum efficiency of HgTe QDs

$V_{1lm} = 12000\ \lambda^3$

The coupling constant is: $g = 1.71\times10^{8}$ s^{-1} or $\frac{g}{2\pi} = 27.2$ MHz .

The homogeneous decay rate Γ_h can be calculated from the total lifetime and the cavity decay rate k from the quality factor of the resonator at the emission wavelength as follows:

$$\frac{\Gamma_h}{2\pi} \approx \frac{1}{4\pi\tau_2} = 10.6 \text{ MHz and } \frac{k}{2\pi} = \frac{1}{2\pi\tau_{ph}^{e}} = 4 \text{ MHz},$$

$$\text{where } \tau_{ph}^{e} = \frac{\lambda_e Q_e}{2\pi c} = 39.8 \text{ ns}, \lambda_e = 1.5\times10^{-6} \text{ m and } Q_e \approx 5\times10^{7}.$$

Comparison between the coupling constant g and the decay rates Γ_h and k shows that strong coupling is possible in this system and that individual HgTe nanoparticles are good candidates for CQED experiments.

V.2.2. Spontaneous emission near planar interfaces

Modification of spontaneous emission can occur also when the emitter is placed at the interface between two media with different dielectric permittivities. This has been observed experimentally [92, 93] and is well studied in terms of classical electromagnetic theory [94-96] as well as quantum theory [97-99]. The findings are that the emission pattern differs significantly from the emission pattern of a dipole in an unbounded medium. Expressions for the dependence of the lifetime on the distance from the interface are derived from both the quantum theory and the classical electromagnetic theory (through the correspondence principle stating that the power radiated by spontaneous emission can be found from the power radiated by an electric dipole calculated by the classical theory by replacing the dipole moment with the transition matrix element). The classical theory [94] calculates the angular distribution of the dipole-radiated power. The field of the dipole is represented as a superposition of radiative field and near field. The interference of the plane waves (radiative field), emitted by the dipole, with their reflection from the interface determines the light distribution in medium 1 with the smaller refractive index, where the dipole is placed. Near field waves for which the wave number k is $k_1 < k \leq k_2$, where $k_1 = n_1 \omega/c$ and $k_2 = n_2 \omega/c$, are transmitted to the denser medium 2 as homogeneous plane waves with angles of refraction greater than the critical angle. In this way the near field carries power to the denser medium. Power contributed from the near field is significant only for distances (separation between the dipole and the denser medium) smaller than the wavelength.

The emission pattern of a dipole on a flat surface is highly nonsymmetrical with respect to the interface. It could be thought of as the directional probability distribution of an emitted photon, which shows that an emission event is most probable into the denser medium at an angle greater than the critical angle. Nevertheless, there is a finite probability of emission into free space. Calculations for the coupling of spontaneous emission from a single QD to a dielectric microsphere are done by Pelton and Yamamoto [100]. Coupling to a single fundamental (q = 1, m = l) TE mode is considered. The analysis is similar to that in Chapter II, but in this case the incident field is the radiation field emitted from the dot and it takes into account also the field scattered off the sphere. The fields are written as linear combinations of orthogonal spherical modes and the coefficients are related by the boundary conditions. Only modes of the same spherical symmetry can contribute to a particular WGM. It is found that the coefficients a_l, which determine the fields of a WGM (II.13) and (II.14), are related only to the coefficients of the incident mode a_l^{inc} as follows:

$$a_l = \frac{h_l'(k_0 a)\, j_l(k_0 a) - h_l(k_0 a)\, j_l'(k_0 a)}{n^2 j_l(k^{in} a) h_l'(k_0 a) - n j_l'(k^{in} a) h_l(k_0 a)} a_l^{inc}, \qquad \text{(V.12)}$$

where n is the refractive index of the dielectric sphere and it is assumed that the sphere is placed in air (or vacuum) so n^{ex} = 1, k_0 is the free space wave vector, and k^{in} is the wave vector of the interior material (fused silica in this case). This equation determines the spectral selection of the coupling. The coefficients of the incident mode are calculated as an overlap integral of the incident electric field and the appropriate spherical harmonic over the surface of the sphere:

$$a_l^{inc} = \frac{a^2}{l(l+1)\, j_l(k_0 a)} \int_0^{2\pi} \int_0^{\pi} \sin\theta d\theta d\phi E^{inc}(a,\theta,\phi) Y_{ll}(\theta,\phi), \qquad \text{(V.13)}$$

where E^{inc} is the dipole field modified by the presence of the dielectric boundary, calculated according to Ref. [94]. Equation (V.13) accounts for the spatial overlap between the incident field and the field of a WGM. The above procedure is used to calculate the capture fraction β, the fraction of spontaneous emission coupled to one particular mode of the cavity, as a function of sphere size and the separation between the dipole and the sphere. The conclusions are that larger spheres have more efficient capture of the radiation, which increases as the dipole is brought close to the surface. These conclusions strongly support the expectations for a large capture fraction of spontaneous emission into a lasing mode in our microlaser system. The large β factor allows for achieving lower laser threshold, as discussed in section V.4.

V.3 Laser rate equations

We assume a 3-level system for the QD-laser operation. The rate equations are written in a standard form.

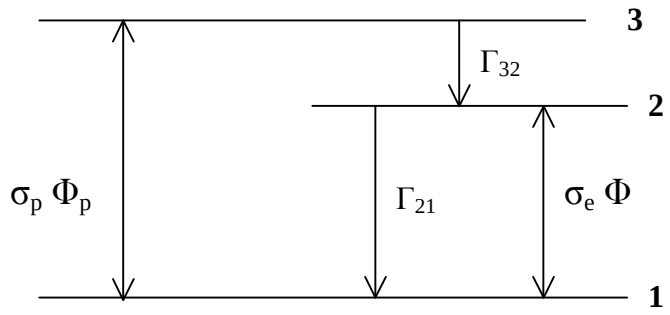

Figure V.1. Three-level laser transition diagram.

In the three-level diagram Φ_p and Φ are the pump and emission photon flux

inside the cavity, σ_p and σ_e are the pump absorption and laser emission cross-sections, and Γ_{ij} are the relaxation rates between energy levels. The population rate equations are as follows:

$$\begin{aligned}
\frac{dN_3}{dt} &= \sigma_p \Phi_p \left(N_1 - N_3\right) - \Gamma_{32} N_3 \\
\frac{dN_2}{dt} &= \Gamma_{32} N_3 - \Gamma_{21} N_2 - \sigma_e \Phi (N_2 - N_1) \\
\frac{dN_1}{dt} &= \Gamma_{21} N_2 + \sigma_e \Phi (N_2 - N_1) - \sigma_p \Phi_p \left(N_1 - N_3\right),
\end{aligned} \tag{V.14}$$

where N_i are excitons per unit volume in different energy levels i. We have assumed a fast 3-2 ($\Gamma_{32} \gg \Gamma_{21},\ \sigma_e \Phi$) transition so $N_3 \approx 0$. Under this assumption the laser gain and pump absorption coefficients for intensity are defined as:

$$\begin{aligned}
\gamma &= \sigma_e (N_2 - N_1) \\
\alpha_p &= \sigma_p N_1,
\end{aligned} \tag{V.15}$$

and the equations are solved for steady state.

Below threshold the stimulated emission term can be eliminated ($\Phi = 0$). The populations of levels 2 and 1 are:

$$\begin{aligned}
N_2 &= \frac{\sigma_p \Phi_p}{\sigma_p \Phi_p + \Gamma_{21}} N_t, \\
N_1 &= \frac{\Gamma_{21}}{\sigma_p \Phi_p + \Gamma_{21}} N_t, \\
\text{and } N_2 - N_1 &= \frac{\sigma_p \Phi_p - \Gamma_{21}}{\sigma_p \Phi_p + \Gamma_{21}} N_t.
\end{aligned} \tag{V.16}$$

Above threshold:

$$N_2 = \frac{\sigma_p \Phi_p + \sigma_e \Phi}{\sigma_p \Phi_p + \Gamma_{21} + 2\sigma_e \Phi} N_t,$$

$$N_1 = \frac{\Gamma_{21} + \sigma_e \Phi}{\sigma_p \Phi_p + \Gamma_{21} + 2\sigma_e \Phi} N_t, \qquad \text{(V.17)}$$

$$\text{and } N_2 - N_1 = \frac{\sigma_p \Phi_p - \Gamma_{21}}{\sigma_p \Phi_p + \Gamma_{21} + 2\sigma_e \Phi} N_t,$$

where $N_t = N_1 + N_2$ is the total density of QDs participating in lasing. What is interesting to notice at this point is that the population density of the ground level increases above threshold compared with its value below threshold, as long as $\sigma_p \Phi_p > \Gamma_{21}$, which is the condition for population inversion, satisfied above threshold. Increased population density of the ground level also means that the pump absorption above threshold is increased.

The field gain per unit time is then defined as:

$$G = \frac{\gamma}{2} \frac{c}{n_{eff}} = \frac{c\sigma_e}{2n_{eff}} (2N_2 - N_t). \qquad \text{(V.18)}$$

In the case of QD laser medium the first term ($2N_2$) represents the carrier density N and the second term N_t is the QD density, thus $G \propto N - N_t$ as derived in section IV.3.

V.4 Laser threshold

The condition for laser threshold can be expressed by setting the gain equal to the cavity loss. On the basis of coupled-mode formalism for a fiber coupled resonator with the addition of gain and loss terms it is shown [101] that at threshold

$$G = \frac{1}{2\tau_{ph}^e} = \frac{k}{2}, \qquad \text{(V.19)}$$

where G is the intracavity field gain per unit time for a particular cavity mode, and τ_{ph}^{e} is the cavity photon lifetime at the laser emission wavelength. τ_{ph}^{e} is proportional to the total quality factor of the cavity mode at the emission wavelength. For the gain we use expression (IV.26) from the discussion in Chapter IV. Thus the intracavity field gain coefficient per unit time at the frequency of emission ν_e is:

$$G = \frac{2\nu_e |d|^2 (N - N_t)}{\sqrt{2\pi}\varepsilon_0 \varepsilon_{QD} \hbar \sqrt{\Delta\nu_h^2 + \Delta\nu_{in}^2}}, \tag{V.20}$$

where $N = 2N_2$ is the carrier density, $\Delta\nu_h$ is the homogeneous linewidth, and $\Delta\nu_{in}$ is the inhomogeneous linewidth of the laser transition. (Both lineshapes are assumed to be Gaussian.) We can express the carrier density at threshold as a function of the cavity and gain medium parameters as:

$$N_{th} = \frac{\sqrt{2\pi}}{4} \frac{\sqrt{\Delta\nu_h^2 + \Delta\nu_{in}^2}}{\nu_e} \frac{\varepsilon_0 \varepsilon_{QD} \hbar}{|d|^2 \tau_{ph}^{e}} + N_t. \tag{V.21}$$

For a three-level system the minimum power necessary to achieve laser oscillation is approximately [102]:

$$P_{th} \approx \frac{1}{2} \frac{h\nu_p}{\tau_2} N_{th} V_p \approx \frac{1}{2} \frac{h\nu_p}{\tau_2} N_t V_p, \tag{V.22}$$

considering a 100% pump efficiency (each photon produces 2 carriers) and a large number of QDs participating in the lasing. Here V_p is the cavity pump mode volume, ν_p is the pump frequency, and τ_2 is the total decay time of level 2.

The following data have been used for calculation of the carrier density and the threshold power:

$\lambda_p = 0.83\times10^{-6}$ m pump wavelength

$\lambda_e = 1.5\times10^{-6}$ m emission wavelength

$\triangle\nu_h = \frac{1}{2\pi\tau_2} = 21$ MHz homogeneous linewidth

$\triangle\nu_{in} \approx 10^{12}$ Hz inhomogeneous linewidth

$d = 73\ \mathrm{D} = 2.42\times10^{-28}\ \mathrm{C}\cdot\mathrm{m}$

$\varepsilon_{QD} = 21$ HgTe permittivity

$n = 1.45$ fused silica index of refraction

$\tau_{rad} = 15$ ns

$\tau_2 = 7.5$ ns total decay time of level 2, based on 50% quantum efficiency of HgTe QDs

$Q_e = 5\times10^7$ at emission wavelength and $Q_p = 5\times10^6$ at pump wavelength

$\tau_{ph}^e = \frac{\lambda_e Q_e}{2\pi c} = 39.8$ ns

$V_p = V_{1lm} = 12000\ \lambda^3$

$a = 250$ μm microsphere radius

For the threshold carrier density we get $N_{th} = (2.8\times10^{16} + N_t)\ \mathrm{m}^{-3}$, which is dependent on the number of QDs in the mode volume. The two terms in N_{th} would be comparable when the number of QDs in the mode volume is on the order of 10^2. Assuming 10^5 QDs in the pump mode (which would correspond to 0.1% coverage and 10% of the QDs strongly absorbing the pump), the threshold power is $P_{th} \approx 1.6\ \mu\mathrm{W}$. To find how this threshold power relates to the power lost from the pump WGM we have to take into account that only a fraction of the power lost is absorbed (typically $\eta_{abs} = 0.2$, as discussed in section V.7.3), and that the input power relates to the intracavity power as in (III.9) and for a critically coupled mode through (III.10). Also, the intensity at the surface is smaller than the average intensity by a factor approximately equal to the evanescent fraction plotted in

Fig. III.2, $\eta_{ev.fr} = 0.02$. It is possible to calculate the threshold power for an undercoupled or an overcoupled mode if we know the coupling regime ($x > 1$ or $x < 1$), the dip depth M_0, and the total Q factor. All of these factors can be expressed in:

$$\left(P_{in}\right)_{th} = \frac{4}{\eta_{abs}\eta_{ev.fr}} \frac{\pi^2 n_{eff} a}{\lambda_p Q_p (1+x) M_0} P_{th}. \tag{1.23}$$

For the case of a critically coupled mode the power is:

$$\left(P_{in}\right)_{th}^{c} = \frac{2}{\eta_{abs}\eta_{ev.fr}} \frac{\pi^2 n_{eff} a}{\lambda_p Q_p^c} P_{th}, \tag{V.24}$$

where is the quality factor of the same pump mode at critical coupling and the actual total input power lost needed to reach the threshold is $\left(P_{in}\right)_{th}^{c} = 688$ nW. For an undercoupled mode of M_0 = 88%, similar to one experimentally measured (shown later in Fig. V.13), the total input power lost at threshold is $\left(P_{in}\right)_{th} = 1.04\ \mu$W.

Although this is a reasonable approximation for the expected threshold power, a quantum analysis of the rate equations, accounting for the large capture fraction of spontaneous emission to the lasing mode, further lowers the expected threshold and reveals different laser operation close to the threshold point. A quantum theory of near threshold behavior of a similar laser system is given in [86]. The model describes an active medium of two-level atoms resonant with a single cavity mode. The atoms are uniformly coupled to the field with a coupling constant *g*. The model does not account for inhomogeneous broadening and mode competition. However for our QD-coated microsphere laser this is acceptable because the homogeneous width of the transition in HgTe QDs (~ 21 MHz) is smaller than the cavity mode spacing (>1 GHz spacing between adjacent polar modes, measured experimentally). In this case a given class of QDs (same

size and shape) in the inhomogeneously broadened spectrum can emit to only one mode of the cavity that is resonant with their transition frequency. This way there will be no mode competition in such a system. Further, the model derives an exact relation between the population inversion and the intensity from Heisenberg-Langevin equations written in the interaction picture. The analytical treatment is based on the assumption that the population inversion is large enough so that its fluctuations can be neglected. This model gives an analytical expression for the relation between the emission intensity and the pump rate, which is:

$$I = \frac{1}{2}(r-1-c) + \frac{1}{2}\sqrt{(r-1-c)^2 + 4cr\left(1+\frac{\Gamma_2}{\Gamma_1}\right)} \tag{V.25}$$

where I is the emission intensity normalized to the saturation intensity, r is the pump rate normalized to the threshold rate, Γ_2 and Γ_1 are the relaxation rates of the two levels (Γ_2 does not include spontaneous emission into the lasing mode), and c is:

$$c = \frac{2g^2}{\Gamma_2(\Gamma_h + k/2)}, \tag{V.26}$$

where $\frac{2g^2}{\Gamma_h + k/2}$ is the rate of spontaneous emission into the lasing mode, Γ_h is the homogeneous decay rate, and k is the decay rate of the cavity photon. The meaning of c is simply the ratio of spontaneous emission into the lasing mode to the rate of all other upper-level decay channels. The relation of c to the previously discussed capture fraction β can be approximated as:

$$\beta = \frac{c}{c + \Gamma_2^{sp}/\Gamma_2}, \tag{V.27}$$

where Γ_2^{sp} is the total radiative decay rate. When spontaneous emission accounts for half

the decay of the upper level then $\beta = c/(1/2 + c)$ and the thresholdless regime is realized when $\beta \to 1$. This model has been used to analyze the behavior of our laser system near threshold.

V.5 Microsphere fabrication and coating with semiconductor nanoparticles

V.5.1 Fabrication of high quality factor microsphere resonators

When ultra-high *Q* factors are necessary, microsphere cavity losses must be minimized. Fused silica optical fibers are designed to have extremely low loss in the near infrared region of the spectrum. The low OH concentration in this material reduces the absorption losses. This makes optical fibers an ideal material for microsphere fabrication. The fiber is stripped and carefully cleaned with methanol and electrowash (commercially available spray for cleaning optical fibers). We melt the end of an optical fiber with a hydrogen-oxygen torch. The end bends in the direction of flow and the surface tension pulls the molten silica into a sphere with an extremely smooth surface. If the gas flow is kept slow the formation of the sphere is slow and allows for the impurities left on the surface to burn out. Keeping the optical fiber in the flame for 1 to 2 minutes results in quality factors greater than 10^8. For fabricating microspheres of diameter less than 300 μm the end of a 125 μm fiber is first tapered to a smaller diameter. The gas flow has to be adjusted for different sphere sizes. Our microspheres typically range in diameter from 100-1000 μm. Bigger microspheres have lower eccentricities, which brings them closer to the perfect sphere shape. Surface roughness was measured by an atomic force microscope (AFM). A typical

scan is shown in Fig. V.2. Microspheres of $Q > 10^8$ had surface roughness less than 1 nm.

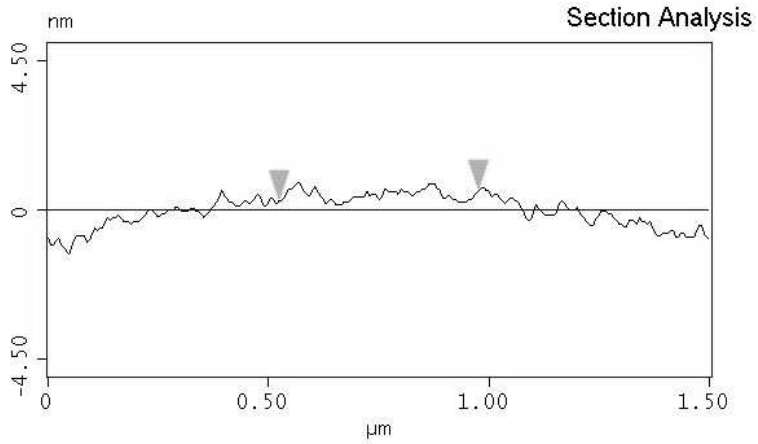

Figure V.2. Section analysis of an AFM image of a surface of fused silica microsphere of diameter 600 µm.

Losses due to surface scattering (the most significant source of loss for coated as well as bare spheres) are calculated for a microsphere with a radius 300 µm and average height of the roughness h = 2 nm and average width B = 20 nm, according to (II.31). The Q factor resulting from scattering losses predicted by this calculation is $\sim 4\times10^8$ for $\lambda = 830$ nm, consistent with the measured Q factors.

V.5.2 Coating of a fused silica microphere resonator with semiconductor nanoparticles

Our coating method simplifies control of the surface density of quantum dots deposited on the microsphere. We used D_2O as a solvent instead of water, in order to reduce the absorption of the surface coating at the long emission wavelengths. The region of strong absorption in the near IR for D_2O is shifted, compared with H_2O, towards longer wavelengths (Fig. V.3). The measurement was done with a Varian Cary 5.

Deionized water or high purity D_2O samples were placed in a standard plastic cuvette and the transmission was compared to that through an empty cuvette in the reference channel. The experiments show that use of D_2O as a solvent is necessary to achieve lasing from HgTe nanoparticles since it was never achieved with water as a solvent.

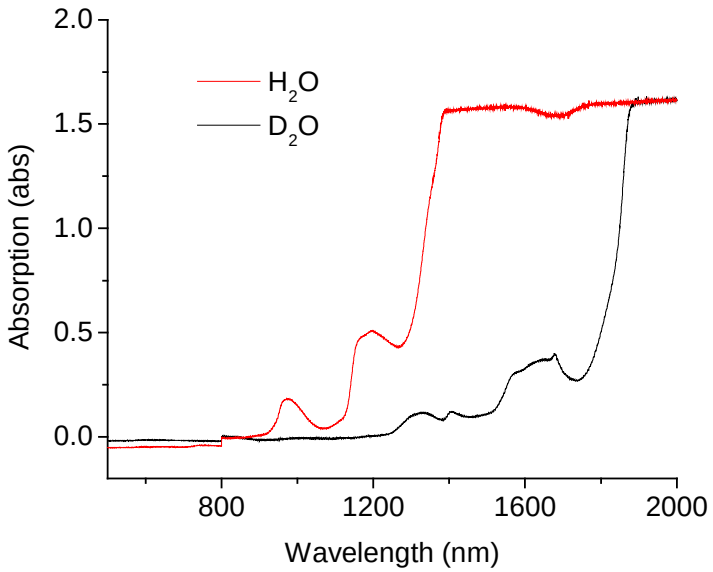

Figure V.3. Absorption spectra of H_2O and D_2O. Clearly D_2O shows less absorption between 1300 nm and 1800 nm, where the peak of HgTe luminescence is expected.

A bilayer coating method was used to functionalize the surface of the silica microsphere, in a manner similar to the layer-by-layer method previously used for preparation of both multilayers [103] and (sub)monolayers [104] of semiconductor nanoparticles. First the microsphere was dipped in a 0.5% D_2O solution of poly(dimethyldiallylammonium) chloride (PDDA) for 30 minutes to obtain a positively charged layer of polyelectrolyte on the surface. It is washed with D_2O for 1 minute to wash away the Cl ions and leave the surface slightly positively charged. Examining the

surface with an AFM shows that the PDDA layer does not add any significant change to the surface roughness of the microsphere. Next the microsphere was dipped in a D_2O solution of negatively charged HgTe nanoparticles long enough to produce a fraction of a monolayer between 0.1% and 1%, as determined by AFM of a coated microsphere. The typical molar concentration of HgTe nanoparticles in D_2O solution was varied from 10^{-6} to 10^{-7} and the dipping time from 5 to 30 sec. The negative charge of the HgTe nanoparticles originates from the organic stabilizer coating their surfaces, which was thioglycolic acid. The organic coating has the function of limiting the growth process. The microsphere is washed again in D_2O for 1 min to remove particles that are not attracted to the surface. Further washing with D_2O helps also to exchange water adsorbed on the surface. As can be seen from the AFM image in Fig. V.4, the polyelectrolyte macromolecules adjust their coverage on the silica surface to form transparent shells (collars) around the HgTe nanoparticles, reducing photoinduced corrosion [104] and improving their adherence to the microsphere. Figure V.5 shows another example of a coated microsphere surface. In this case the nanoparticle solution was ~10^{-6} M and although the microsphere was kept in it for a shorter time the resultant surface coverage is denser. This figure also shows the typical size dispersion when using the nanoparticle solution as prepared without further size selection. The size dispersion of different batches of nanoparticles ranges from 5% to more than 30%. It slowly deteriorates as HgTe particles have the tendency to ripen (grow in size) in time despite their organic coating.

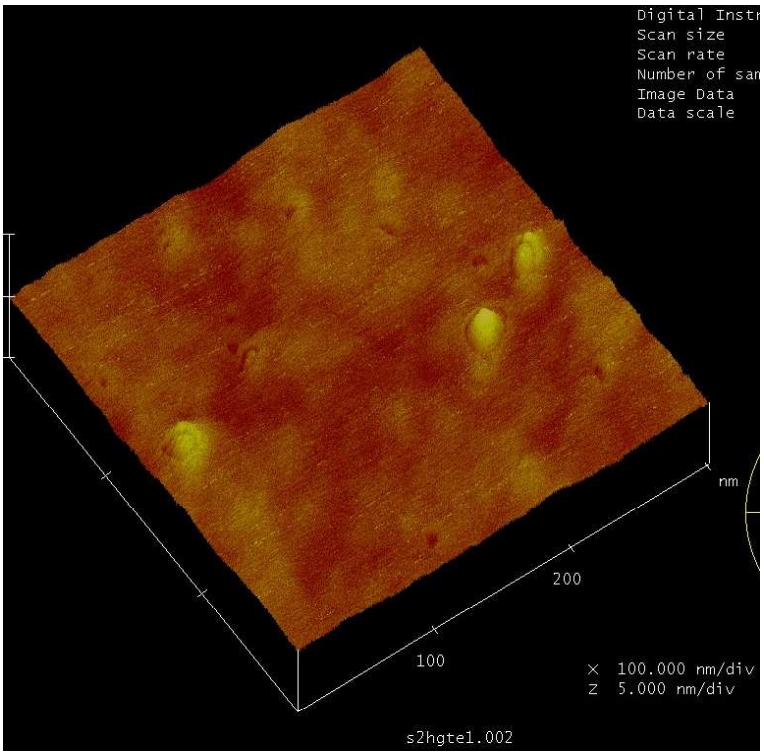

Figure V.4. Surface of a 450 μm diameter sphere coated with a bilayer of PDDA and HgTe nanoparticles. Scan is 300×300 nm and the vertical scale is 5 nm/div. The diameter of the particles is 3 to 4 nm. The concentration of the nanoparticle solution was ~ 10^{-7} M. The microsphere was dipped for 10 sec.

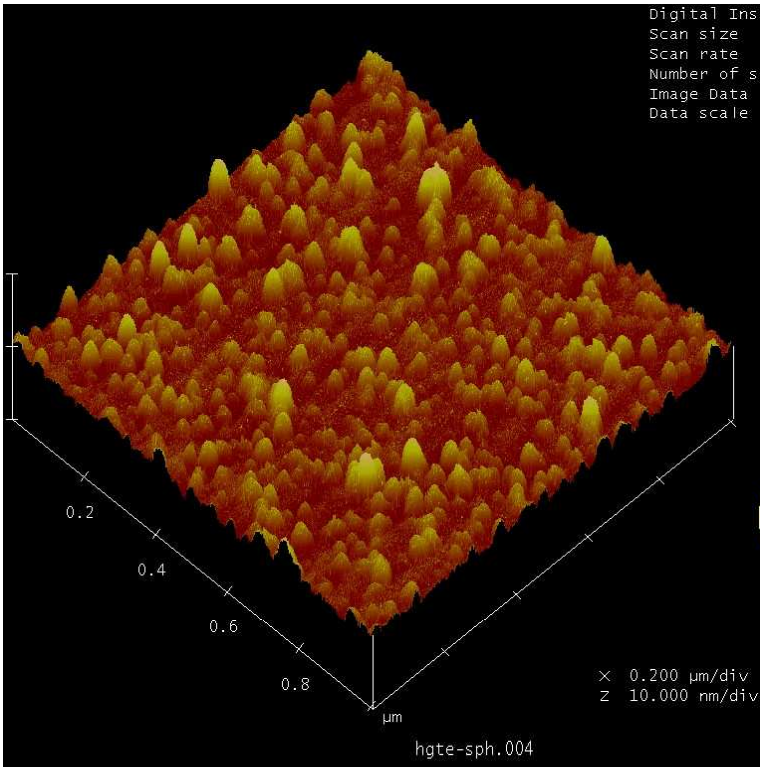

Figure V.5. Surface of a 650 µm diameter sphere coated with a bilayer of PDDA and HgTe nanoparticles. The concentration of the nanoparticle solution was ~ 10^{-6} M. The microsphere was dipped for 5 sec. The scan is 1×1 µm and the vertical scale is 10 nm/div.

The section analysis in Fig. V.6 gives an idea of the size dispersion in the sample. The highest object selected on the section analysis appears to be two particles stacked together vertically.

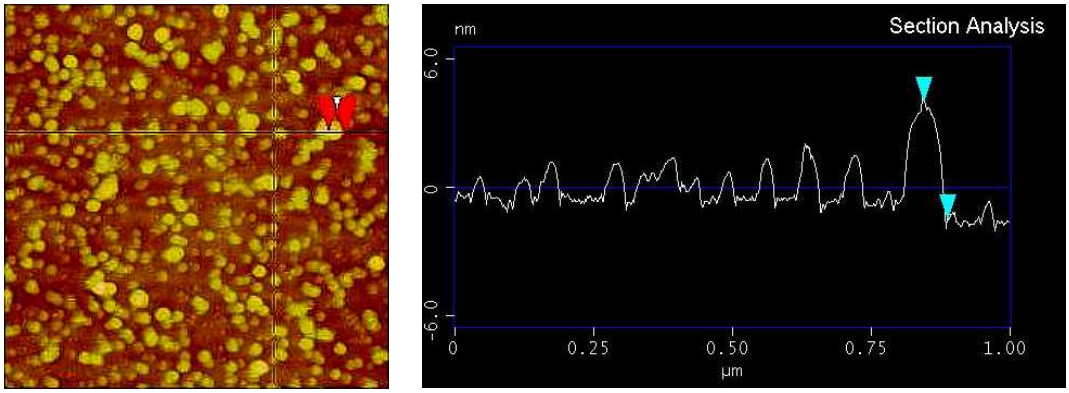

Figure V.6. AFM image and section analysis of a bilayer of PDDA and HgTe NPs coated on a surface of a microsphere.

To improve the size uniformity of our samples we have used capillary electrophoresis. A concentrated solution of HgTe NPs is run through a coated 50 cm long, 50 µm diameter, open tube capillary, which has different potentials at the ends. It was prepared as follows: first rinsed with 1.0 M sodium hydroxide for 15min, then flushed with 0.1 M HCl and rinsed with water for 15 min, and finally rinsed with running buffer. The separation method employs a single buffer (20 mM phosphate buffer pH 7) in the solution. The particles have different velocities based on differences in mass-to-charge ratios. Both mass and charge are functions of particle size. By collecting particles at different time intervals it is possible to select groups with more uniform size distributions. This method has improved the size dispersion on the coated surfaces. The difference is evident comparing Fig. V.4 with Fig. V.5. The coating shown in Fig. V.4

was made with an NP solution processed with capillary electrophoresis and separated into two fractions with respect to the particle size. The fraction with the smaller average size particles was used for coating. The method is effective when low concentration samples (10^{-8} M – 10^{-7} M) are needed, but it is extremely time consuming and ineffective for more concentrated samples.

V.6 Experimental setup and emission measurements

V.6.1 Experimental setup, excitation, and emission outcoupling

The experimental setup is shown in Fig. V.7. As a pump source we use a tunable cw Ti:sapphire laser. The laser is stabilized and has a very narrow emission line of width 40 kHz. The laser mirror set currently in use allows lasing in the wavelength interval between 770 nm and 860 nm, tunable by rotating the birefringent filter inside the cavity. The intracavity etalon and the electronics unit allow for fine tuning and scanning the laser frequency over a range of up to 40 GHz. The optical isolator after the pump laser output is a Faraday rotator that prevents backscattered light from entering the laser. The pump is coupled into a WGM of the microsphere via a biconical tapered fiber. The fiber diameter is optimized [105] for efficient coupling of the pump wavelength. That fiber continues to detector P1, a Si photodiode (Newport 818-SL). The pump WGM resonances are observed as the pump frequency is scanned. The lock-in amplifier is used when pump and emission measurements are made simultaneously. A short-pass filter removes any microlaser emission coupled out into this fiber.

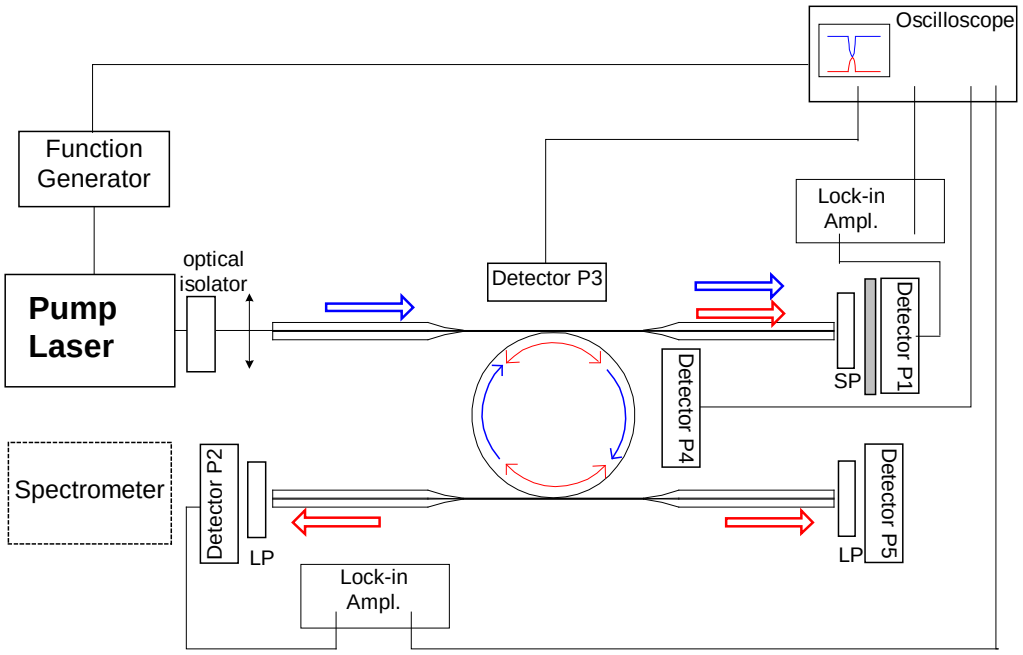

Figure V.7. Experimental setup. Light from a frequency-scanned cw Ti:sapphire laser (blue) is launched into a bitapered fiber to excite WGMs of the microsphere and pump the quantum dots, which produce microlaser emission (red). LP and SP denote filters that pass long (> 900 nm) and short (< 900 nm) wavelengths respectively. Detector P2 and the filter can be exchanged with a spectrometer for measuring the emission spectrum.

A second tapered fiber, optimized for the microlaser emission wavelength, also couples light out of the microsphere; any pump light is filtered out by a long-pass filter and the microlaser emission goes to detector P2, a Ge photodiode (Newport 818-IR). The signal from detector P2 is amplified by a second lock-in and an emission peak is displayed on the oscilloscope. Detector P2 in Fig. V.7 can be replaced with a scanning monochromator (SpectraPro-300) to determine the microlaser emission spectrum. The scattering losses of the pump are measured with detectors P3 and P4, Si photodiodes (Newport 818-ST). Detector P4 is actually above the plane of the figure. Detector P2 and the long pass (LP) filter in front of it were replaced by another detector (Newport 818-SL) to verify that outcoupling of the pump through the second fiber made only a small contribution (about 1%) to the total pump loss. A microscope sits above the plane of the figure, and looks down on a pole of the sphere. It is used for visual alignment of the couplers. In addition, the light scattered from the periphery of the sphere could be captured through the microscope with a detector. This is either a Si detector for measuring scattered pump light or a Ge detector (with long-pass filter) for observing scattered microlaser emission. The two tapered fibers are attached to holders as shown in Fig. III.6. The holders are mounted on 3D stages (Newport 561) with angular alignment (Newport 561 TILT). The microsphere is mounted on a chuck, attached to a lens holder, which allows for vertical and horizontal adjustments. A view of the microsphere and the fibers through the microscope is shown in Fig. V.8.

The setup is kept in a Plexiglas box to eliminate air currents and reduce dust contamination.

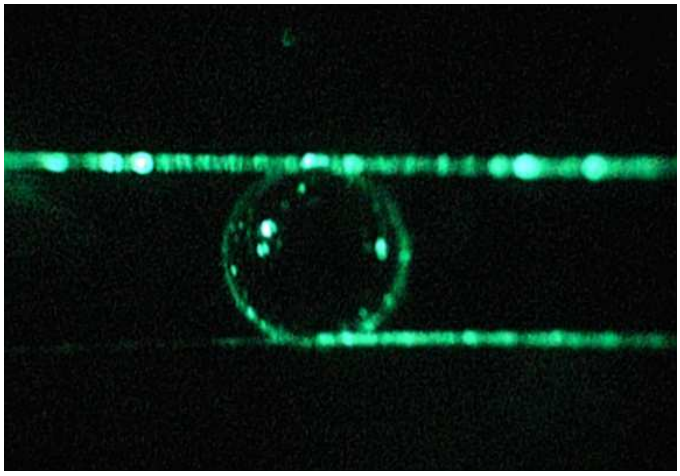

Figure V.8. The IR viewer image of the pump radiation at 834 nm.

V.6.2 Spectral measurements

In most of our experiments we chose to scan the laser slowly over a small frequency range (1-2 GHz at a 1 Hz repetition rate), rather than trying to stay on a particular pump WGM. This scan rate is slow enough that we can say with confidence that continuous (cw) laser emission was observed; the time scale for changes in the emission due to pump scanning is far longer than the cavity or material lifetimes. Higher pump power heats the microsphere and results in shifting the WGMs in one direction. When the pump laser is scanning in that direction the modes are broadened and when the scan is in the opposite direction the modes appear sharper. This effect is referred to as thermal bistability. To avoid it we kept the pump power incident on the microsphere lower than a few mW. Observing continuous wave laser emission was done as we tune the laser frequency to a WGM and stop the scan at this point. For measuring the emission

spectrum we use the experimental setup of Fig. V.7 with a spectrometer (SpectraPro-300) replacing the detector P2.

Spectral measurements typically suggest multimode laser operation over a narrow portion of the photoluminescence spectrum. An example is given in Fig. V.9. The photoluminescence is measured from a solution of the same batch of nanoparticles, but in a separate experiment. The limited spectrometer resolution (0.1 nm) does not allow us to distinguish individual lasing WGMs. The pump laser was scanned in frequency while the emission spectrum was measured. Different spikes in the emission are actually different pump scans through a mode.

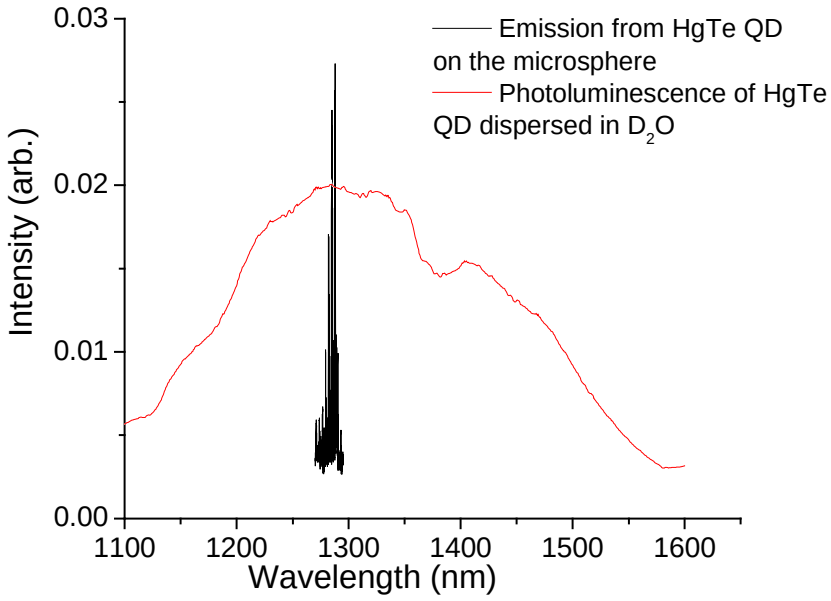

Figure V.9. Broad photoluminescence and narrow laser emission spectra from the same batch of HgTe nanoparticles prepared in D_2O solution.

Continuous emission has been verified by stopping the pump laser scan in the middle of a pump WGM while acquiring a microlaser emission spectrum with the spectrometer, as shown in Fig. V.10.

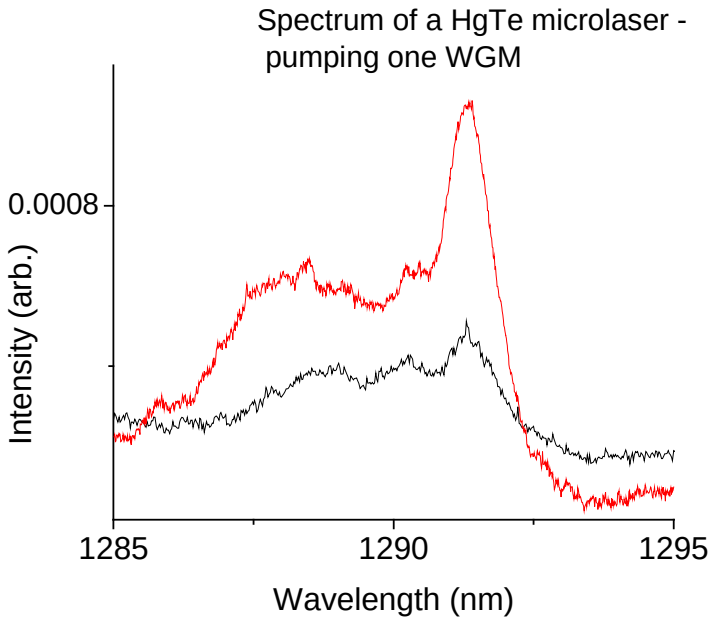

Figure V.10. The frequency of the pump laser is kept at the resonant frequency of a particular WGM. Increasing the pump power (black trace to red trace) produces the takeoff of the lasing modes.

The observed microlaser emission wavelengths, using different batches of nanoparticles having different semiconductor cores but similar organic coatings, are in the 1240-1780 nm range. Fig. V.11 shows an example of emission lines for several different batches of nanoparticles. Longer wavelengths are produced by HgTe and shorter by HgCdTe. The blue shift of the lasing wavelength for HgCdTe is consistent with the increase of absolute energy of the conduction band when Cd atoms are added to the crystal lattice, thereby widening the bandgap [27, 33].

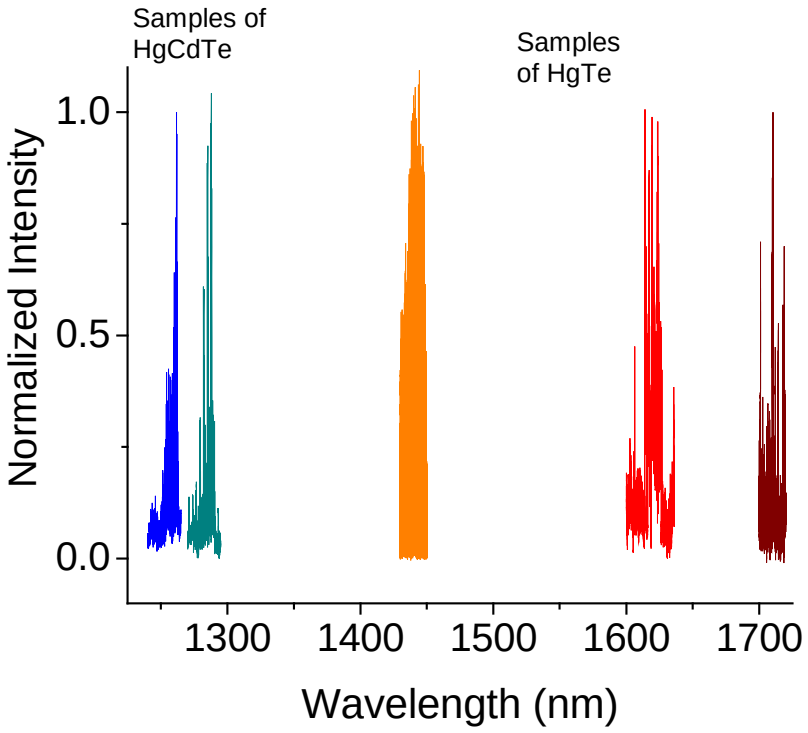

Figure V.11. Emission spectra of different samples of HgCdTe and HgTe NPs, coated on different microspheres. Intensity is normalized.

The first sample from the shorter wavelength side is $Hg_{0.8}Cd_{0.2}Te$ with average size 3nm in diameter. In the second some content of Cd, less than 10%, was traced by energy dispersive X-ray analysis (EDX) – average size 3 nm. These two samples were treated with capillary electrophoresis for narrowing the size dispersion as described in section V.5.2. The last three samples are HgTe NPs of different average size (orange – 3 nm, red – 5 nm, and brown – 6 nm). The absolute values of intensities are significantly lower for the wavelengths above 1600 nm, because of the strong water absorption in this spectral region. For the first three samples the emission peaks, from the NPs coated on high *Q*-factor microresonators, coincide with the peaks of broad luminescence spectra, in

a manner similar to that shown in Fig. V.9. For the last two samples luminescence spectra were not available.

V.7. Input-output characteristics and threshold measurements

V.7.1 Input-output measurements

For measuring the increase of output power as a function of the laser pump power we used the setup shown in Fig. V.7. The pump laser was scanned 1GHz per second. Snapshots of pump dips and emission peaks were taken simultaneously from the oscilloscope display of detector P1 (measuring the pump throughput) and P2 (measuring the laser output) readings. One pump WGM was chosen and followed through the snapshots, simultaneously with the corresponding emission peak, as the pump off-resonance throughput power was increased from about 5 μW to higher power. Three examples of microlaser output power are shown in Fig. V.12 as a function of total pump power – the portion of the incident power that is lost, absorbed as well as scattered from the nanoparticles on the surface of the microsphere. Each experimental point has a horizontal coordinate corresponding to the minimum of the resonance pump dip and vertical coordinate corresponding to the maximum of the emission peak. The detectors' responsivities for different wavelengths were taken into account.

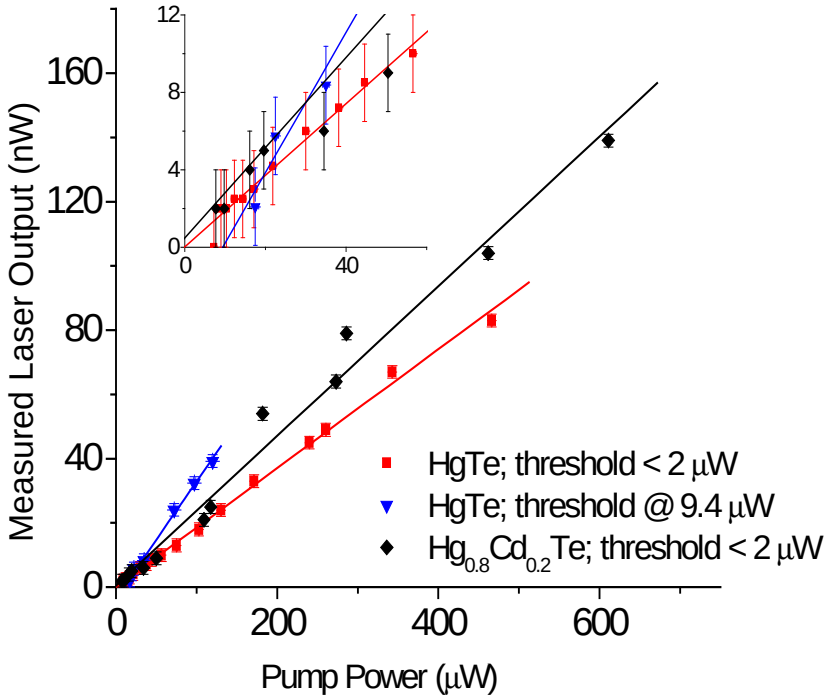

Figure V.12. Measured microlaser output (one fiber, one direction) versus total pump power. The inset shows the region near the origin. The lines are linear fits to the data.

In Fig. V.12 two of the microsphere resonators are coated with HgTe NPs. One had a diameter of 650 μm, pump Q of 2×10^6, and lasing Q of about 10^7 (around 1620 nm, estimated from measurements made on the microsphere before coating); a linear fit to the data gives a threshold total pump power of P_{th} = 9.41 ± 2.35 μW. The other had a diameter of 950 μm, pump Q of 2×10^7, and lasing Q of about 10^8 (around 1670 nm); the linear fit gives P_{th} = -0.06 ± 2.18 μW. The third microsphere was coated with $Hg_{0.8}Cd_{0.2}Te$. It had a diameter of 600 μm, pump Q of 1×10^7, and lasing Q of about 6×10^7 (around 1250 nm); the linear fit gives P_{th} = -5.62 ± 4.85 μW. The thresholds and their uncertainties are overestimated, by about a factor of five, because the total pump

power includes losses due to scattering and to outcoupling via the second fiber. The measured slope efficiencies of 2×10^{-4} – 4×10^{-4} are likewise underestimated by about an order of magnitude. The overestimate of pump power also contributes to this, as do measurement of just a fraction of the output power (one fiber, one direction) and water absorption of the microlaser emission. (With time, the D_2O in the coating is replaced by water; rinsing with D_2O after several days of use can increase the microlaser power by more than a factor of two.)

The extremely low laser threshold cannot be measured precisely with the presented technique. In order to improve precision of the input-output measurements and get a good estimate of the actual absorbed pump power, we developed a new technique described in the next subsection.

V.7.2 Input-output measurements in a single pump WGM

In this method of data collection, the emission is correlated with the dip in the pump signal instead of varying the pump power and comparing peaks. As the pump scans across a WGM dip, the intracavity intensity varies; emission occurs when threshold is crossed. The off-resonance power for these measurements was kept low (less than 100 μW) to avoid distortions of the pump mode shape because of thermal bistability. The experimental setup is as shown in Fig. V.7. The precision is enhanced by lock-in amplification. An important point in this measurement is to have the two signals, pump and emission, amplified equally, which ensures the same time delay in the compared signals. To have the two signals measured at the same scale we have used a neutral-density (ND) filter before detector P1 to attenuate the pump throughput signal. Another

consecutive measurement of the same throughput dip without the ND filter gives the scaling factor to determine the true total pump power. This improved method of data collection allows acquiring many data points and thus improving the error analysis. A typical threshold curve determined using this technique is shown in Fig. V.13.

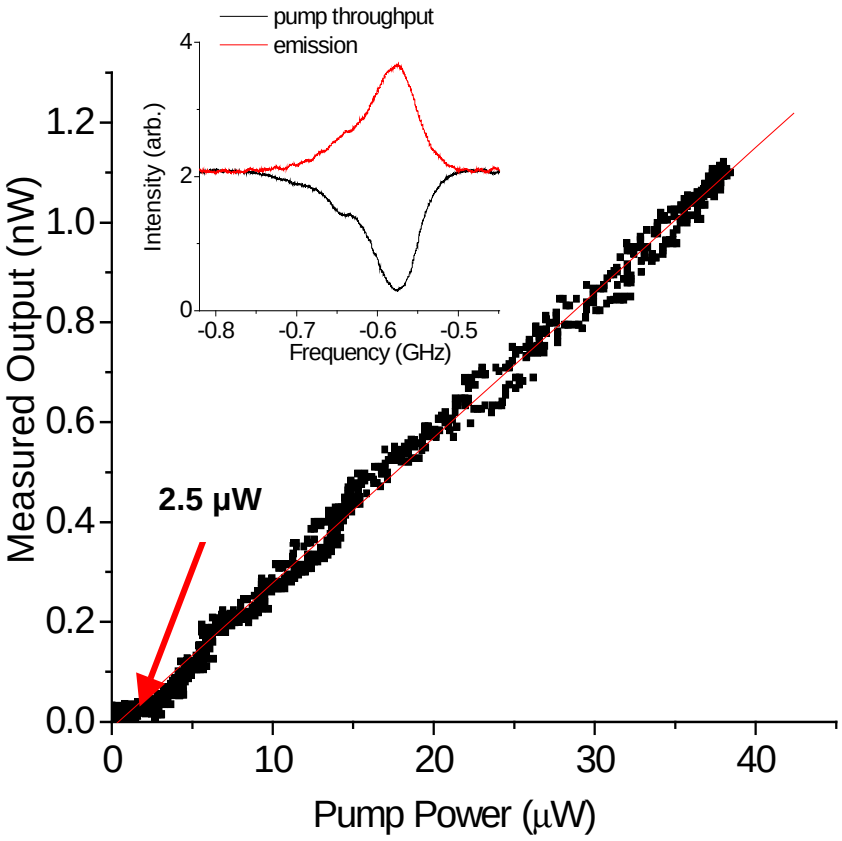

Figure V.13. An example of input – output characteristic of the laser emission.

The threshold measurement of Fig. V.13 shows a threshold of the total pump power at 2.5 μW. As was said earlier, the pump power is overestimated mainly because it includes the scattered power loss, which does not contribute to excitation of the NPs. To find the actual pump power absorbed by the active medium we have performed a simultaneous measurement of the scattered pump signal along with the pump throughput and laser emission, described in the next subchapter.

V.7.3 Measuring the scattered losses and estimating the absorbed pump power

Scattered pump light was measured with detectors P3 and P4 from Fig. V.7. Detector P3 stays on one side of an imaginary cube (Fig. V.14) surrounding the microsphere and P4 stays on the top (or bottom).

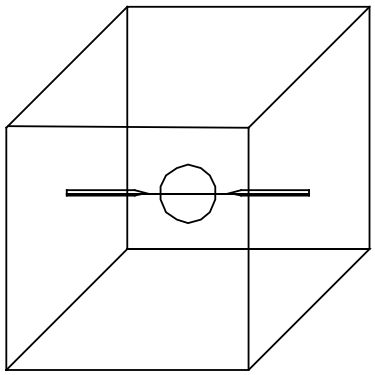

Figure V.14. The microsphere is placed in an imaginary cube for measurement of the integrated scattering losses.

A side surface of the cube is 1 cm^2, corresponding to the surface of the active area of each of the detectors. We assume equal scattering losses for each of the four sides and equal losses for the top and bottom (which are different from the side losses). It was experimentally verified that the top and bottom sides have very similar scattering losses and also that the losses measured on the sides parallel to the fiber are similar. The readings from all detectors, P1 (pump throughput power in black in Fig. V.15), P2 (laser emission in red), P3, and P4 (scattered losses) were taken simultaneously. The total scattered power was estimated to be $4\times P_3 + 2\times P_4$. A plot of this integrated scattered power is shown in Fig. V.15 in blue. The scattered pump power is different for each pump WGM. For the sphere whose WGM spectrum is shown in Fig. V.15, it ranges

between 80% and 64% of the total pump power. The difference between the total pump power and the sum of the scattered pump power plus the pump power outcoupled through the second fiber, mentioned earlier, gives an estimate of the actual absorbed pump power.

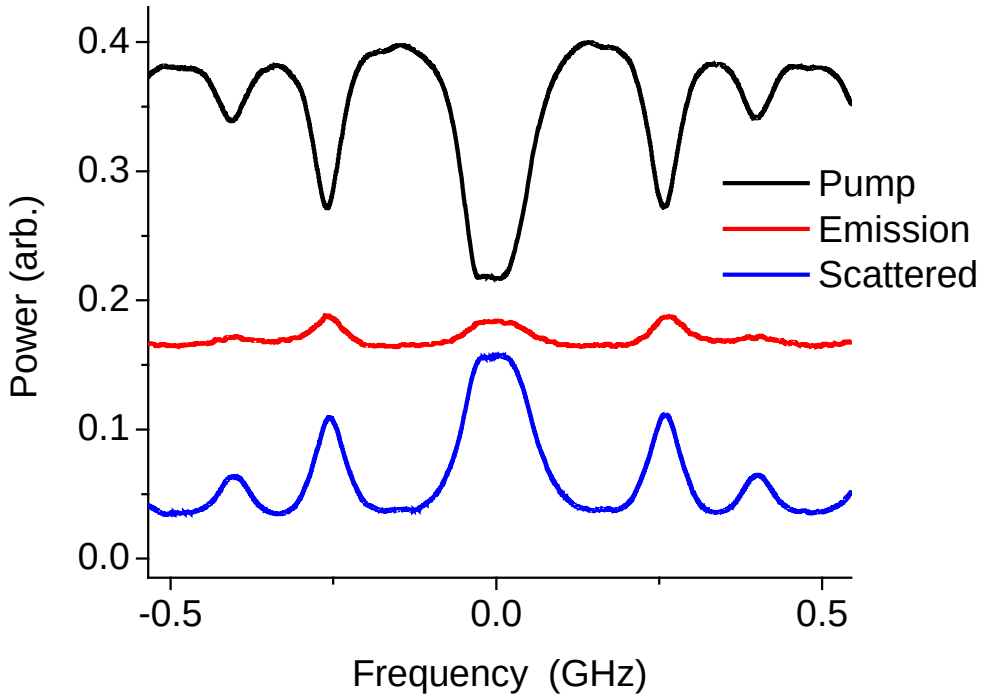

Figure V.15 The pump throughput (upper, black), the microlaser output (middle, red) and the integrated scattering loss (lower, blue) measured simultaneously as the pump is slowly scanned in frequency. The pump and scattered signals are on the same scale, while the emission signal is magnified.

An input-output curve with a horizontal axis showing the actual absorbed pump power is given in Fig. V.16. Measurement of pump scattering loss permits determination of the fraction (in the case in Fig. V.16, 20%) of the input pump loss that is actually due to absorption by the laser medium. This means that the threshold in terms of the absorbed pump power can be as low as a few hundred nanowatts.

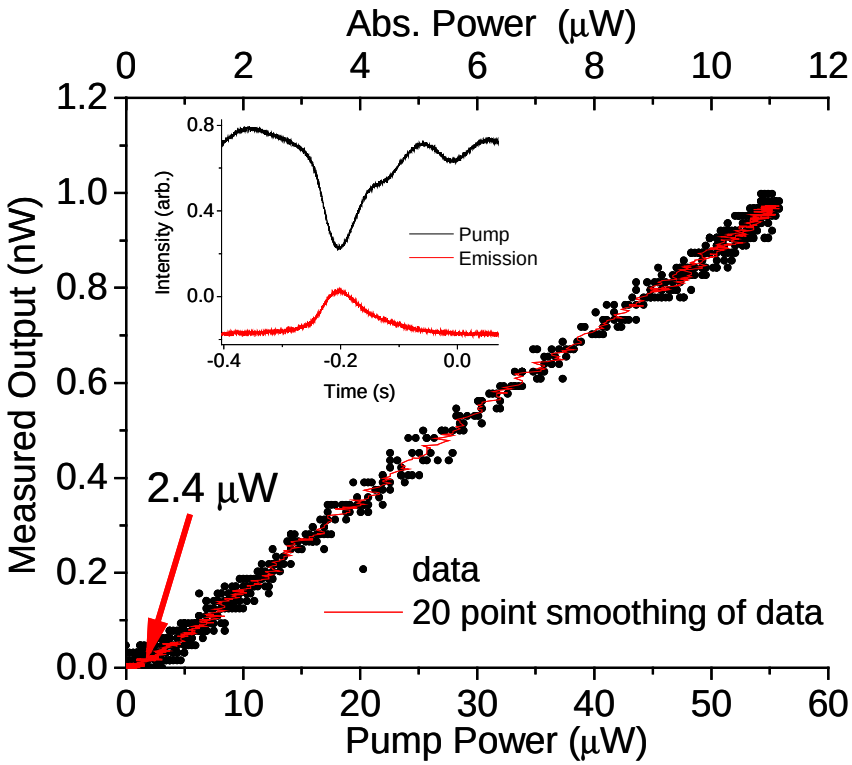

Figure V.16. Microlaser threshold determination. Pump dip depth = 68%, pump WGM $Q = 4 \times 10^6$, scattering = 80% of total pump.

V.7.4. Slope efficiency

The efficiency is defined as the ratio of the increase of emission power versus the increase of pump power in percent. Slope efficiency depends on several factors:

1. Coupling of the laser emission to the fiber: The second fiber in our experimental setup (Fig. V.7) is a 1550 nm standard optical fiber (SMA28) tapered to a diameter that is optimized for efficient coupling of the longer wavelength of emission. In a series of experiments, however, it is hard to ensure optimal coupling because one fiber will be used for multiple microspheres, the emission wavelength varies between different batches of NPs, coupling depends on the WGM, and the fiber may be misaligned and become contaminated with time. Quantitive analysis of a slope efficiency dependence on the coupling conditions is given in [101]. The parameter used in this analysis is the gap width between the microresonator and the fiber. The highest slope efficiency is reached for a gap close to the optimal gap for critical coupling and rapidly drops at overcoupled and undercoupled conditions.

2. Measuring the emission signal from only one port: In principle microlaser emission may occur in both directions, as it is sketched in the experimental setup of Fig. V.7 (red arrow inside the sphere). In this case it will couple out into both fibers and in both directions. In practice we have measured emission in both directions; however, the more common outcome is to have emission only in the pump direction. Why there is a preferred direction is a subject of further investigations.

3. We have found experimentally that the efficiency of the laser emission depends on the excitation wavelength. The emission efficiency increases if the pump wavelength is changed towards the peak associated with the first excited state. If the size

dispersion in the nanoparticle solution is very low it is possible to identify the excitonic transition wavelengths from an absorption spectrum at room temperature (Fig. V.17). The positions of these peaks depend on the average size of the NPs in the solution. The peak at 960 nm corresponds to the measurements for absorption of HgTe presented in the literature (between 900 nm and 1100 nm, depending on the average size) [27].

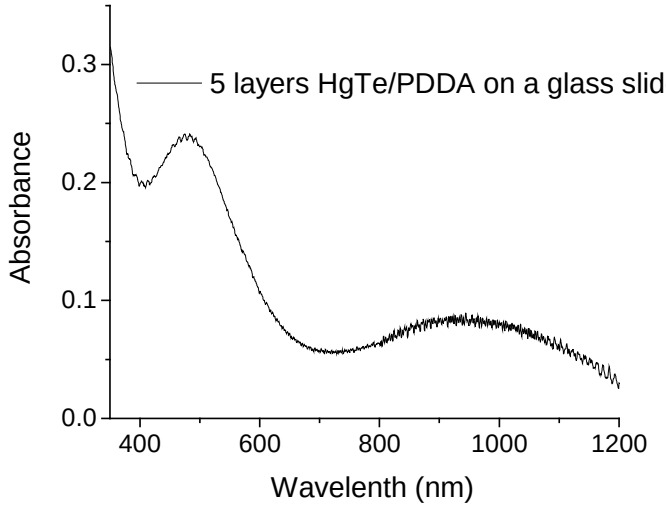

Figure V.17. Absorption of five bilayers of HgTe/PDDA deposited on a glass slide.

The dependence of emission efficiency on the pump wavelength is shown in Fig. V.18. In this figure, the efficiency is based on the total pump power. Because of this and the factors mentioned above, the measured slope efficiency is always smaller than the optimal and it differs significantly between experiments. For this experiment we used a size-selected sample produced by capillary electrophoresis. Particles were collected in two selections. The first (which was used for coating the microsphere resonator) was around the average size in the prepared NP solution – 3 nm. The second consisted of larger particles formed during the growth process, or as a result of ripening or clustering.

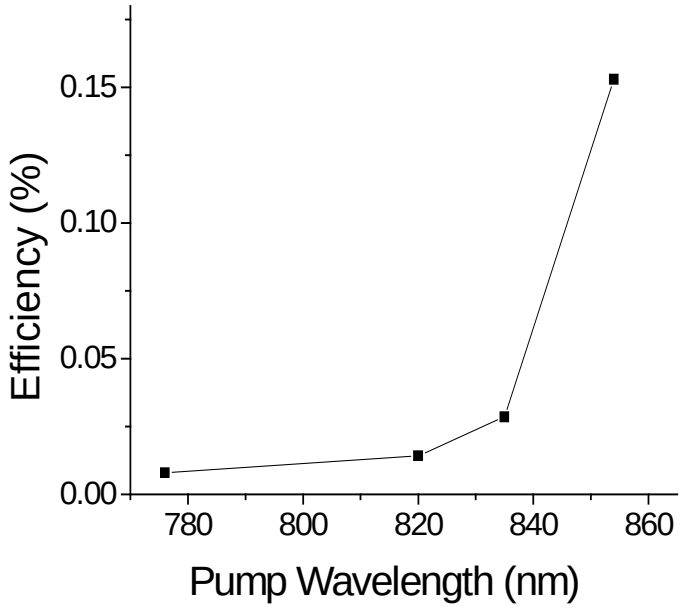

Figure V.18. Efficiency of the laser emission as the pump wavelength is changed towards the absorption maximum of the first excited state.

V.7.5 Polarization dependence

There is not significant dependence on polarization. We have found that either pump polarization produces emission of both TE and TM polarizations with similar powers. Polarized photoluminescent spectra of CdSe QDs have been studied and attributed to deviation from the spherical shape. Theoretical analysis [106] shows that this asymmetry leads to splitting of the degenerate ground hole state into a doublet. This leads to a conclusion that our NPs must be nearly spherical.

V.8 Analysis of the microlaser threshold behavior

The experimental results are analyzed with the theory of a thresholdless laser discussed in Section V.4. The results of the input-output measurements presented in Fig. V.13 and Fig. V.16 were normalized and fitted to (V.25), in which Γ_1 is taken as a large number (relaxation rate of the lower level is fast), so that

$$I = \frac{1}{2}(r-1-c) + \frac{1}{2}\sqrt{(r-1-c)^2 + 4cr}\,, \tag{V.28}$$

and the normalization is done as:

$$I = \frac{P_{out}}{P_{sat}} \text{ and } r = \frac{P_{in}}{P_{th}} \tag{V.29}$$

where P_{out} is the measured emission power, P_{sat} the saturation power, P_{in} pump power, and P_{th} the threshold pump power. P_{in} and P_{th} refer to the total pump power and not to the actual absorbed pump power. For pump rates far above threshold ($r \gg 1+c$), (V.28) becomes

$$I = r - 1 \tag{V.30}$$

From this equation the saturation power can be expressed as:

$$P_{sat} = \frac{dP_{out}}{dP_{in}} P_{th}, \tag{V.31}$$

so it is given from the measured slope of the input-output dependence far above threshold and as a function of P_{th}.

The fitted parameters were P_{th} and c. The results are shown in Fig. V.19. The experimental results from Fig. V.19(a) were fitted to the theoretical curve with:

$c = 0.16 \pm 0.05$ or $\beta = 0.24 \pm 0.07$, and

$P_{th} = 2.4\ \mu W$.

Similarly the results from Fig. V.19(b) were fitted with:

$c = 0.25 \pm 0.10$ or $\beta = 0.33 \pm 0.14$, and

$P_{th} = 2.5\ \mu W$.

The threshold power obtained from the fit is consistent with the one measured directly from the input-output dependence. The high capture fraction of spontaneous emission (β) is consistent with expectations for this type of laser, but the results are valid under the assumption that at low pump power emission is either single mode or multimode with equal threshold powers.

It is important to remember that the theoretical input-output dependence was derived for a single mode laser. The results will be relevant for our system if all QDs of the same size and shape contribute to only one lasing mode and all lasing modes have very similar threshold powers. For the second assumption to be valid the losses of the modes have to be similar, which is true for modes of different polar orders. No mode competition is expected since the homogeneous linewidth is on the order of the cavity linewidth and smaller than the mode spacing at the lasing frequencies.

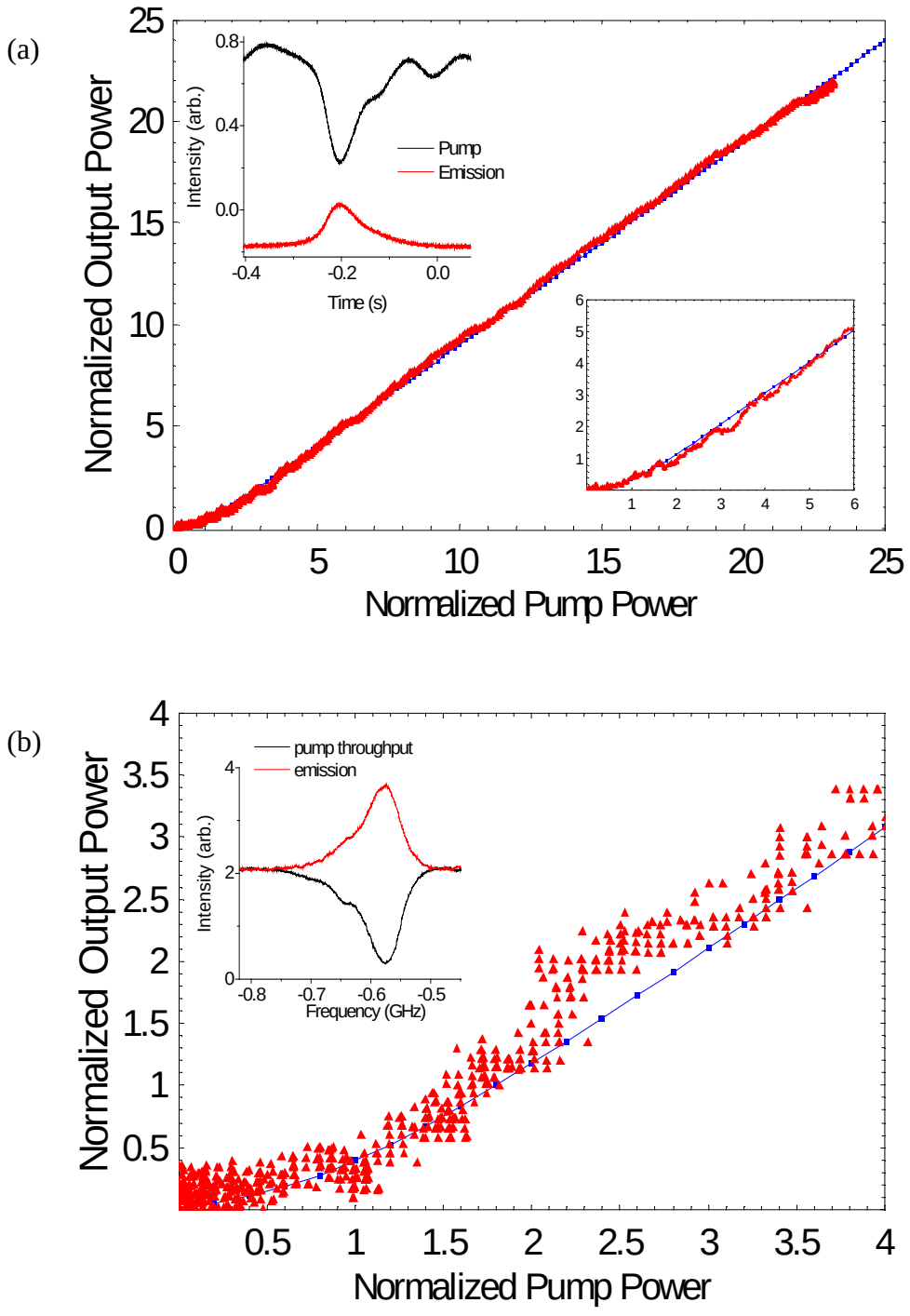

Figure V.19. Experimental results of (a) Fig. V.16 and (b) Fig. V.13 fitted to the thresholdless laser model.

V.9 Changes in pump dips as the laser emission turns on

The laser threshold can also be observed based on the effect of lasing on the pump resonances (throughput dips) (Fig. V.20).

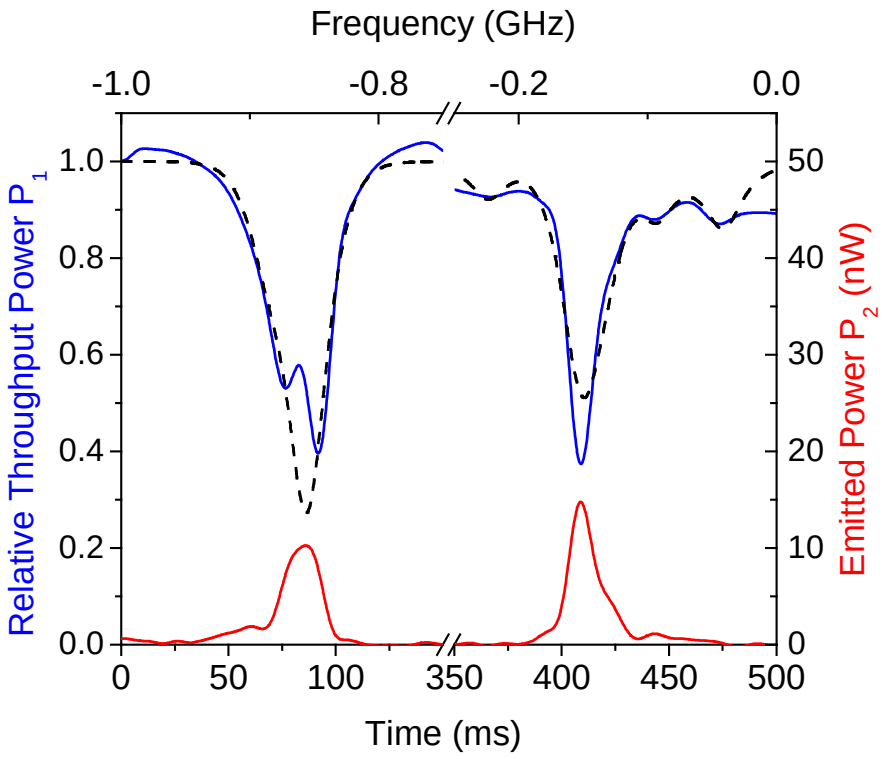

Figure V.20. Effect of lasing on pump throughput. The upper oscilloscope traces are pump throughput (left axis) and the lower are microlaser output (right axis), recorded simultaneously as the pump scans in frequency. The time scale is shown at the bottom and the relative pump frequency is shown at the top. Left: undercoupled pump mode; right: overcoupled. The dotted curves are fits showing approximately what the pump dips would look like in the absence of lasing-enhanced absorption.

When microlaser emission occurs, the pump absorption increases due to lasing-enhanced recombination, as shown in section V.3. When the pump WGM is overcoupled (coupling loss greater than intrinsic loss), this increase in its intrinsic loss drives the

system closer to critical coupling, increasing the dip depth. This was observed for the HgTe QD laser of Fig. V.12 (experimental points in red), where the dip got 2.5% deeper as the total pump power increased from 7.2 μW to 470 μW. For an undercoupled WGM, the pump dip depth decreases when a laser mode turns on. Examples of both undercoupled and overcoupled pump modes are shown in Fig. V.20.

The effect of lasing on the pump dips was also measured simultaneously with the scattered signal. Results are given in Table V.2.

	Input Power (μW) P_{in}	Power Loss (μW) P_{loss}	Power Scattered (μW) P_{sctr}	Power Absorbed (μW) P_{abs}	Dip Depth %	P^*_{sctr}/P_{input}	P_{abs}/P_{loss}
Overcoupled	47.05	13.88	10.17	3.70	29.50	0.307	0.26
	75.04	22.72	16.47	6.25	30.20	0.307	0.27
	177.65	53.73	36.89	16.84	30.31	0.307	0.31
Undercoupled	49.54	22.76	15.96	6.8	46.00	0.408	0.30
	78.07	35.85	24.35	11.5	45.90	0.398	0.32
	182.00	82.44	54.78	27.6	45.29	0.398	0.34

Table V.2. Changes in dip depth with increase of input power for overcoupled and undercoupled modes. All measured parameters are sketched in Fig.V.21. Dip Depth represents the ratio P_{loss}/P_{in}.

The changes in two pump dips at different coupling regimes were observed. The input power is off-resonance throughput measured by detector P1; power loss is the on-resonance drop in the throughput (total pump); power scattered is the integrated power measured by detectors P3 and P4; power absorbed is essentially the difference between the power loss and the power scattered. The sketch in Fig. V.21 represents the measured parameters from Table V.2. P^*_{sctr}/P_{input} gives the ratio of the total scattered power to the

off resonance input. Measurements show that it stays constant as the input power increases. On the other hand the ratio of the absorbed power to the power loss at resonance increases, while the dip depth increases in the case of overcoupled mode and decreases if the mode is undercoupled.

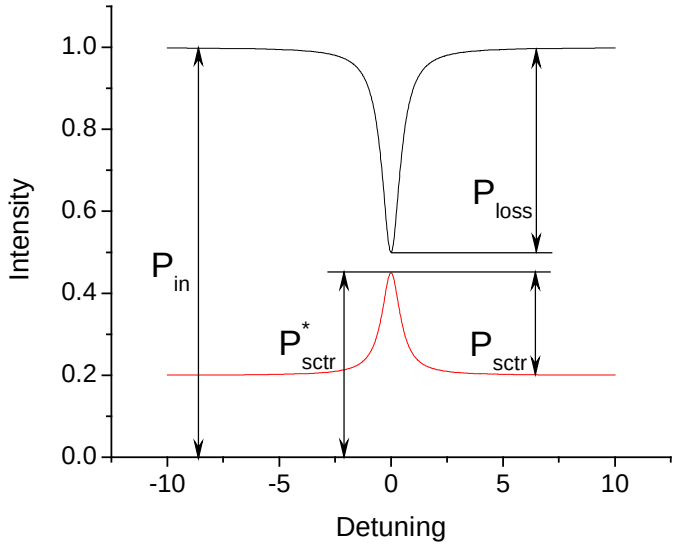

Figure V.21. Representation of the measured parameters included in Table V.2.

The results in Table V.2 show that while the scattered signal is proportional to the input power, the absorbed fraction increases. This results in an increase of the dip depth in the case of an overcoupled mode and a decrease of the dip depth in the case of an undercoupled mode. This may also explain why some of our input-output curves (using the total pump) look nonlinear at relatively low incident pump powers (above 200 μW), since the absorbed power is actually not linearly scaled with the power lost (total pump). Measurements of the threshold power (as in Fig. V.13 and Fig. V.16) were taken from scans at low input powers and their validity is justified also by the comparison with the

fitted values from Fig. V.19. Table V.2 along with the results in Fig. V.20 leads us to the conclusion that the onset of lasing can also be seen in the change of the pump WGM dip depth.

V.10 Mode selection using coupled resonators

From the relatively wide laser emission peak (~10 nm FWHM) it can be inferred that it is multimode emission. In order to observe a single mode we use a second passive resonator (2 in Fig. V.22) coupled to the coated microsphere (1) to provide mode selection. Only modes that are coresonant in both spheres would couple energy efficiently to the second fiber (see the experimental setup in Fig. V.7). The optical behavior of coupled passive resonators was previously studied in our group [107].

Figure V.22 shows the spectrum from a single resonator with gain (in black) and 20 times magnified spectrum of the coupled-resonator system (in red). The spectral width is significantly reduced and the spectral feature is symmetric. Single mode emission however has to be verified by a spectrum analyzer, a high quality scanning Fabry-Perot resonator. The power in a single mode is very low, which makes this measurement challenging and requiring further work.

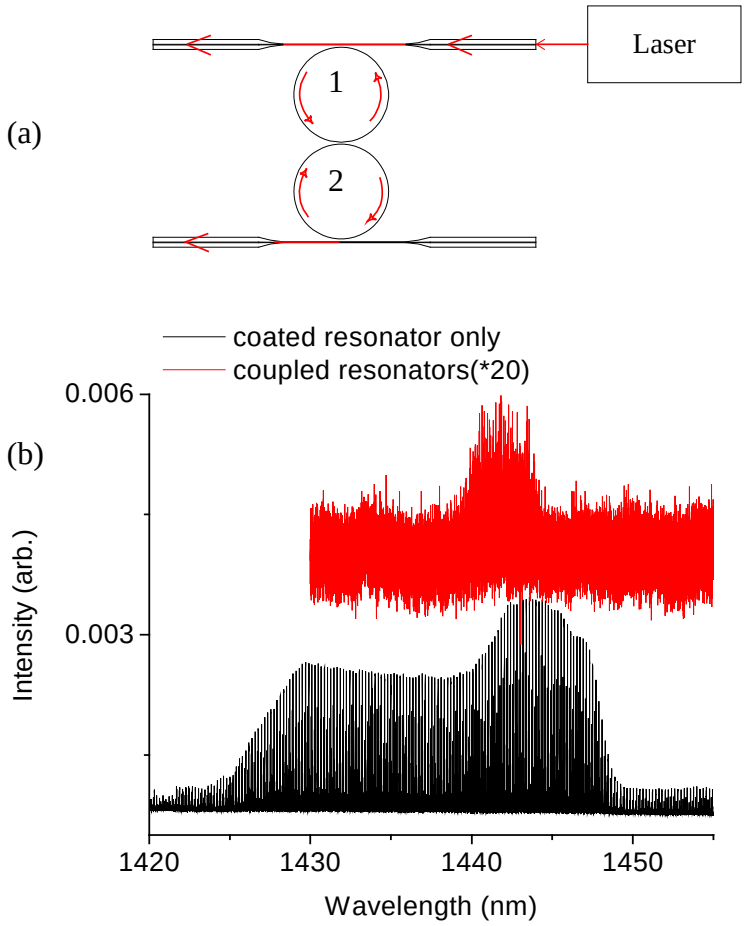

Figure V.22. (a) Schematic of coupled-resonator system. Resonator 1 is active (coated with HgTe NPs) and resonator 2 is passive. (b) Comparison between the spectrum of a single active resonator (in black) and that of a coupled-resonator system (in red).

V.11 Conclusions

In this chapter we discuss the design and emission characteristics of a WGM microlaser based on a spherical microresonator coated with semiconductor (HgTe or HgCdTe) nanoparticles. There are several advantages in the chosen design. (1) The choice of small HgTe QDs in the strong confinement regime allows for high efficiency

room temperature emission. The calculations give a large dipole moment for HgTe QDs in comparison with other gain materials. This contributes to the low threshold and also shows the suitability of the material for CQED. (2) The high quality resonator was coated with a submonolayer of the gain material, which reduces the absorption and scattering losses and ensure low transparency density. Also the use of D_2O as solvent eliminates the strong water absorption in the emission wavelength range. (3) Placing the gain material at the interface between high and low index media allows for a large capture fraction of spontaneous emission into a lasing mode and thus reduces the laser threshold.

The most interesting result that was achieved is the ultralow lasing threshold (one of the lowest in this type of laser). We prove lasing by observing several different effects: threshold in the input-output curve; spectral measurements showing the take off of the lasing modes; and the effect of lasing-enhanced absorption on the pump WGM. For better precision in threshold determination we measured the scattered pump light. We also developed a method for obtaining the input-output characteristic by following the increase in the pump power while scanning a single pump WGM. The possibility of mode selection using coupled resonators was also shown.

The future work on this project could go in two directions – fundamental and technological. Further examination of the threshold dependence on the surface coating density will help to understand better the laser dynamics as well as to approach the regime of CQED. Experimenting with other suitable gain materials, such as PbSe NPs, has already started in our lab.

Obtaining a single mode laser emission is essential for applications. For this it is important to further optimize the laser parameters such as minimizing the size dispersion in the gain material and optimizing the pump wavelength in accordance with the average

particle size. Using a second microsphere for mode selection, and optimizing the coupling between the two resonators, such that only a single mode is resonant in the coupled system is one way of achieving single mode laser. Another way would be using novel single mode WGM resonators as described in [108].

CHAPTER VI

GOLD NANOROD SURFACE PLASMON EFFECTS ON WGM RESONATORS

VI.1 Introduction

The properties of colloidal gold solutions have fascinated people for a long time. For example, gold nanoparticles have been used in ruby-colored stained glass. Specific physical and chemical properties of metallic nanoparticles have been studied from a fundamental point of view as well for their practical applications. First, in 1908, Mie [4] gave a rigorous theoretical explanation of the optical properties of metal clusters based on the absorption and scattering of electromagnetic radiation by spherical particles as discussed in Chapter II. Gans [52] developed an extension to Mie's theory that deals with particles with an elliptical shape. Only recently the properties of non-spherical particles have been utilized through control of the geometry of the particles in the process of their synthesis.

Solution-phase colloidal preparation of gold nanorods (NRs) provides a simple way of fabricating materials with tunable optical properties. The size and shape of these metallic NRs, together with the dielectric permittivity of the surrounding medium, tune the plasmon resonance of the Au NRs from the visible to the near infrared (500 nm to 1500 nm) [109, 110] spectral region. These particles have enormous extinction

coefficients that depend on their composition [55] and on the ratio of length to width, i.e., aspect ratio (AR) [111]. Unlike organic dyes or quantum dots, the Au NR plasmons do not bleach or blink [112].

Au NRs are yielded when Au nanoparticles (NPs) with various capping agents are added to an aqueous solution containing anionic gold (I) dichloride ($AuCl_2^-$), ascorbic acid, and cetyltrimethylammonium bromide (CTAB). At room temperature the reaction does not proceed at an appreciable rate until NP seeds are added because of the free energy barrier of forming a new interface. The mechanisms for Au NR nucleation and growth are currently under intense investigation [113, 114].

To utilize these particles in chemical and biological sensors, as well as in other optical devices, immobilization is required. Two different approaches have been used: (1) immobilizing Au nanorods from solution by using one or a few intermediate layers, such as self assembled monolayers of mercaptohexanoic acid (MHA-SAM) or polyelectrolytes, on the substrate surface [54, 110], and (2) direct growth on the surface. In the second approach, gold NP seeds are attached to the surface prior to immersing the substrate in the growth solution [115-118].

The contribution of this work is that it utilizes semiconducting HgTe NP seeds capped with thioglycolic acid (TGA) to nucleate gold NRs with morphology comparable to previous work [117, 118], which uses Au NP seeds. There are advantages to using HgTe NPs to initiate Au growth. Our method is a simple way to coat surfaces having different electrical and optical properties with a submonolayer of semiconducting NPs using an intermediary polyelectrolyte layer [104], initiating growth of rods directly on the surfaces. The poly(dimethyldiallylammonium) chloride (PDDA) layer serves not only to attach seeds and NRs to the surface, but also assists in the one-dimensional growth

process. Thus, we achieve growth of Au NRs directly on the surface of high quality optical resonators [41]. Another reason for the use of semiconducting HgTe NP seeds is that they have electronic states in the same spectral region (500 nm to 2000 nm) [33, 119] as the longitudinal mode of the metallic Au NR plasmon. This offers a possibility of synthesizing composite nanomaterials with unique optical and electrical properties. Finally, nanorods have significantly lower plasmon dephasing rates in comparison with those of small nanospheres [120] due to a suppression of interband damping. A WGM optical resonator can further amplify and modify the local fields. It was shown that surface propagating modes transmit energy between pairs of dipoles on the surface and thus modify dipole-dipole interaction [121]. The interactions between strong local fields and semiconductor nanoparticles are also expected to enhance the nonlinear effects.

VI.2 Synthesis

VI.2.1 Two stage coating process

This section describes a synthesis of gold nanorods directly on different dielectric surfaces. It is based on the solution seeded nanorod synthesis protocol developed by Murphy and coworkers [122], but uses a reduced CTAB concentration [114]. The technique consists of two major stages (Figure VI.1) – first, coating the surface with a submonolayer of semiconductor nanoparticles (HgTe), and second, immersion in growth solution.

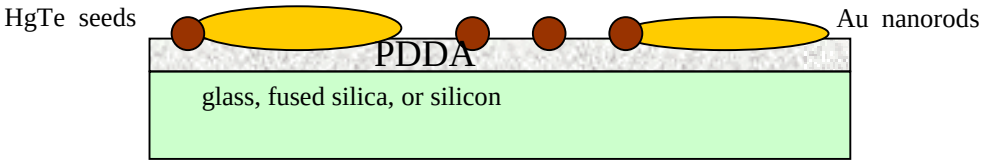

Figure VI.1. Schematic of the surface coating of the substrate.

The three-step procedure for growing Au NRs from HgTe NPs bound to surfaces is depicted in Fig. VI.2(a)-(c). In the first step, based on the layer-by-layer technique [104], the surface is dipped in an aqueous solution of poly(dimethyldiallyammonium) (PDDA) chloride for ~30 minutes (Fig. VI.2(a)). This polyelectrolyte coating is applied to glass, mica, fused silica, and silicon surfaces. After washing with deionized water, the substrate is dipped in an aqueous solution of thioglycolic acid (TGA)-capped HgTe NPs for ~5 s to deposit a fraction of a monolayer of HgTe particles (Fig. VI.2(b)) [40]. The concentration of seeds on the surface was kept low, approximately 20-40 NPs/μm^2, to enable the growth of well-separated Au rods. The negatively charged carboxylate group of the HgTe NP capping agent is electrostatically bound to the quaternary amines of PDDA, and the interaction is strong enough to withstand washing with water. Next, the substrates are immersed in a gold growth solution of 1.3×10^{-4} m (molal) tetrachlorauric acid ($HAuCl_4$ - 99%, Sigma-Aldrich), 8.0×10^{-3} m cetyltrimethylammonium bromide (99%, Sigma-Aldrich), and 1.9×10^{-4} m ascorbic acid (99%, Sigma-Aldrich).

The ascorbic acid reduces $AuCl_4^-$ to $AuCl_2^-$ and other Au^+ species before the substrate is dipped into the solution. Further reduction to metallic Au is enabled by the heterogeneous nucleation induced by the HgTe NP seeds. Originally transparent samples begin to turn pink in approximately 5 minutes, indicating Au deposition on the surface.

As a control, a glass slide coated only with PDDA was immersed in the growth solution and kept there for 3 hours. No surface changes or coloration of the solution was observed. Figure VI.2(c) depicts one possible outcome, in which the HgTe seed induces rod growth in such a way that it remains at one end of the NR. It is also possible that Au growth occurs on two opposite sides of the HgTe crystal.

VI.2.2 The interpretation of the Au rod growth mechanism

When Au NPs are used as seeds, multifaceted particles up to a size of approximately 20 nm form before anisotropic rod growth begins [123]. At this size, rod growth begins because the crystal is large enough for the preferential binding of CTAB to (110) or (100) crystal faces [118]. This hinders growth asymmetrically, allowing faster growth along directions free of CTAB. The positively charged quaternary amines of CTA^+ are attracted to the Br^- layer that is adsorbed to the lateral faces of the NRs. A bilayer of CTAB forms that shields the aliphatic tail of the surfactant from the aqueous environment (not shown in Fig. VI.2(c)) [110, 114, 122, 124]. Both HgTe and Au form face-centered cubic structures, but the lattice constants are 0.65 nm and 0.41 nm, respectively. This implies that the elastic strain and defect density in the first few layers of Au atoms to deposit is greater when HgTe seeds are used and suggests that anisotropic growth could start even earlier than in the synthesis that uses Au seeds. The PDDA-derivatized surfaces may play a similar or competitive role to CTAB in the growth mechanism because the quaternary amines of PDDA are also electrostatically attracted to the Br^- layer. This interaction attaches the NR to the surface without an intermediary CTAB layer. Figure VI.3 presents the structural formulas of all organic compounds used

in the proposed synthesis of Au NRs. The addition of $AgNO_3$ increases the yield of rods. Fast growth is likely to produce more spheres than slow growth. Full control of the process has not yet been achieved.

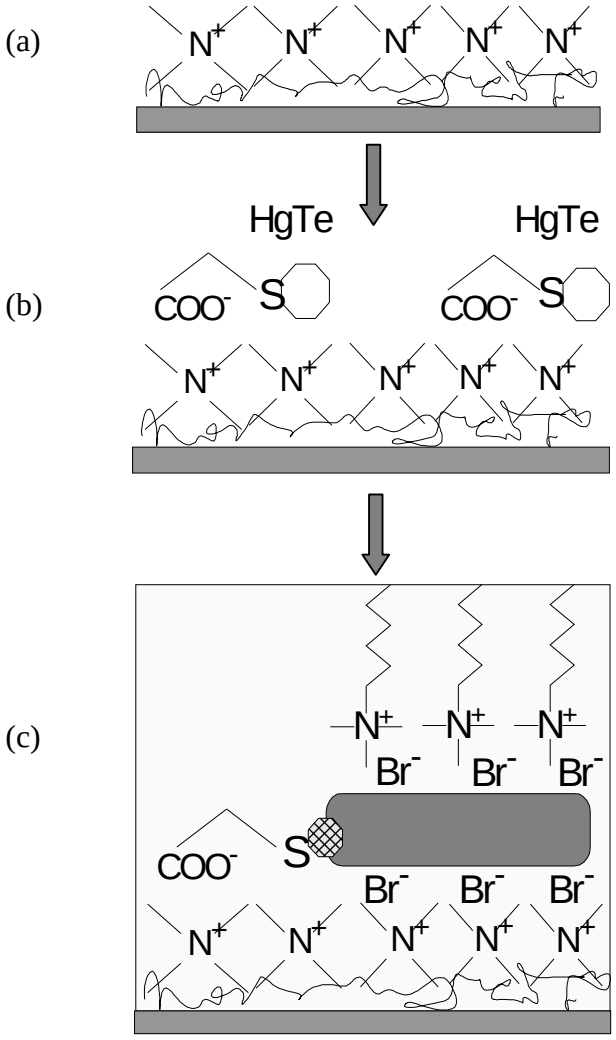

Figure VI.2. (a) The substrate is coated with a monolayer of PDDA, washed with deionized water and dried. (b) A submonolayer of HgTe NPs, capped with TGA, is formed on top of the PDDA layer. (c) The sample is immersed in Au growth solution, where one-dimensional growth is assisted by the presence of CTAB and the PDDA layer.

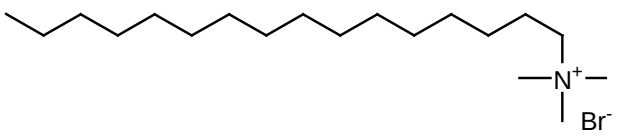

cetyltrimethylammonium bromide

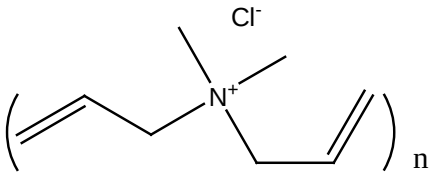

poly(dimethyldiallylammonium) chloride

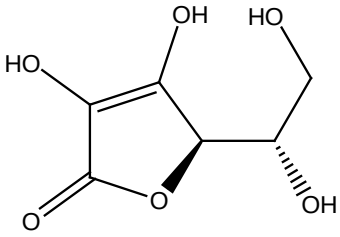

ascorbic acid

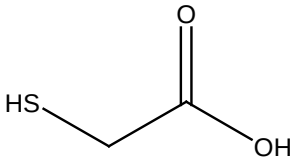

thioglycolic acid

Figure VI.3. The organic compounds used in HgTe NP-Au NR formation.

VI.3 Results and discussion of growth technique

Gold rods were grown on several different surfaces (glass, fused silica, silicon, mica, and Ni formvar-coated TEM grids) as the two-stage procedure described in section VI.2.1 was followed. Many different experimental techniques were used to prove the claims made in this work. Transmission electron microscopy (TEM), scanning electron microscopy (SEM), atomic force microscopy (AFM), visible and near infrared extinction spectroscopy, energy dispersive atomic x-ray spectroscopy (EDX), and x-ray photoelectron spectroscopy (XPS) are used to characterize the samples. TEM is performed with a JEOL (JEM 100 CX II) at 100 kV and SEM with a JEOL (JXM 6400)

at 30 kV. AFM results are from a Digital Instruments Nanoscope IIIa. The extinction spectroscopy experiments are carried out using a Varian Cary 5. EDX measurements are from an EVEX Analytical System. Finally, XPS measurements are performed with an Mg anode and a PHI double-pass cylindrical mirror analyzer with a pass energy of 50 eV.

VI.3.1 Growth of gold nanocrystals on different surfaces

The technique discussed in section VI.2 is amenable to many surfaces with different electronic and optical properties. Substrates used for growing gold nanorods were formvar-coated grids (Fig. VI.4), mica (Fig. VI.5), glass (Fig. VI.6), fused silica, and silicon (Fig. VI.7). TEM (Fig. VI.4), SEM (Fig. VI.5), and AFM (Fig.VI.6 and VI.7) images were acquired to observe the morphology of single gold nanocrystals, as well as to estimate the yield of nanorods versus other shapes.

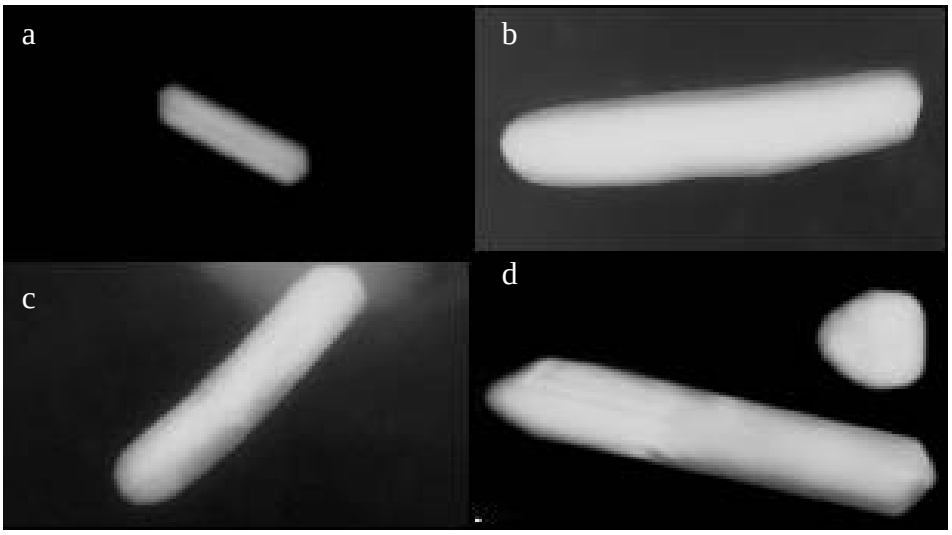

Figure VI.4. TEM images of Au rods nucleated with HgTe NPs on TEM formvar-coated grids. Rod size: (a) 128.5 × 35.7 nm; (b) 270 × 62.9 nm; (c) 262 × 55.2 nm; (d) 333 × 66 nm.

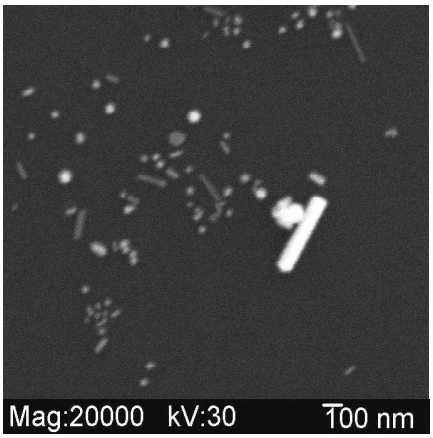

Figure VI.5. SEM image of gold rods and spheres on a mica surface.

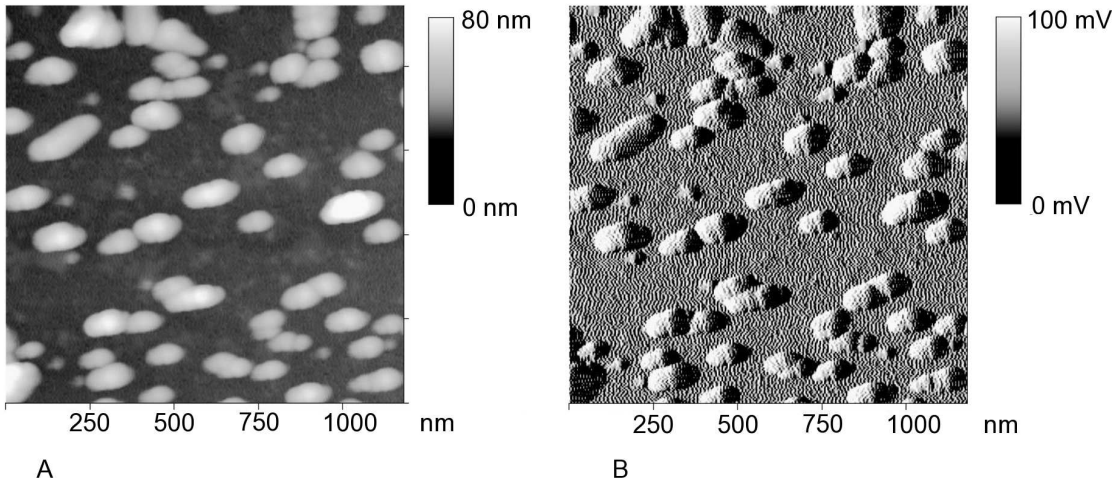

Figure VI.6. AFM height (A) and amplitude (B) images of gold rods grown on a microscope glass slide. The scan size is 1.18 µm and the maximum height on the brightness scale is 80 nm.

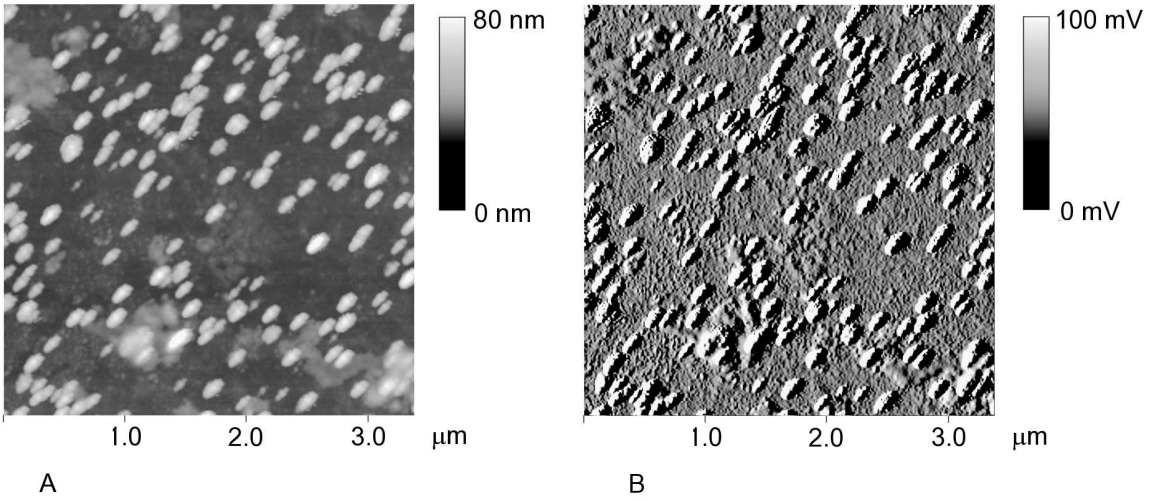

Figure VI.7. AFM height (A) and amplitude (B) images of gold rods grown on silicon. The scan size is 3.33 μm and the maximum height on the brightness scale is 80 nm. Average length is 150 to 200 nm; aspect ratio is 2 to 3.

Growth occurs on all these surfaces after applying the same procedure. The presence of gold on the surfaces was confirmed by several different methods.

1. Backscattered electron images of the surface (Fig. VI.8) taken with JEOL (JXM 6400) show bright objects, which is an indication of metal surfaces, i.e., gold nucleated by HgTe NP seeds. Samples were coated with carbon to prevent accumulation of charge on the surface.

2. Energy dispersive X-ray analysis (EDX) (Fig. VI.9) on the same surface shows an Au peak. The problem with this technique is that the peak of EDX for Hg overlaps with the Au peak. The resolution capabilities of the instrument are not enough for resolving the two peaks.

3. X-ray photoelectron spectroscopy gave clear evidence of Au presence (Fig. VI.10). With increasing immersion time in the growth solution, the intensity of the Au doublet ($4f_{7/2}$ and $4f_{5/2}$ transitions) increases relative to the intensity of the Si ($2p_{3/2}$

transition) peak, which comes from the substrates. All samples in this experiment were prepared on glass slides.

(a) 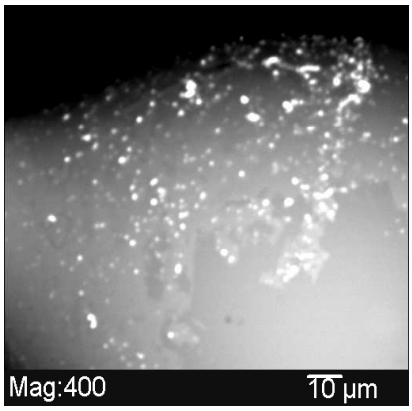

(b) 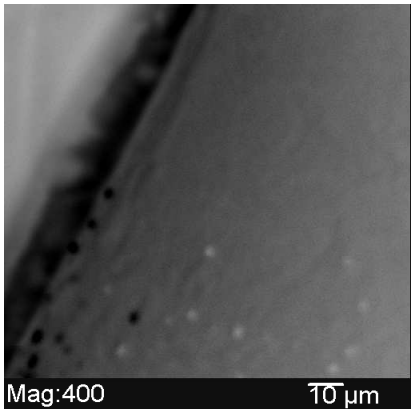

Figure VI.8 SEM images after immersion in Au growth solution. (a) HgTe seeds present; (b) no HgTe seeds.

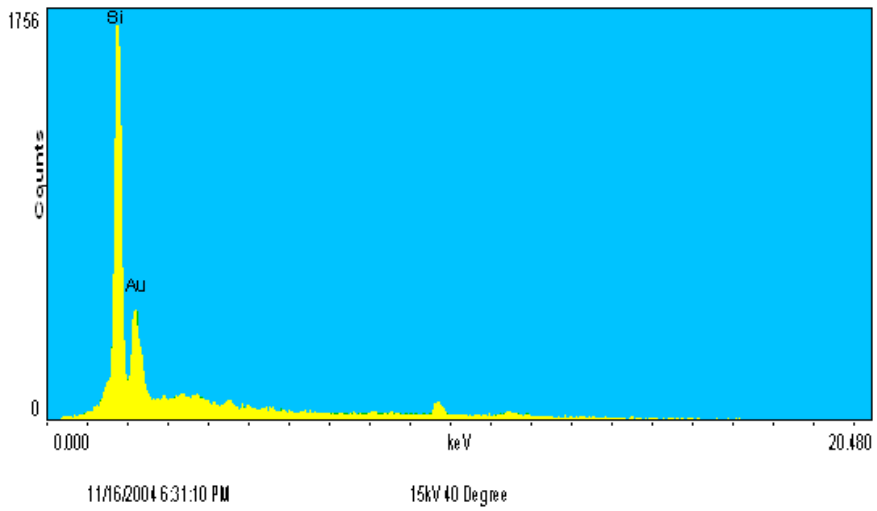

Figure VI.9 EDX taken on the surface of the fused silica microsphere of Fig. VI.8(a) – identification result: Si, 1.763 keV; Au, 2.230 keV.

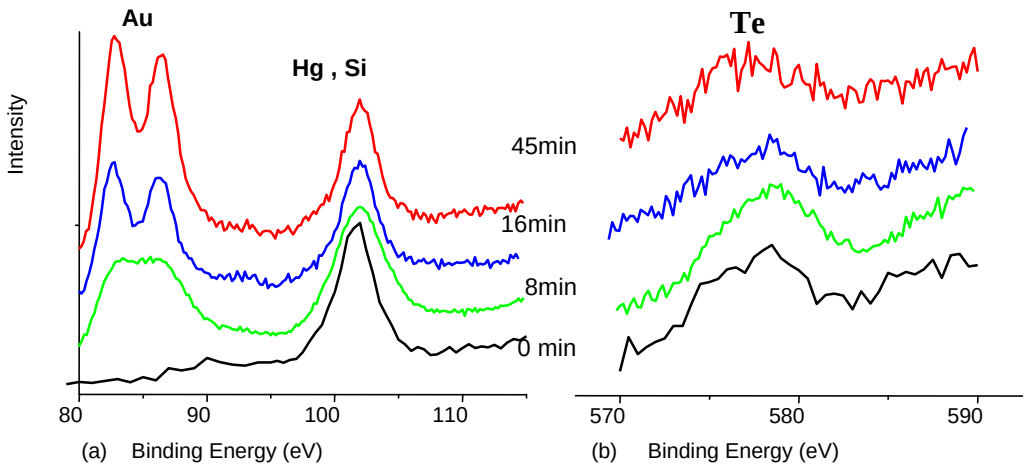

Figure VI.10. XPS of glass slide surface coated with HgTe seeds only (black), and after immersion in gold growth solution for various times. (a) The Au doublet is at about 84 eV and the Hg peak at 99 eV overlaps the Si peak at 102 eV. Relative growth of the Au peak in comparison with the Si peak is evident. (b) Position of the Te $3d_{5/2}$ transition for different samples.

4. Absorption spectra of the surfaces were taken with the Varian Cary 5. As a reference we used a PDDA coated glass slide. Figure VI.11 shows the peak of Au plasmon absorption. The samples are the same as those used in the XPS measurements, except for the first, which was a glass slide coated with PDDA and immersed in gold growth solution for 45 min. Only one surface plasmon peak was detected, which was expected in air for particles with a small aspect ratio. AFM measurements show the presence of spheres (radius of 20 to 50 nm) and rods with AR < 3. The 45-minute sample resulted in an almost complete monolayer of gold particles on the surface. Figure VI.12 shows spectra of samples immersed in different batches of Au growth solution. Although the presence of rods is indicated by the shoulder above 600 nm, spheres are dominating rods in all samples.

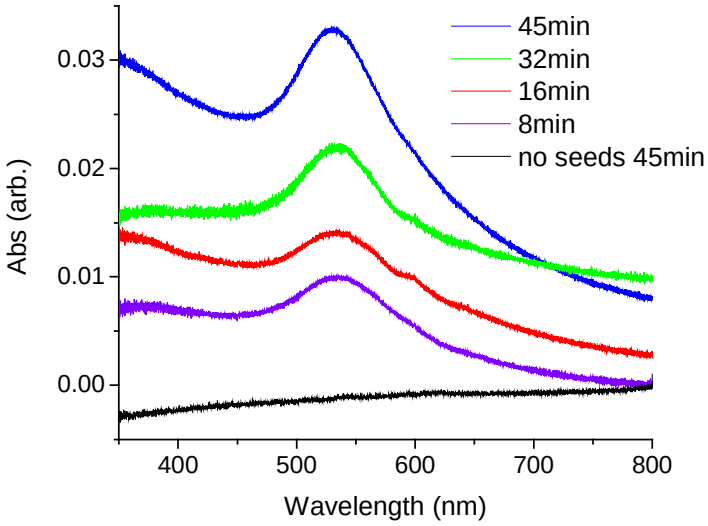

Figure VI.11. Absorption measurements of glass slides coated with PDDA and HgTe NPs kept in gold growth solution for different times. The first scan (black) is a control sample initially coated only with PDDA.

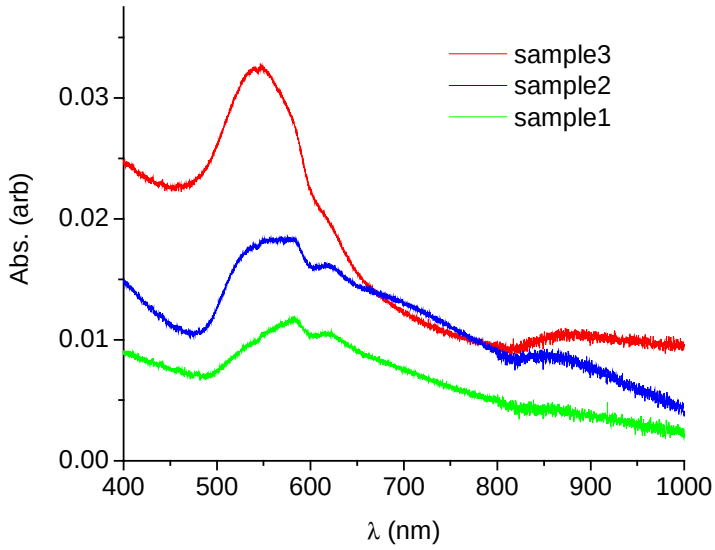

Figure VI.12. Absorption measurements of glass slides coated with PDDA and HgTe NPs. Different batches of growth solution (slightly different concentrations of CTAB and $AgNO_3$) were used.

VI.3.2 Role of HgTe nanoparticles in initiating Au growth

Although the exact mechanism of Au growth on HgTe nanocrystals is not yet clear, the possible mechanism that was discussed in section VI.2.2 and shown in Fig. VI.2 is well supported by our experimental data. As control experiments, clean glass substrates, PDDA coated glass slides, and PDDA coated silica microspheres of ~500 μm diameter are exposed to the gold growth solution. No change of color is observed on the sample or in the solution during 45 minutes of exposure. Further examination of the initially PDDA coated samples with SEM and absorption spectroscopy does not show growth of gold particles on the surface. Also no color change is observed in 45 minutes when PDDA or the sodium salt of 2-thiobenzoic acid (sodium mercaptobenzoate) are added separately or together with the gold growth solution. In conclusion, bare substrates, PDDA, and water soluble thiol-containing species like TGA do not induce nucleation of nanoparticulate Au.

Additional evidence that Au NRs are nucleated by HgTe NPs is provided by XPS. Figure VI.10(b) shows the intensity of the Te $3d_{5/2}$ peak (which overlaps the less intense Hg $4p_{3/2}$ peak). The intensity of the Te peak was compared with the intensity of the Si and Au peaks from Fig. VI.10(a). The ratio of the Te to Si peaks remains constant, while the ratio of Au to Si peaks grows with time. The relatively low Au/Te ratio (below 10) suggests that not all the seeds are contributing to the nucleation of gold. The position of the Te $3d_{5/2}$ peak suggests that Te is in an oxide form in all the samples prior to immersing in Au solution. This might be caused by the large surface to volume ratio of HgTe NPs (3 nm in diameter). The position of the Te peak does not change with the increase of time of immersion, indicating that Te does not react with the components of the gold growth solution. The position of the Hg $4f_{7/2}$ transition also does not change

during the process of growth, but it is harder to compare because it overlaps with the Si $2p_{3/2}$ transition (Fig. VI.10(a)).

VI.4 Enhancement of evanescent coupling to whispering-gallery modes caused by Au NRs grown on a microresonator surface

Incident light on the interface of a thin metal layer and a dielectric surface can cause free charge oscillations, called surface plasmons (SPs). Surface plasmon resonance occurs when the momentum of the incident light matches that of the SPs. In general, a SP can be excited by a plane-wave coupler, which can be a prism [125, 126], a grating structure [127-129] or random surface roughness [130]. Applications of the evanescent field of a waveguide for the resonant excitation of SPs are described extensively in the literature [131, 132]. The presence of the metal layer on the waveguide surface converts the waveguide mode into a waveguide-surface plasmon coupled mode, which highly enhances the evanescent field [133]. Such structures are used as sensors because they can combine the SP-enhanced evanescent field with simple surface functionalization techniques [133, 134]. One advantage of using a layer of a metal nanorods instead of a metal film is the possibility to tailor the spectral position of the surface plasmon resonance by controlling the aspect ratio, as shown in Chapter II. Further optimization of the sensitivity of waveguide-surface plasmon coupled sensors was proposed by using metal nanoparticles deposited on the surface of the fiber [135, 136].

We have investigated optical properties of a dielectric microresonator coated with gold nanorods. The surface plasmon resonances of Au nanoparticles are excited by the evanescent field of a WGM supported by the microsphere resonator. Enhancement of the

evanescent field caused by resonant excitation of the SPs produces changes in the coupling of light from the resonator to a tapered optical fiber. Our measurements show coupling enhancement by a factor greater than 200. This is a result of the significant field enhancement that can be realized in these structures.

VI.4.1 Gold rods on the surfaces of fused silica microspheres

Permanent attachment of gold nanorods with controllable density on the surface of a dielectric microsphere resonator was achieved using the growth technique described above. Nanorods were nucleated using thioglycolic acid-capped HgTe nanoparticles adsorbed to a polyelectrolyte intermediary layer directly on the surface of a high-quality optical microresonator [41]. This technique results in about 30% rod-shaped particles with variable aspect ratios and about 70% spherical particles on the surface of the resonator. The initial Q factor of the resonators at $\lambda = 830$ nm before coating the surface is typically more than 10^8. After growth, the quality factor is reduced but still on the order of 10^5-10^6 if the nanoparticles (nanorods and nanospheres) are only a fraction of a monolayer. Figure VI.13(a) is a photograph of a 450-μm (diameter) sphere. Gold growth on the surface causes the pale pink color. Figure VI.13(b) shows a scanning electron micrograph of the surface of a microsphere coated with gold nanoparticles. The vertical trace was left by an optical fiber used to couple light into the sphere.

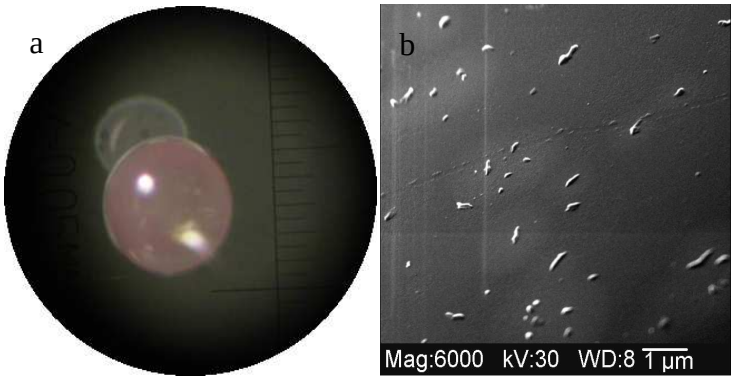

Figure VI.13. (a) Microsphere coated with Au NRs. The smallest division on the scale is 50 μm. (b) Scanning electron micrograph of the surface of a coated microsphere.

VI.4.2 Experimental setup and results

A simplified schematic of the setup is shown in Fig. VI.14. Light from a cw laser (Ti-sapphire with a wavelength tunable from 780 to 850 nm or diode with a wavelength of 1550 nm) is launched into a single-mode optical fiber that is tapered for coupling. The polarization incident on the microresonator can be selected by a polarization controller (PC), and a polarization analyzer (PA) reads the polarization of the light coupled back to the fiber. From the tapered part of the fiber, light is evanescently coupled to the whispering gallery modes (WGMs) of the microresonator. As the input light is scanned in frequency, dips in throughput correspond to WGM resonances. The WGMs are classified by the ratio x of coupling loss to intrinsic (absorption and scattering) loss: overcoupled, $x > 1$; undercoupled, $x < 1$; critically coupled, $x = 1$, as discussed in Chapter III.

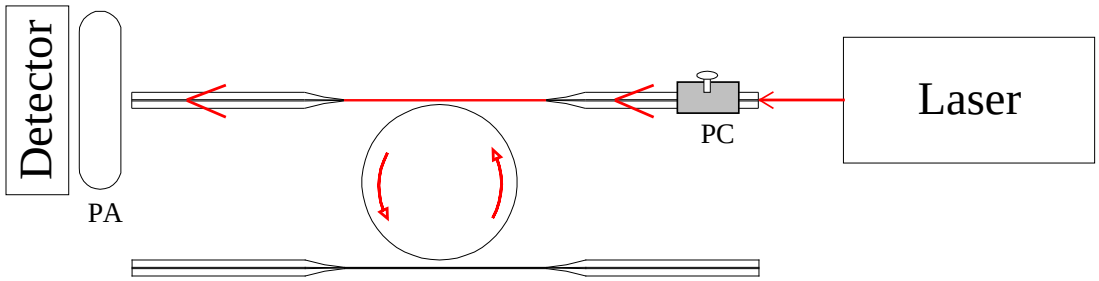

Figure VI.14. Light (polarization controlled by PC and analyzed by PA) is evanescently coupled to the whispering gallery modes (WGMs) of a microresonator on which Au NRs have been grown. The second fiber is brought into contact with the microsphere to probe the coupling regime of the resonator.

An important step is to have a method to check the WGMs for their coupling condition. Bringing a second fiber close to the microsphere effectively increases the intrinsic loss. Adding this extra loss makes the dip of an overcoupled mode deeper, and that of an undercoupled mode shallower.

The laser wavelength was scanned several GHz around 830 nm. The microspheres ranged between 400 and 700 μm in diameter. Using the test fiber, we verified that the modes of a bare sphere can range from undercoupled through critically coupled to overcoupled. The microsphere resonator was tested again after coating it with a polyelectrolyte layer (PDDA). Because of additional losses introduced with this layer, such as absorption and scattering, the intrinsic quality factor of the coated resonator drops by about an order of magnitude. Therefore, the PDDA coated microresonator coupled to the tapered fiber (keeping similar coupling conditions – fiber and sphere in contact) resulted in mostly undercoupled modes (Fig.VI.15(a)). After growing gold NRs on the surface of the same resonator, it was tested again using the same setup. As Fig. VI.15(b) shows, almost all the modes are strongly overcoupled. Although adding some intrinsic

losses (about 50%) because of the absorption and scattering from Au NRs at the wavelength of excitation, the coupling losses appeared to be more than 200 times greater.

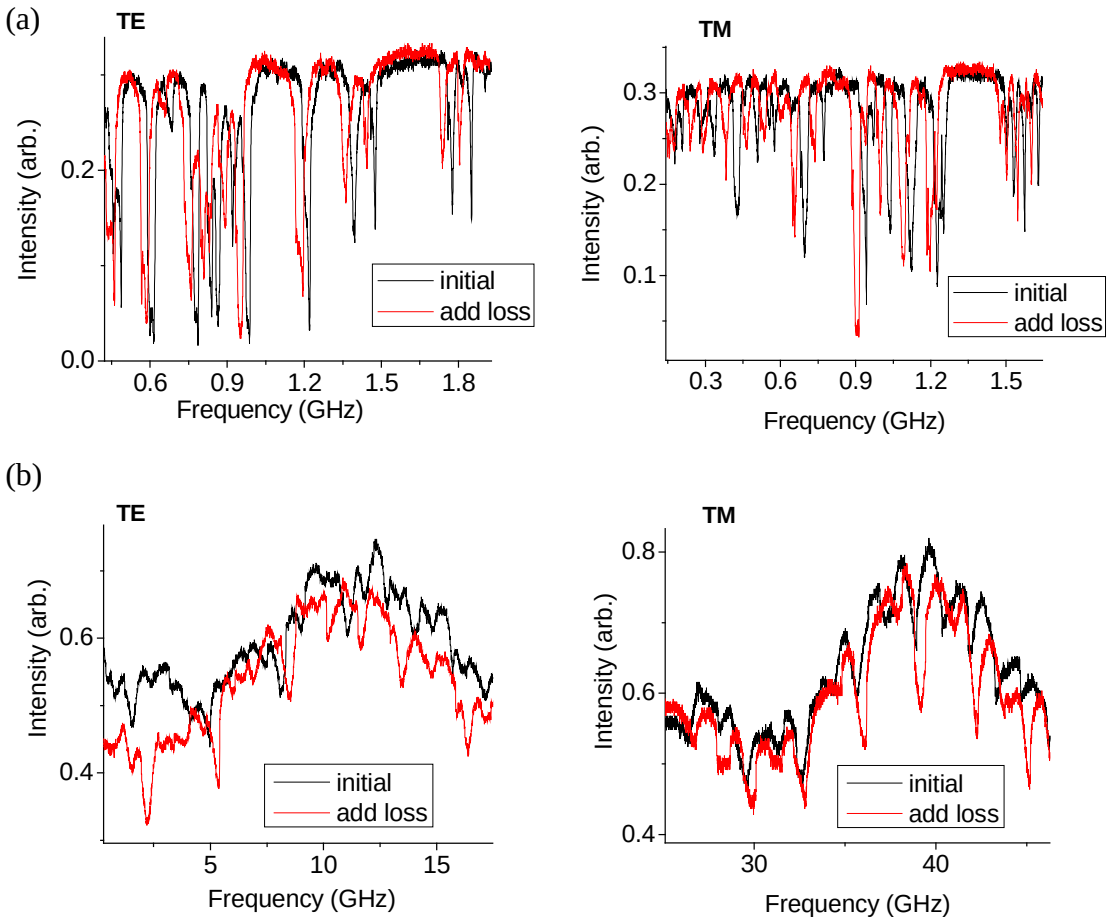

Figure VI.15. TE and TM whispering gallery modes of (a) a microsphere coated with a PDDA monolayer, and (b) after growing Au nanorods and nanospheres on its surface.

WG modes excited with longer (1550 nm) wavelength showed undercoupled behavior. Figure VI.16 shows the WGM spectra of a microsphere resonator, with Au nanoparticles grown on its surface, at two different excitation wavelengths 800 nm (Fig. VI.16(a)) and 1550 nm (Fig. VI.16(a)).

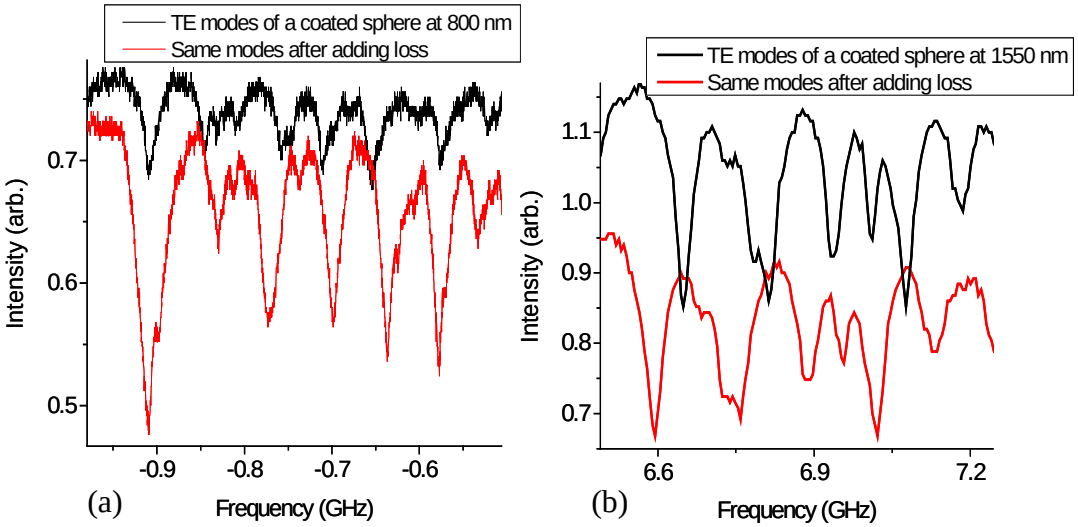

Figure VI.16. WGMs of a sphere with Au nanorods and nanospheres grown on its surface excited with two different wavelengths (a) 800 nm and (b) 1550 nm.

The wavelength dependence of the coupling enhancement suggests that it is caused by the surface plasmon related enhancement of the local fields. The WGM can excite the nanorods' SPs as well increase the interaction between individual nanoparticles.

VI.4.3 Calculation of the coupling enhancement

To quantify the enhancement, we have used a simple four-mirror model of a ring

resonator described in Chapter III, which gives us relations between the measured WGM dip depth (M_0) and the ratio of coupling to intrinsic losses (x) and between the dip width and the total round trip loss $(T+\alpha l)$, where T is proportional to the coupling losses and αl is proportional to the round trip intrinsic losses. From the dip depth (III.7) and knowledge of whether it is overcoupled or undercoupled, the loss ratio (III.3) can be found.

The loaded Q_{total} is inversely proportional to the total loss $(T+\alpha l)$, and thus to the dip width. Q_{in} is likewise related to the intrinsic loss αl, and $Q_{coupling}$ to the coupling loss T, so $Q_{coupling}$ and Q_{in} can be found from Q_{total} and x:

$$Q_{total} = \frac{Q_{in}Q_{coupling}}{Q_{in}+Q_{coupling}} = Q_{coupling}\left(\frac{1}{1+\frac{1}{x}}\right), \tag{VI.1}$$

consequently

$$\begin{aligned} Q_{coupling} &= Q_{total}\left(1+\frac{1}{x}\right) \\ Q_{in} &= Q_{total}\left(x+1\right). \end{aligned} \tag{VI.2}$$

After coating the microsphere resonator with a polyelectrolyte layer (PDDA), most WGMs are undercoupled. M_0 (from dip depth) and Q_{total} (from dip width) are measured for a strongly undercoupled mode, because only these are likely to survive after coating the resonator with Au NRs. Since the mode is undercoupled, only the root with $x<1$ is considered in (III.7).

After growing Au NRs on the surface of the resonator, the same measurements are made. Now, however, because the WGMs are strongly overcoupled, only $x>1$ is

relevant. Comparing coupling losses before (T^I) and after (T^{II}) adding Au NRs gives the coupling enhancement *C* resulting from the field enhancement due to the Au NR surface plasmon resonance:

$$C = \frac{T^{II}}{T^I} = \frac{Q_c^I}{Q_c^{II}} = \frac{Q_t^I\left(1+\frac{1}{x^I}\right)}{Q_t^{II}\left(1+\frac{1}{x^{II}}\right)}. \qquad \text{(VI.3)}$$

A similar ratio between the intrinsic losses before and after can give the increase in the intrinsic losses:

$$\frac{(\alpha l)^{II}}{(\alpha l)^I} = \frac{Q_{in}^I}{Q_{in}^{II}} = \frac{Q_{total}^I\left(x^I+1\right)}{Q_{total}^{II}\left(x^{II}+1\right)}. \qquad \text{(VI.4)}$$

Coupling enhancement factors *C* between 200 and 500 with an increase of only about 50% in the intrinsic loss have been measured for the WGMs of a 500-μm-diameter sphere shown in Fig. VI.15. This order of magnitude is typical for Au NR-coated spheres. No significant difference in the enhancement of TE and TM modes was found.

VI.5 Conclusions

In conclusion, the synthesis of Au NRs using HgTe NPs as nucleation seeds is demonstrated. The method provides a simple way to permanently attach gold nanorods on surfaces with different electrical and optical properties. Further work can be done to determine the nanometer-scale composition distribution, and optical properties of metal NR – semiconductor NP composites. It was shown that synthesis of Au NRs on a high quality factor microresonator leads to an increase in evanescent coupling between a coated microresonator and an optical fiber. Strong overcoupling suggests enhancement of

the evanescent field of the WGMs, caused by the surface plasmon resonance of the Au NRs. Comparison of the coupling loss before and after Au NR growth indicates coupling enhancement by a factor of 10^2 to 10^3. Gold nanoparticle coated resonators are expected to enhance the sensitivity of WGM evanescent-wave chemical sensors. These resonators are also good candidates for surface-enhanced Raman scattering experiments. Future work on device fabrication is feasible.

.

REFERENCES

1. L. Rayleigh, "The incidence of light upon a transparent sphere of dimensions comparable with the wave-length," Proc. R. Soc. Lond. A **84**, 25-46 (1910).

2. L. Rayleigh, "The Problem of the Whispering Gallery," Phil. Mag. **20**, 1001-1004 (1910).

3. P. Debye, "The heliograph of spheres of any material," Ann. Physik **30**, 57-136 (1909).

4. G. Mie, "Articles on the optical characteristics of turbid tubes, especially colloidal metal solutions," Ann. Physik **25**, 377-445 (1908).

5. C. G. Garrett, W. Kaiser, and W. L. Bond, "Stimulated Emission into Optical Whispering Modes of Spheres," Phys. Rev. **1**, 1807-1809 (1961).

6. P. Walsh and G. Kemeny, "Laser Operation without Spikes in a Ruby Ring," J. Appl. Phys. **34**, 956-959 (1963).

7. R. E. Benner, P. W. Barber, J. F. Owen, and R. K. Chang, "Observation of Structure Resonances in the Fluorescence-Spectra from Microspheres," Phys. Rev. Lett. **44**, 475-478 (1980).

8. S. C. Hill, R. E. Benner, C. K. Rushforth, and P. R. Conwell, "Structural Resonances Observed in the Fluorescence Emission from Small Spheres on Substrates," Appl. Opt. **23**, 1680-1683 (1984).

9. J. B. Snow, S. X. Qian, and R. K. Chang, "Stimulated Raman-Scattering from Individual Water and Ethanol Droplets at Morphology-Dependent Resonances," Opt. Lett. **10**, 37-39 (1985).

10. S. X. Qian, J. B. Snow, and R. K. Chang, "Coherent Raman Mixing and Coherent Anti-Stokes Raman-Scattering from Individual Micrometer-Size Droplets," Opt.

Lett. **10**, 499-501 (1985).

11. H. M. Tzeng, K. F. Wall, M. B. Long, and R. K. Chang, "Laser-Emission from Individual Droplets at Wavelengths Corresponding to Morphology-Dependent Resonances," Opt. Lett. **9**, 499-501 (1984).

12. H. B. Lin, A. L. Huston, B. L. Justus, and A. J. Campillo, "Some Characteristics of a Droplet Whispering-Gallery-Mode Laser," Opt. Lett. **11**, 614-616 (1986).

13. V. B. Braginsky, M. L. Gorodetsky, and V. S. Ilchenko, "Quality-Factor and Nonlinear Properties of Optical Whispering-Gallery Modes," Phys. Lett. A **137**, 393-397 (1989).

14. H. Frohlich, "The specific temperatures of the electrons of small metal particles at low temperatures," Physica **4**, 0406-0412 (1937).

15. S. V. Gaponenko, *Optical properties of semiconductor nanocrystals*, Cambridge Studies in Modern Optics (Cambridge University Press, Cambridge, 1998).

16. Y. Masumoto and T. Takagahara, *Semiconductor Quantum Dots*, NanoScience and Technology (Springer, Heidelberg 2002).

17. U. Kreibig and M. Vollmer, *Optical Properties of Metal Clusters*, Springer Series in Materials Science (Springer, Heidelberg, 1995), Vol. 25.

18. Y. Arakawa and H. Sakaki, "Multidimensional Quantum Well Laser and Temperature-Dependence of Its Threshold Current," Appl. Phys. Lett. **40**, 939-941 (1982).

19. M. Asada, Y. Miyamoto, and Y. Suematsu, "Gain and the Threshold of 3-Dimensional Quantum-Box Lasers," IEEE J. Quantum Electron. **22**, 1915-1921 (1986).

20. J. Oshinowo, M. Nishioka, S. Ishida, and Y. Arakawa, "Highly Uniform InGaAs/GaAs Quantum Dots (Similar-to-15 nm) by Metalorganic Chemical-Vapor-Deposition," Appl. Phys. Lett. **65**, 1421-1423 (1994).

21. D. Bimberg, N. Kirstaedter, N. N. Ledentsov, Z. I. Alferov, P. S. Kopev, and V.

M. Ustinov, "InGaAs-GaAs quantum-dot lasers," IEEE J. Sel. Top. Quantum Electron. **3**, 196-205 (1997).

22. J. A. Lott, N. N. Ledentsov, V. M. Ustinov, N. A. Maleev, A. E. Zhukov, A. R. Kovsh, M. V. Maximov, B. V. Volovik, Z. I. Alferov, and D. Bimberg, "InAs-InGaAs quantum dot VCSELs on GaAs substrates emitting at 1.3 μm," Electron. Lett. **36**, 1384-1385 (2000).

23. R. L. Sellin, C. Ribbat, D. Bimberg, F. Rinner, H. Konstanzer, M. T. Kelemen, and M. Mikulla, "High-reliability MOCVD-grown quantum dot laser," Electron. Lett. **38**, 883-884 (2002).

24. S. S. Kher and R. L. Wells, "Synthesis and characterization of colloidal nanocrystals of capped gallium arsenide," Nanostruct. Mater. **7**, 591-603 (1996).

25. C. B. Murray, D. J. Norris, and M. G. Bawendi, "Synthesis and Characterization of Nearly Monodisperse CdE (E = S, Se, Te) Semiconductor Nanocrystallites," J. Am. Chem. Soc. **115**, 8706-8715 (1993).

26. C. B. Murray, S. H. Sun, W. Gaschler, H. Doyle, T. A. Betley, and C. R. Kagan, "Colloidal synthesis of nanocrystals and nanocrystal superlattices," IBM J. Res. Dev. **45**, 47-56 (2001).

27. A. L. Rogach, M. T. Harrison, S. V. Kershaw, A. Kornowski, M. G. Burt, A. Eychmüller, and H. Weller, "Colloidally prepared CdHgTe and HgTe quantum dots with strong near-infrared luminescence," Phys. Status Solidi B **224**, 153-158 (2001).

28. A. Sashchiuk, L. Langof, R. Chaim, and E. Lifshitz, "Synthesis and characterization of PbSe and PbSe/PbS core-shell colloidal nanocrystals," J. Cryst. Growth **240**, 431-438 (2002).

29. E. H. Sargent, "Infrared quantum dots," Adv. Mater. **17**, 515-522 (2005).

30. V. S. Dneprovskii, V. I. Klimov, D. K. Okorokov, and Y. V. Vandyshev, "Strong Optical Nonlinearities and Laser-Emission of Semiconductor Microcrystals," Solid State Commun **81**, 227-230 (1992).

31. A. V. Malko, A. A. Mikhailovsky, M. A. Petruska, J. A. Hollingsworth, H. Htoon,

M. G. Bawendi, and V. I. Klimov, "From amplified spontaneous emission to microring lasing using nanocrystal quantum dot solids," Appl. Phys. Lett. **81**, 1303-1305 (2002).

32. R. D. Schaller, M. A. Petruska, and V. I. Klimov, "Tunable near-infrared optical gain and amplified spontaneous emission using PbSe nanocrystals," J. Phys. Chem. B **107**, 13765-13768 (2003).

33. L. Fradkin, L. Langof, E. Lifshitz, A. Rogach, N. Gaponik, H. Weller, and A. Eychmüller, "Magneto-optical studies of HgTe/$Hg_xCd_{1-x}Te$(S) core-shell nanocrystals," ChemPhysChem **4**, 1203-1210 (2003).

34. G. Chen, R. Rapaport, D. T. Fuchs, L. Lucas, A. J. Lovinger, S. Vilan, A. Aharoni, and U. Banin, "Optical gain from InAs nanocrystal quantum dots in a polymer matrix," Appl. Phys. Lett. **87**, 251108 (2005).

35. X. D. Fan, P. Palinginis, S. Lacey, H. L. Wang, and M. C. Lonergan, "Coupling semiconductor nanocrystals to a fused-silica microsphere: a quantum-dot microcavity with extremely high Q factors," Opt. Lett. **25**, 1600-1602 (2000).

36. P. Olk, B. C. Buchler, V. Sandoghdar, N. Gaponik, A. Eychmüller, and A. L. Rogach, "Subwavelength emitters in the near-infrared based on mercury telluride nanocrystals," Appl. Phys. Lett. **84**, 4732-4734 (2004).

37. S. L. Lu, D. S. Jiang, R. Jia, L. An, L. F. Bian, X. G. Liang, B. S. Ma, and B. Q. Sun, "Lasing of $CdSe_xS_{1-x}$ quantum dots in a glass spherical microcavity," J. Phys.-Condens Mat. **14**, 6395-6401 (2002).

38. M. Artemyev, U. Woggon, and W. Langbein, "Quantum dot emission confined by a spherical photonic dot," Phys. Status Solidi B **229**, 423-426 (2002).

39. Y. P. Rakovich, L. Yang, E. M. McCabe, J. F. Donegan, T. Perova, A. Moore, N. Gaponik, and A. Rogach, "Whispering gallery mode emission from a composite system of CdTe nanocrystals and a spherical microcavity," Semicond. Sci. Technol. **18**, 914-918 (2003).

40. S. I. Shopova, G. Farca, A. T. Rosenberger, W. M. S. Wickramanayake, and N. A. Kotov, "Microsphere whispering-gallery-mode laser using HgTe quantum dots," Appl. Phys. Lett. **85**, 6101-6103 (2004).

41. S. I. Shopova, C. W. Blackledge, A. T. Rosenberger, and N. F. Materer, "Gold nanorods grown from HgTe nanoparticles directly on various surfaces," Appl. Phys. Lett. **89**, 023120 (2006).

42. J. A. Stratton, *Electromagnetic Theory* (McGraw-Hill Book Company, Inc., New York and London, 1941).

43. S. Schiller, "Asymptotic-Expansion of Morphological Resonance Frequencies in Mie Scattering," Appl. Opt. **32**, 2181-2185 (1993).

44. H. M. Lai, P. T. Leung, K. Young, P. W. Barber, and S. C. Hill, "Time-Independent Perturbation for Leaking Electromagnetic Modes in Open Systems with Application to Resonances in Microdroplets," Phys. Rev. A **41**, 5187-5198 (1990).

45. D. W. Vernooy and H. J. Kimble, "Quantum structure and dynamics for atom galleries," Phys. Rev. A **55**, 1239-1261 (1997).

46. A. N. Oraevsky, "Whispering-gallery waves," Quantum Electron. **32**, 377-400 (2002).

47. H. A. Haus, *Waves and fields in optoelectronics*, Prentice-Hall series in solid state physical electronics (Prentice-Hall Inc., Engelwood Cliffs, 1984), Ch.7.

48. D. W. Vernooy, V. S. Ilchenko, H. Mabuchi, E. W. Streed, and H. J. Kimble, "High-Q measurements of fused-silica microspheres in the near infrared," Opt. Lett. **23**, 247-249 (1998).

49. G. C. Papavassiliou, "Optical properties of small inorganic and organic metal particles," Prog. Solid St. Chem. **12**, 185-271 (1979).

50. C. Bohren and D. Huffman, *Absorption and scattering of small particles.* (John Wiley & Sons, Inc., New York, 1983), pp. 102-104.

51. C. Bohren and D. Huffman, *Absorption and scattering of small particles* (John Wiley & Sons Inc., New York, 1983), p. 80.

52. R. Gans, "The shape of ultra microscopic gold particles," Ann. Physik **37**, 881-

900 (1912).

53. P. B. Johnson and R. W. Christy, "Optical-Constants of Noble-Metals," Phys. Rev. B **6**, 4370-4379 (1972).

54. Y. Niidome, H. Takahashi, S. Urakawa, K. Nishioka, and S. Yamada, "Immobilization of gold nanorods on the glass substrate by the electrostatic interactions for localized plasmon sensing," Chem. Lett. **33**, 454-455 (2004).

55. S. Link and M. A. El-Sayed, "Spectral properties and relaxation dynamics of surface plasmon electronic oscillations in gold and silver nanodots and nanorods," J. Phys. Chem. B **103**, 8410-8426 (1999).

56. E. Kretschmann, "Determination of Optical Constants of Metals by Excitation of Surface Plasmons," Z. Phys. **241**, 313-317 (1971).

57. M. L. Gorodetsky and V. S. Ilchenko, "High-Q Optical Whispering-Gallery Microresonators - Precession Approach for Spherical Mode Analysis and Emission Patterns with Prism Couplers," Opt. Commun. **113**, 133-143 (1994).

58. B. E. Little, J. P. Laine, and H. A. Haus, "Analytic theory of coupling from tapered fibers and half-blocks into microsphere resonators," J. Lightw. Technol. **17**, 704-715 (1999).

59. J. D. Love, W. M. Henry, W. J. Stewart, R. J. Black, S. Lacroix, and F. Gonthier, "Tapered Single-Mode Fibers and Devices.I. Adiabaticity Criteria," IEE Proc. Optoelectron. **138**, 343-354 (1991).

60. J. D. Love and W. M. Henry, "Quantifying Loss Minimization in Single-Mode Fiber Tapers," Electron. Lett. **22**, 912-914 (1986).

61. A. Yariv, "Universal relations for coupling of optical power between microresonators and dielectric waveguides," Electron. Lett. **36**, 321-322 (2000).

62. D. R. Rowland and J. D. Love, "Evanescent-Wave Coupling of Whispering-Gallery Modes of a Dielectric Cylinder," IEE Proc. Optoelectron. **140**, 177-188 (1993).

63. M. J. Humphrey, "Calculations of coupling between tapered fiber modes and whispering-gallery modes of a spherical microlaser " Ph.D. dissertation (Oklahoma State University, Stillwater, 2004).

64. G. Farca, "Cavity-Enhanced Evanescent-Wave Chemical Sensing Using Microresonators," Ph.D. dissertation (Okalahoma State University, Stillwater, 2006).

65. H. Goronkin, P. Allmen, R. Tsui, and T. Zhu, "R&D Status and Trends in Nonoparticles, Nanostructured Materials, and Nanodevices," (International Technology Research Institute, World Technology Division, Loyola College in Maryland, 1999).

66. S. V. Gaponenko, *Optical properties of semiconductor nanocrystals*, Cambridge Studies in Modern Optics (Cambridge University Press, Cambridge, 1998), Ch. 2.

67. N. Peyghambarian, S. W. Koch, and A. Mysyrowicz, *Introduction to Semiconductor Optics*, Prentice Hall Series in Solid State Physical Electronics (Prentice Hall, Englewood Cliffs, NJ, 1993).

68. S. V. Gaponenko, *Optical properties of semiconductor nanocrystals*, Cambridge Studies in Modern Optics (Cambridge University Press, Cambridge, 1998), Ch. 1.

69. A. I. Ekimov, F. Hache, M. C. Schanneklein, D. Ricard, C. Flytzanis, I. A. Kudryavtsev, T. V. Yazeva, A. V. Rodina, and A. L. Efros, "Absorption and Intensity-Dependent Photoluminescence Measurements on CdSe Quantum Dots - Assignment of the 1st Electronic-Transitions," J. Opt. Soc. Am. B **10**, 100-107 (1993).

70. S. Adachi, *Optical Constants of Crystalline and Amorphous Semiconductors* (Kluwer Academic Publisher, Norwell, 1999), pp. 553-555.

71. Y. Masumoto and T. Takagahara, *Semiconductor Quantum Dots*, NanoScience and Technology (Springer, Heidelberg 2002), p. 62.

72. L. E. Brus, "Electron Electron and Electron-Hole Interactions in Small Semiconductor Crystallites - the Size Dependence of the Lowest Excited Electronic State," J. Chem. Phys. **80**, 4403-4409 (1984).

73. Y. Kayanuma, "Wannier Exciton in Microcrystals," Solid State Commun. **59**, 405-408 (1986).

74. H. M. Schmidt and H. Weller, "Photochemistry of Colloidal Semiconductors.IV. Quantum Size Effects in Semiconductor Crystallites - Calculation of the Energy-Spectrum for the Confined Exciton," Chem. Phys. Lett. **129**, 615-618 (1986).

75. S. V. Gaponenko, *Optical properties of semiconductor nanocrystals*, Cambridge Studies in Modern Optics (Cambridge University Press, Cambridge, 1998), p. 30.

76. T. Takagahara, "Electron-phonon interactions in semiconductor nanocrystals," J. Lumin. **70**, 129-143 (1996).

77. Y. Masumoto and T. Takagahara, *Semiconductor Quantum Dots*, NanoScience and Technology (Springer, Heidelberg 2002), pp. 66-67.

78. K. J. Vahala, "Quantum Box Fabrication Tolerance and Size Limits in Semiconductors and Their Effect on Optical Gain," IEEE J. Quantum Electron. **24**, 523-530 (1988).

79. K. Vahala and A. Yariv, "Application of an Electronic Wave-Packet Formalism to Local-Operator Equations of Motion for Semiconductor-Lasers," Phys. Rev. A **32**, 345-356 (1985).

80. K. An and H. J. Moon, "Laser oscillations with pumping-independent ultrahigh cavity quality factors in evanescent-wave-coupled-gain microsphere dye lasers," J. Phys. Soc. Jpn. **72**, 773-776 (2003).

81. M. Cai, O. Painter, K. J. Vahala, and P. C. Sercel, "Fiber-coupled microsphere laser," Opt. Lett. **25**, 1430-1432 (2000).

82. S. Hoogland, V. Sukhovatkin, I. Howard, S. Cauchi, L. Levina, and E. H. Sargent, "A solution-processed 1.53 mu m quantum dot laser with temperature-invariant emission wavelength," Opt. Express **14**, 3273-3281 (2006).

83. F. Lissillour, D. Messager, G. Stéphan, and P. Féron, "Whispering-gallery-mode laser at 1.56 mu m excited by a fiber taper," Opt. Lett. **26**, 1051-1053 (2001).

84. V. Sandoghdar, F. Treussart, J. Hare, V. Lefèvre-Seguin, J. M. Raimond, and S. Haroche, "Very low threshold whispering-gallery-mode microsphere laser," Phys. Rev. A **54**, R1777-R1780 (1996).

85. L. Yang and K. J. Vahala, "Gain functionalization of silica microresonators," Opt. Lett. **28**, 592-594 (2003).

86. I. Protsenko, P. Domokos, V. Lefèvre-Seguin, J. Hare, J. M. Raimond, and L. Davidovich, "Quantum theory of a thresholdless laser," Phys. Rev. A **59**, 1667-1682 (1999).

87. M. V. Artemyev, U. Woggon, R. Wannemacher, H. Jaschinski, and W. Langbein, "Light trapped in a photonic dot: Microspheres act as a cavity for quantum dot emission," Nano Lett. **1**, 309-314 (2001).

88. S. Haroche and D. Kleppner, "Cavity Quantum Electrodynamics," Phys. Today **42**, 24-30 (1989).

89. R. Chang and A. Campillo, *Optical Processes in Microcavities*, Advanced Series in Applied Physics (World Scientific Publishing Co. Pte. Ltd., Singapore, 1996), Vol. 3, pp. 1-75.

90. A. Thränhardt, C. Ell, G. Khitrova, and H. M. Gibbs, "Relation between dipole moment and radiative lifetime in interface fluctuation quantum dots," Phys. Rev. B **65**, 035327 (2002).

91. U. Woggon, R. Wannemacher, M. V. Artemyev, B. Möller, N. LeThomas, V. Anikeyev, and O. Schöps, "Dot-in-a-dot: electronic and photonic confinement in all three dimensions," Appl. Phys. B **77**, 469-484 (2003).

92. K. H. Drexhage, "Influence of a dielectric interface on fluorescence decay time," J. Lumin. **1-2**, 693-701 (1970).

93. R. E. Kunz and W. Lukosz, "Changes in Fluorescence Lifetimes Induced by Variable Optical Environments," Phys. Rev. B **21**, 4814-4828 (1980).

94. W. Lukosz, "Light-Emission by Magnetic and Electric Dipoles Close to a Plane Dielectric Interface III. Radiation-Patterns of Dipoles with Arbitrary Orientation," J. Opt. Soc. Am. **69**, 1495-1503 (1979).

95. W. Lukosz and R. E. Kunz, "Light-Emission by Magnetic and Electric Dipoles Close to a Plane Interface I. Total Radiated Power," J. Opt. Soc. Am. **67**, 1607-1615 (1977).

96. W. Lukosz and R. E. Kunz, "Light-Emission by Magnetic and Electric Dipoles Close to a Plane Dielectric Interface II. Radiation-Patterns of Perpendicular Oriented Dipoles," J. Opt. Soc. Am. **67**, 1615-1619 (1977).

97. G. S. Agarwal, "Coherence in Spontaneous Emission in Presence of a Dielectric," Phys. Rev. Lett. **32**, 703-706 (1974).

98. G. S. Agarwal, "Quantum Electrodynamics in Presence of Dielectrics and Conductors IV. General Theory for Spontaneous Emission in Finite Geometries," Phys. Rev. A **12**, 1475-1497 (1975).

99. G. S. Agarwal, "Quantum Electrodynamics in Presence of Dielectrics and Conductors III. Relations among One-Photon Transition-Probabilities in Stationary and Nonstationary Fields, Density of States, Field-Correlation Functions, and Surface-Dependent Response Functions," Phys. Rev. A **11**, 253-264 (1975).

100. M. Pelton and Y. Yamamoto, "Ultralow threshold laser using a single quantum dot and a microsphere cavity," Phys. Rev. A **59**, 2418-2421 (1999).

101. B. K. Min, T. J. Kippenberg, L. Yang, K. J. Vahala, J. Kalkman, and A. Polman, "Erbium-implanted high-Q silica toroidal microcavity laser on a silicon chip," Phys. Rev. A **70**, 033803 (2004).

102. P. W. Milonni and J. H. Eberly, *Lasers* (John Wiley & Sons, New York, 1988).

103. A. Rogach, D. Koktysh, M. Harrison, and N. Kotov, "Layer-by-layer assembled films of HgTe nanocrystals with strong infrared emission," Chem. Mater. **12**, 1526-1528 (2000).

104. Z. Y. Tang, Y. Wang, and N. A. Kotov, "Semiconductor nanoparticles on solid substrates: Film structure, intermolecular interactions, and polyelectrolyte effects," Langmuir **18**, 7035-7040 (2002).

105. J. C. Knight, G. Cheung, F. Jacques, and T. A. Birks, "Phase-matched excitation

of whispering-gallery-mode resonances by a fiber taper," Opt. Lett. **22**, 1129-1131 (1997).

106. A. L. Efros and A. V. Rodina, "Band-Edge Absorption and Luminescence of Nonspherical Nanometer-Size Crystals," Phys. Rev. B **47**, 10005-10007 (1993).

107. A. Naweed, G. Farca, S. I. Shopova, and A. T. Rosenberger, "Induced transparency and absorption in coupled whispering-gallery microresonators," Phys. Rev. A **71**, 043804 (2005).

108. I. S. Grudinin, A. B. Matsko, A. A. Savchenkov, D. Strekalov, V. S. Ilchenko, and L. Maleki, "Ultra high Q crystalline microcavities," Opt. Commun. **265**, 33-38 (2006).

109. Y. Yu, S. Chang, C. Lee, and C. Wang, "Gold nanorods: Electrochemical synthesis and optical properties," J. Phys. Chem. B **101**, 6661-6664 (1997).

110. A. Gole and C. Murphy, "Seed-mediated synthesis of gold nanorods: Role of the size and nature of the seed," Chem. Mater. **16**, 3633-3640 (2004).

111. S. Link and M. El-Sayed, "Optical properties and ultrafast dynamics of metallic nanocrystals," Ann. Rev. Phys. Chem. **54**, 331-366 (2003).

112. C. Sonnichsen and A. Alivisatos, "Gold nanorods as novel nonbleaching plasmon-based orientation sensors for polarized single-particle microscopy," Nano Lett. **5**, 301-304 (2005).

113. C. J. Murphy, T. K. San, A. M. Gole, C. J. Orendorff, J. X. Gao, L. Gou, S. E. Hunyadi, and T. Li, "Anisotropic metal nanoparticles: Synthesis, assembly, and optical applications," J. Phys. Chem. B **109**, 13857-13870 (2005).

114. J. Perez-Juste, L. Liz-Marzan, S. Carnie, D. Chan, and P. Mulvaney, "Electric-field-directed growth of gold nanorods in aqueous surfactant solutions," Adv. Funct. Mater. **14**, 571-579 (2004).

115. H. Liao and J. Hafner, "Monitoring gold nanorod synthesis on surfaces," J. Phys. Chem. B **108**, 19276-19280 (2004).

116. A. J. Mieszawska and F. P. Zamborini, "Gold nanorods grown directly on surfaces from microscale patterns of gold seeds," Chem. Mater. **17**, 3415-3420 (2005).

117. N. Taub, O. Krichevski, and G. Markovich, "Growth of gold nanorods on surfaces," J. Phys. Chem. B **107**, 11579-11582 (2003).

118. Z. Wei, A. Mieszawska, and F. Zamborini, "Synthesis and manipulation of high aspect ratio gold nanorods grown directly on surfaces," Langmuir **20**, 4322-4326 (2004).

119. D. Koktysh, N. Gaponik, M. Reufer, J. Crewett, U. Scherf, A. Eychmuller, J. Lupton, A. Rogach, and J. Feldmann, "Near-infrared electroluminescence from HgTe nanocrystals," ChemPhysChem **5**, 1435-1438 (2004).

120. C. Sonnichsen, T. Franzl, T. Wilk, G. von Plessen, J. Feldmann, O. Wilson, and P. Mulvaney, "Drastic reduction of plasmon damping in gold nanorods," Phys. Rev. Lett. **88**, 077402 (2002).

121. H. R. Stuart and D. G. Hall, "Enhanced dipole-dipole interaction between elementary radiators near a surface," Phys. Rev. Lett. **80**, 5663-5666 (1998).

122. T. Sau and C. Murphy, "Seeded high yield synthesis of short Au nanorods in aqueous solution," Langmuir **20**, 6414-6420 (2004).

123. C. J. Johnson, E. Dujardin, S. A. Davis, C. J. Murphy, and S. Mann, "Growth and form of gold nanorods prepared by seed-mediated, surfactant-directed synthesis," J. Mater. Chem. **12**, 1765-1770 (2002).

124. B. Nikoobakht and M. El-Sayed, "Preparation and growth mechanism of gold nanorods (NRs) using seed-mediated growth method," Chem. Mater. **15**, 1957-1962 (2003).

125. E. Kretschmann and H. Raether, "Radiative Decay of Non Radiative Surface Plasmons Excited by Light," Z. Naturforsch., A: Phys. Sci. **A 23**, 2135-2136 (1968).

126. W. H. Weber and S. L. McCarthy, "Anomalies in Surface Plasmon Resonance Excitation at Both Surfaces of Evaporated Metal-Films," Appl. Phys. Lett. **25**,

396-398 (1974).

127. I. Pockrand, "Resonance Anomalies in Light-Intensity Reflected at Silver Gratings with Dielectric Coatings," J. Phys. D **9**, 2423-2432 (1976).

128. R. H. Ritchie, E. T. Arakawa, J. J. Cowan, and R. N. Hamm, "Surface-Plasmon Resonance Effect in Grating Diffraction," Phys. Rev. Lett. **21**, 1530-1534 (1968).

129. G. Schider, J. R. Krenn, W. Gotschy, B. Lamprecht, H. Ditlbacher, A. Leitner, and F. R. Aussenegg, "Optical properties of Ag and Au nanowire gratings," J. Appl. Phys. **90**, 3825-3830 (2001).

130. E. Kretschmann, "Determination of Surface-Roughness of Thin-Films Using Measurement of Angular-Dependence of Scattered Light from Surface Plasma-Waves," Opt. Commun. **10**, 353-356 (1974).

131. R. D. Harris and J. S. Wilkinson, "Wave-Guide Surface-Plasmon Resonance Sensors," Sens. Actuators B **29**, 261-267 (1995).

132. W. Lukosz, "Principles and Sensitivities of Integrated Optical and Surface-Plasmon Sensors for Direct Affinity Sensing and Immunosensing," Biosens. Bioelectron. **6**, 215-225 (1991).

133. P. Stöcker, B. Menges, U. Langbein, and S. Mittler, "Multimode waveguide mode surface plasmon coupling: a sensitivity and device realizability study," Sens. Actuators A **116**, 224-231 (2004).

134. B. Gupta and A. Sharma, "Sensitivity evaluation of a multi-layered surface plasmon resonance-based fiber optic sensor: a theoretical study," Sens. Actuators B **107**, 40-46 (2004).

135. A. Sharma and B. Gupta, "Fiber optic sensor based on surface plasmon resonance with nanoparticle films," Photonics and Nanostructures - Fundamentals and Applications **3**, 30-37 (2005).

136. J. N. Yih, F. C. Chien, C. Y. Lin, H. F. Yau, and S. J. Chen, "Angular-interrogation attenuated total reflection metrology system for plasmonic sensors," Appl. Opt. **44**, 6155-6162 (2005).

VITA

Siyka Ivanova Shopova

Candidate for the Degree of

Doctor of Philosophy

Thesis: NANOPARTICLE-COATED OPTICAL MICRORESONATORS FOR WHISPERING-GALLERY LASING AND OTHER APPLICATIONS

Major Field: Photonics

Biographical:

Personal Data: Born on April 19, 1965 in Bulgaria.

Education: Received Masters of Science degree in Engineering Physics from Sofia University Kliment Ohridski, Sofia, Bulgaria in 1989; Completed the requirements for the Doctor in Philosophy degree in Photonics at Oklahoma State University in January, 2007

Experience: Research Assistant - 2001-until now, Teaching Assistant - 2000-2001, Physics Department at Oklahoma State University, Stillwater, OK; High School Physics Teacher - 1997-2000, Mathematics and Physics High School, Bulgaria; Researcher - 1996-1997, Institute of Physical Chemistry at Bulgarian Academy of Science; Laser Physicist - 1993-1996, Optron Technology Ltd., Sofia, Bulgaria

Professional Memberships: OSA

Name: Siyka Shopova Date of Degree: May, 2007

Institution: Oklahoma State University Location: Stillwater, Oklahoma

Title of Study: NANOPARTICLE-COATED OPTICAL MICRORESONATORS FOR WHISPERING-GALLERY LASING AND OTHER APPLICATIONS

Pages in Study:148 Candidate for the Degree of Doctor of Philosophy

Major Field: Photonics

Scope and Method of Study:

The purpose of this study is to explore the properties of high quality optical microsphere resonators in combination with various types of nanoparticles deposited on their surfaces. Optical whispering-gallery modes of the silica microspheres were pumped efficiently by tapered optical fibers. For whispering-gallery lasing, the microspheres were coated with HgTe and HgCdTe quantum dots. Gold nanorods were grown on the surface of the microspheres nucleated by HgTe nanopartiles.

Findings and Conclusions:

Lasing in HgTe was demonstrated for the first time and record low thresholds were measured in these devices. Interesting effect on enhancement of evanescent coupling was observed with microsphere resonators with gold nanorods grown on their surfaces. We develop a new procedure that uses semiconductor nanoparticles as seeds for growth of gold nanorods.

ADVISER'S APPROVAL: Albert T. Rosenberger